Rapid magnetic resonance tissue relaxometry in the steady state

Inauguraldissertation
zur
Erlangung der Würde eines Doktors der Philosophie
vorgelegt der
Philosophisch-Naturwissenschaftlichen Fakultät
der Universität Basel

von
Rahel Maria Heule
aus Widnau SG

Basel, 2015

Genehmigt von der Philosophisch-Naturwissenschaftlichen Fakultät
auf Antrag von

Prof. Dr. Thomas Vetter
Fakultätsverantwortlicher
Prof. Dr. Oliver Bieri
Dissertationsleiter
Prof. Dr. Stefan Ropele
Korreferent

Basel, den 23. Juni 2015

Prof. Dr. Jörg Schibler
Dekan

Abstract

Longitudinal (T_1) and transverse (T_2) relaxation are the most fundamental physical processes governing the signal intensity and the soft tissue contrast in magnetic resonance imaging (MRI). The T_1 and T_2 relaxation times are characteristic properties of living tissues and they were observed to be altered in the context of several diseases. Commonly, the MR images acquired in the clinical routine for medical assessment provide qualitative rather than quantitative information about the T_1 and T_2 relaxation times of the tissues of interest. The signal intensity generated by conventional qualitative MR imaging may be predominantly T_1- or T_2-weighted but is generally dependent on other tissue-specific parameters such as the proton density, the acquisition protocol, and the used MR hardware.

It is beneficial to directly measure the T_1 and T_2 relaxation times by acquiring typically two or more MR images of the same anatomical region but of different contrasts and to represent the results in quantitative maps. While these maps have the same structural appearance as the acquired base images, the individual pixel values have a physical meaning (i.e. the values of T_1 and T_2 in milliseconds) instead of displaying the signal intensity in arbitrary units. Quantitative maps of tissue-specific MR parameters are superior to conventional MR images since they are ideally independent of the MR protocol and hardware, and thus offer the possibility to directly compare the results from studies across multiple subjects, time-points, and imaging sites. Relaxation time measurements (also referred to as relaxometry) have demonstrated increased specificity and sensitivity to detect pathological tissue changes compared to conventional T_1- and T_2-weighted MR imaging.

In practice, T_1 and T_2 quantification techniques which are based on the acquisition of purely T_1- and T_2-weighted images without residual sensitivity on T_2 and T_1, respectively, require prohibitively long scan times making them not suited for the clinical practice. As a consequence, fast MR imaging using steady-state free precession (SSFP) sequences has come into the research focus of quantitative MRI. The images obtained from SSFP acquisitions show generally a mixed T_1 and T_2 contrast. Contemporary SSFP-based techniques for relaxation time measurements are impaired by a T_2-related bias in the T_1 quantification and by a T_1-related bias in the T_2 quantification. In addition, their speed comes at the expense of increased sensitivity to extrinsic instrumental factors (e.g. static or transmit field inhomogeneities).

In this thesis, new robust SSFP-based relaxometry methods are developed which offer clinically acceptable scan times and considerably reduce or even eliminate the T_2- and T_1-bias in the T_1 and T_2 calculation, respectively, of targets such as the human brain and the musculoskeletal system.

Publications arising from this thesis

Journal papers

- **Heule R**, Ganter C, Bieri O. Triple echo steady-state (TESS) relaxometry. Magn Reson Med, 71(1):230-237, 2014.
- **Heule R**, Ganter C, Bieri O. Rapid estimation of cartilage T_2 with reduced T_1 sensitivity using double echo steady state imaging. Magn Reson Med, 71(3):1137-1143, 2014.
- **Heule R**, Bär P, Mirkes C, Scheffler K, Trattnig S, Bieri O. Triple-echo steady-state T_2 relaxometry of the human brain at high to ultra-high fields. NMR Biomed, 27(9):1037-1045, 2014.
- **Heule R**, Ganter C, Bieri O. Variable flip angle T_1 mapping in the human brain with reduced T_2 sensitivity using fast radiofrequency-spoiled gradient echo imaging. Magn Reson Med, doi: 10.1002/mrm.25668, 2015.
- Juras V, Bohndorf K, **Heule R**, Kronnerwetter C, Szomolanyi P, Hager B, Bieri O, Zbyn S, Trattnig S. A comparison of multi-echo spin-echo and triple-echo steady-state T_2 mapping for in vivo evaluation of articular cartilage. Eur Radiol, submitted, 2015.

Patent application publication

- **Heule R**, Bieri O. Magnetic resonance imaging method for the quantification of the T_1 and/or T_2 relaxation times in a sample. US patent application 2014/0292,325, filed March 28, 2013, and issued October 2, 2014.

Conference proceedings

- **Heule R**, Bieri O. T_1-corrected rapid T_2 estimation using double echo steady state (DESS). Proceedings of the 29th Annual Meeting ESMRMB, Lisbon, 2012. E-poster.
- **Heule R**, Ganter C, Bieri O. Triple echo steady state (TESS) relaxometry. Proceedings of the 21st Annual Meeting ISMRM, Salt Lake City, 2013. Talk (ISMRM Merit Award - Magna cum Laude).
- **Heule R**, Bär P, Mirkes C, Scheffler K, Trattnig S, Bieri O. Fast B_1-insensitive T_2 relaxometry of the human brain at high to ultra-high fields. Proceedings of the Joint Annual Meeting ISMRM-ESMRMB, Milan, 2014. Talk (ISMRM Merit Award - Summa cum Laude).
- **Heule R**, Ganter C, Bieri O. Variable flip angle T_1 mapping in the human brain with reduced T_2 sensitivity using fast RF-spoiled gradient echo imaging. Proceedings of the 23rd Annual Meeting ISMRM, Toronto, 2015. E-poster.
- Pusterla O, Santini F, **Heule R**, Bieri O. T_2-snapshots imaging with simultaneous multislice TESS acquisition. Proceedings of the 23rd Annual Meeting ISMRM, Toronto, 2015.
- Juras V, Bohndorf K, **Heule R**, Kronnerwetter C, Szomolanyi P, Hager B, Bieri O, Trattnig S. Assessment of the clinical relevance of triple-echo steady-state T_2 mapping in articular cartilage. Proceedings of the 23rd Annual Meeting ISMRM, Toronto, 2015.
- Riegler G, Drlicek G, Kronnerwetter C, **Heule R**, Bieri O, Hager B, Bär P, Trattnig S. Triple-echo steady state T_2 mapping and high resolution axonal bundle assessment of the median nerve in healthy volunteers and patients with carpal tunnel syndrome at 7 Tesla. Proceedings of the 23rd Annual Meeting ISMRM, Toronto, 2015.

Contents

Chapter 1

Introduction

1.1 Motivation: Why does relaxometry matter?

The signal intensity and contrast in conventional proton magnetic resonance imaging (MRI) is predominantly governed by the proton density and relaxation times of the tissues being imaged. In order to ensure clinically acceptable scan times, MR experiments are often restricted to a qualitative (or weighted) rather than quantitative assessment of tissue-specific parameters. In such weighted imaging, the same tissue of the same subject can exhibit different signal intensities in different data sets depending on the MR sequence used and the available hardware (type and set-up of the scanner, radiofrequency (RF) coils). In the clinical routine, the appearance of a particular tissue type in the acquired weighted MR image is commonly referred to as being 'hyperintense' or 'hypointense' relative to another region. Intensity differences in weighted MRI do not provide a quantitative measure of tissue alterations and are prone to visual illusion effects (see Fig. 1.1). As a consequence, weighted imaging is less specific in tissue characterization and may have reduced sensitivity to detect global pathological tissue changes compared to quantitative approaches.

So far having been mainly viewed as a process for obtaining qualitative anatomical images, MRI may in the future increasingly be used as a scientific instrument to measure clinically relevant quantities, i.e. MR parameters which are altered in disease. Measurement science has a long tradition in human history starting from early quantitative methods focused on measuring distance, mass, monetary value, or time. In 1883, the desire to quantify was described by Lord Kelvin, giving a lecture on electrical units of measurement, with the words [1]:

> *[...] when you can measure what you are speaking about, and express it in numbers, you know something about it; but when you cannot measure it, when you cannot express it in numbers, your knowledge is of a meagre and unsatisfactory kind: it may be the beginning of knowledge, but you have scarcely, in your thoughts, advanced to the stage of science, whatever the matter may be.* [2]

This statement has been remained valid nowadays motivating the move of qualitative MRI towards a quantitative assessment of the imaged object.

Quantitative MRI is a promising tool to isolate particular tissue properties without the confounding influence of other MR parameters. The obtained parametric maps calculated from typically two or more MR images of the same anatomical region are expressed in absolute physical units and are ideally independent of the MR protocol as well as hardware. Determination of tissue-specific parameters in a quantitative way enables to directly compare MR images across subjects as well as to assess pathological tissue changes in longitudinal and multi-center studies. However, in practice, MR quantification techniques require significant measurement time, show residual sensitivity to the protocol parameters, are impaired by system imperfections, and the provided information is typically limited to a single parameter at a time. Research in quantitative MRI thus focuses on the development of fast data acquisition and postprocessing techniques for accurate and precise multiparametric mapping of tissue properties.

The most fundamental quantitative fingerprints of MRI are the longitudinal and transverse relaxation times (T_1 and T_2) which reflect the biophysical and biochemical

Figure 1.1: Optical illusion illustrating why quantitative MR techniques are superior to conventional weighted imaging: the square on the left-hand side appears to be brighter compared to the square on the right. This appearance is a consequence of the left square appearing 'hyperintense' relative to its surrounding area while the right one appearing 'hypointense' in its environment. In fact, the color of the two squares is exactly the same. This illusion can be eliminated by quantitative MRI.

properties of tissues at a submicroscopic level. In 1971, Damadian [3] attracted the attention of the medical community by his work on tumor detection in animals using relaxation time measurements based on a phenomenon called nuclear magnetic resonance (NMR). He was the first to report that normal and pathological tissues can be distinguished by means of NMR relaxation time quantification (also referred to as relaxometry). Ever since, relaxometry has gained paramount importance and proved to fundamentally advance the diagnostic power of MRI.

In several studies, relaxation time measurements have demonstrated potential impact for the early diagnosis and progression monitoring of diseases in the human brain, body, and heart. Brain pathologies are often observed to be associated with an increase in the longitudinal and transverse relaxation times. Relaxation time prolongation in the brain has been reported in numerous contexts, e.g. in studies concerning autism, dementia, Parkinson's disease, multiple sclerosis, epilepsy, stroke, and tumors.

In the body, measurements of transverse relaxation times (T_2 and T_2^*) have proven value for the assessment of iron accumulation, e.g. in the liver, pancreas, spleen, and kidney. Iron overload occurs in many pathologies and results in a shortening of the relaxation times compared to those in healthy tissue. Furthermore, MR relaxometry is an established method for the evaluation of cartilage disease and has shown ability to detect early chondral abnormalities. In addition to providing a quantitative measure for early diagnosis, relaxation time mapping techniques are widely used to follow cartilage repair treatment. In cardiac applications, relaxation time measurements are beneficial for assessing cardiac iron overload, myocardial infarction, edema, and hemorrhage. Beside tissue characterization, accurate knowledge of T_1 is important for contrast agent uptake studies as well as for the measurement of perfusion and blood volume. A comprehensive review of the medical relaxometry applications with many relevant references is given in Ref. [4].

1.2 Relaxation processes

The process of nuclear magnetic resonance (NMR) upon which MRI is based involves the interaction of atomic nuclei with an externally applied static (main) magnetic field B_0. Many different nuclei can undergo NMR such as for example those from carbon (^{13}C), nitrogen (^{15}N), fluorine (^{19}F), sodium (^{23}Na), phosphorus (^{31}P), and

most importantly for in vivo MR applications the hydrogen nucleus which consists of a single proton. In order to exhibit NMR, the atomic nucleus must possess a non-zero spin associated with a magnetic moment. The spin is a fundamental quantum mechanical property and the principles of NMR can thus only be fully understood by means of quantum mechanics. Due to its abundance in water and fat which are major constituents of living tissues, the hydrogen nucleus is the most frequently imaged atomic nucleus in clinical MRI. It possesses a half-integer spin of 1/2, i.e. according to quantum mechanics, it is allowed to occupy only two possible energy levels.

For the scope of this work, a classical treatment of NMR based on the Bloch equation extended with terms to include the processes of relaxation in a phenomenological way is sufficient [5]. Classically, the protons can be considered as small magnets which tend to align along the direction of the applied static magnetic field. This process is counteracted by thermal energy which tends to randomly orient the protons and to destroy the alignment. In the established equilibrium obeying Boltzmann statistics, a small excess of spins which are aligned with the magnetic field is produced. The resulting net bulk magnetization $\vec{M}$ is used to generate the MR signal. Its evolution over the time t is described by the Bloch equation which is, as a result, also referred to as the equation of motion of magnetization.

In order to produce transverse magnetization components which generate the MR signal, the magnetization $\vec{M}$ is excited, i.e. rotated away from its equilibrium direction, by means of RF radiation with carrier frequency close to the Larmor frequency ω_0 of the hydrogen protons. After the application of an RF pulse, two characteristic relaxation processes take place which are empirically determined and drive the magnetization back to the equilibrium – denoted longitudinal (T_1) and transverse (T_2) relaxation.

The analysis below follows Refs. [6] and [7], and is valid in a reference system (x, y, z) with unit vectors $(\hat{x}, \hat{y}, \hat{z})$ that rotates around the direction of B_0 ($\vec{B}_0 = B_0\hat{z}$) with the Larmor frequency $\omega_0 = \gamma B_0$ (γ: gyromagnetic ratio, for protons: $2\pi\cdot(42.6\cdot10^6)$ rad/(s·T)). In this rotating reference system (also referred to as Larmor reference frame or B_0 reference frame) the precession of the magnetization due to B_0 is not seen.

1.2.1 Longitudinal relaxation time: T_1

The regrowth of the longitudinal magnetization component M_z after the excitation of the spin system is determined by a characteristic time constant T_1. The spins of the protons try to realign with B_0 by releasing the energy which they absorbed from the RF pulse through interaction with the surroundings (spin-lattice interaction). As energy is transferred away from the spins to the lattice, M_z relaxes back to the equilibrium value M_0. This results in the following equation of motion for M_z:

$$\frac{dM_z(t)}{dt} = \frac{M_0 - M_z(t)}{T_1}. \tag{1.1}$$

For a starting value of $t = 0$, the solution of Eq. (1.1) is found as

$$M_z(t) = M_z(0)\exp(-t/T_1) + M_0(1 - \exp(-t/T_1)). \tag{1.2}$$

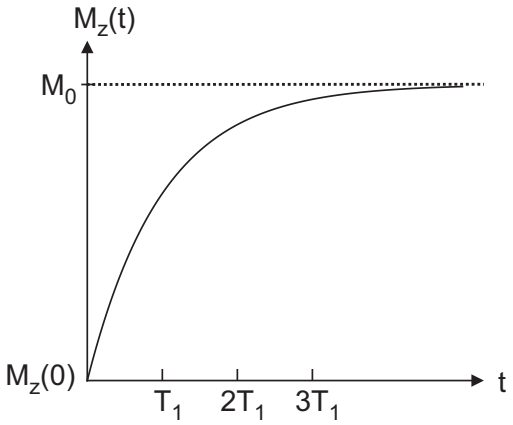

Figure 1.2: Exponential recovery curve of the longitudinal magnetization component $M_z(t)$ from $M_z(0)$ back to the equilibrium value M_0. (adapted from Ref. [6])

The exponential regrowth from the initial value $M_z(0)$ to M_0 is illustrated in Figure 1.2. The longitudinal relaxation time T_1 ranges from hundreds to thousands of milliseconds for protons in human tissues and fluids at clinically relevant field strenghts (1.5 – 3 Tesla). It is also referred to as spin-lattice relaxation time.

1.2.2 Transverse relaxation time: T_2

Simultaneously with the recovery of the longitudinal magnetization, the transverse component $\vec{M}_\perp = M_x\hat{x} + M_y\hat{y}$ relaxes back to zero with the characteristic decay time T_2. An important mechanism driving the reduction in $\vec{M}_\perp$ is the loss of the phase coherence between the spins, also called dephasing. The individual spins dephase in time as they experience locally varying fields which are a combination of the static magnetic field B_0 and the fields produced by their neighbors resulting in different precessional frequencies. No energy is lost through these spin-spin interactions but redistributed within the spin system. In many textbooks, the relaxation parameter T_2 is referred to as spin-spin relaxation time. The equation of motion for $\vec{M}_\perp$ is given by

$$\frac{d\vec{M}_\perp(t)}{dt} = -\frac{\vec{M}_\perp(t)}{T_2} \tag{1.3}$$

with the solution

$$\vec{M}_\perp(t) = \vec{M}_\perp(0)\exp(-t/T_2) \tag{1.4}$$

for a starting point of $t = 0$. An illustration of this exponential decay from the initial value $\vec{M}_\perp(0)$ to zero is presented in Figure 1.3. As not only the collective dephasing of the spins contributes to the relaxation of $\vec{M}_\perp$ but also the spin-lattice couplings giving rise to T_1 effects, the decay constant T_2 is considerably shorter than T_1, typically on the order of tens of milliseconds for protons in living tissues and on the order of seconds for fluids (for the clinically relevant B_0 range).

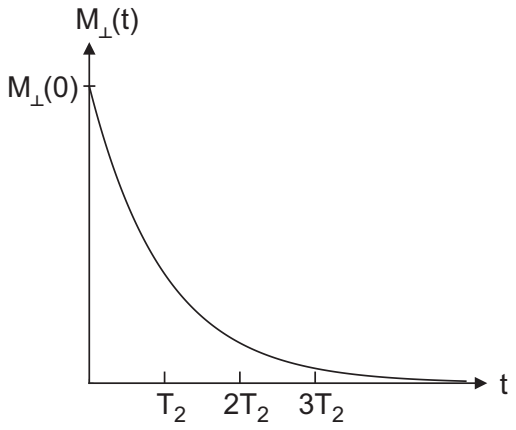

Figure 1.3: Exponential decay curve of the transverse magnetization component $M_\perp(t)$ from $M_\perp(0)$ to zero. (adapted from Ref. [6])

Off-resonance effects such as imperfections in the main magnetic field, susceptibility differences among various tissues or at tissue-air interfaces, and chemical shift lead to an additional dephasing of the spins and thus to a faster decay of the bulk magnetization $\vec{M}_\perp$. This additional reduction in transverse magnetization can be characterized by a separate time constant T_2'. The overall transverse relaxation time T_2^* is then determined by

$$\frac{1}{T_2^*} = \frac{1}{T_2} + \frac{1}{T_2'}. \tag{1.5}$$

The T_2'-induced dephasing can be eliminated by the application of an appropriate pulse (180° pulse in a spin-echo MR sequence) which effects a rephasing of the spin and thus a reversal of the initial dephasing. In contrast, the T_2 losses internal in the proton system are not recoverable as they are caused by local, random, and time-dependent field variations.

1.2.3 Bloch equation including relaxation

The Bloch equation in its general form is given by

$$\frac{d\vec{M}}{dt} = \gamma(\vec{M} \times \vec{B}). \tag{1.6}$$

In MR imaging, three different magnetic fields are relevant which add up to $\vec{B}$:

- the external static magnetic field B_0, pointing in z direction: $B_0\hat{z} + \vec{\delta}B$ ($\vec{\delta}B$: field inhomogeneity)
- the gradient field, here assumed to point in z direction for convenience: $(\vec{G}\cdot\vec{r})\hat{z}$ ($\vec{r}$: position vector, $\vec{G}$: magnetic field gradient)
- the magnetic component of the RF field: $\vec{B}_1$

In the rotating reference frame where the precession due to B_0 is eliminated and by neglecting the B_0 field inhomogeneity $\vec{\delta}B$, the matrix formulation of the Bloch equation including the relaxation terms presented in Eqs. (1.1) and (1.3) is then found as [7]

$$\frac{d\vec{M}}{dt} = \begin{pmatrix} -1/T_2 & \gamma\vec{G}\cdot\vec{r} & -\gamma B_{1y} \\ -\gamma\vec{G}\cdot\vec{r} & -1/T_2 & \gamma B_{1x} \\ \gamma B_{1y} & -\gamma B_{1x} & -1/T_1 \end{pmatrix} \begin{pmatrix} M_x \\ M_y \\ M_z \end{pmatrix} + \begin{pmatrix} 0 \\ 0 \\ M_0/T_1 \end{pmatrix}. \tag{1.7}$$

For the derivation of Eq. (1.7), it was assumed that the z component of the RF field $\vec{B}_1$ can be neglected as compared with the static magnetic field: $B_1 \sim 10^{-5}B_0$ [7]. Eq. (1.7) builds the basis for designing MR imaging methods and RF pulses.

1.3 Gold standard T_1 and T_2 measurement techniques

The current gold standard methods for measuring T_1 and T_2 are based on sampling the complete T_1 recovery and T_2 decay curves, respectively (cf. Figs. 1.2 and 1.3). They are described in the following subsections assuming that the tissue of interest has a single T_1 and a single T_2 component, and including a sketch of the underlying MR sequences, i.e. the RF and gradient waveform patterns needed to obtain images with a contrast that is sensitive to T_1 or T_2. The three orthogonal logical axes along which the imaging gradients are played out are denoted throughout this work consistently as slice-selection, phase-encoding, and frequency-encoding axes abbreviated by G_{SS}, G_{PE}, and G_{FE}, respectively.

1.3.1 T_1 measurement using inversion recovery sequences

The principles for the current gold standard T_1 measurement technique were developed from NMR experiments by Drain [8] and Hahn [9] in the late 1940s. In contemporary quantitative MRI, the classical gold standard T_1 mapping method is based on a series of n inversion recovery (IR) measurements with varying inversion times (TI_n). The underlying MR sequence is depicted in Figure 1.4 and consists of an IR module followed by a self-contained host pulse sequence such as an RF spin echo, gradient echo, or variants of them. The first pulse of the sequence inverts the longitudinal magnetization M_z. Typically, a flip angle of 180° is used to yield a complete inversion of M_z. During a time delay, known as the inversion time TI, the inverted magnetization relaxes back towards the equilibrium value M_0 according to Eqs. (1.1) and (1.2). The recovery is governed by the characteristic time constant T_1, cf. Section 1.2.1. The different recovery rates of tissues with different T_1 values result in a T_1 contrast. The second pulse excites the recovered longitudinal magnetization and tips it into the transverse plane for measurement (typically, a flip angle of 90° is used), thus converting the differences in M_z into differences in $M_\perp$.

The relaxation time T_1 can be estimated from sampling the complex MR signal S_n at n different time points TI_n. The acquired signal S_n depends on the sequence parameters, the intrinsic time constant T_1 and proportionality factors incorporating the proton density, the coil sensitivity, and T_2 (spin-echo host sequence) or T_2^* (gradient-echo host sequence) relaxation. Analytical expressions for the signal intensity pro-

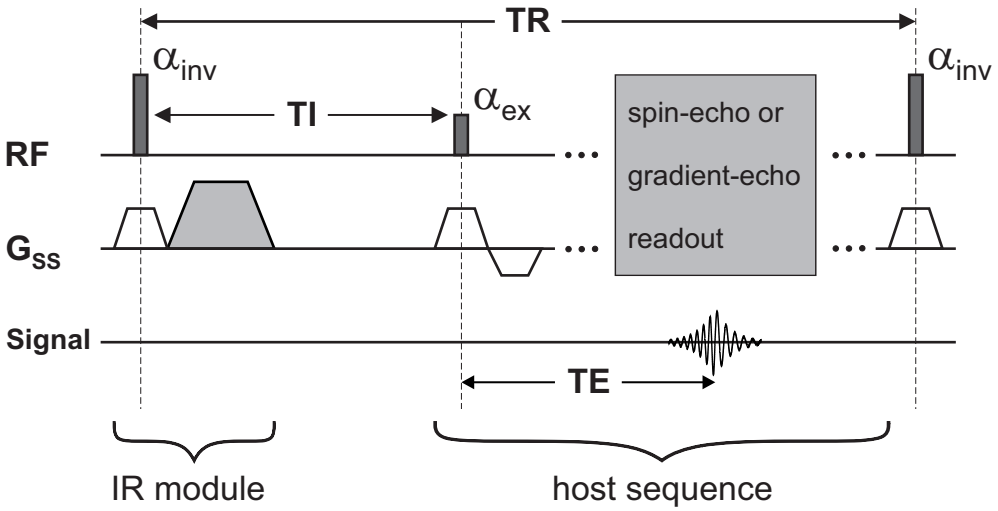

Figure 1.4: A generic inversion recovery (IR) pulse sequence. After the time delay TI (inversion time), the RF inversion pulse (α_{inv}, here a spatially selective inversion pulse is depicted, but non-selective inversion pulses can also be used) is followed by an RF excitation pulse (α_{ex}) and a spin-echo or gradient-echo based readout in order to sample the signal at time TI + TE (TE: echo time). Typically, the inversion pulse is followed by a spoiler gradient (gray-colored gradient area along $\mathrm{G_{SS}}$) to eliminate any residual transverse magnetization. A long repetition time (TR) on the order of seconds (2 – 12 s) is required to allow adequate recovery of the longitudinal magnetization. (adapted from Ref. [14])

duced by the inversion recovery sequence using a spin-echo host and a gradient-echo host can be found for example in Ref. [10], Eq. (1) and Ref. [11], Eq. (8), respectively, where instantaneous RF pulses, perfect spoiling of $M_\perp$ after the application of the inversion pulse, and negligible effect of off-resonances were assumed. From these signal expressions, it is seen that an estimate for T_1 can be obtained by fitting the acquired data to the five-parameter model [12, 13]:

$$S_n = a + b \cdot \exp(-\mathrm{TI}_n/T_1) \tag{1.8}$$

where a and b are complex-valued parameters, and T_1 is real-valued yielding five free fitting variables. Frequently, simplifications of Eq. (1.8) are made resulting in the four-parameter model:

$$S_n = c \cdot (1 - (1 - \cos\alpha_{\mathrm{inv}})\exp(-\mathrm{TI}_n/T_1)) \tag{1.9}$$

or in the three-parameter model (with known TR):

$$S_n = c \cdot (1 - 2 \cdot \exp(-\mathrm{TI}_n/T_1) + \exp(-\mathrm{TR}/T_1))\,. \tag{1.10}$$

The parameter c is a complex-valued constant in Eqs. (1.9) and (1.10). In Eq. (1.9), the flip angle of the inversion pulse (α_{inv}) is considered as a free fitting parameter to account for imperfect inversion. The model relies, however, on the assumption that

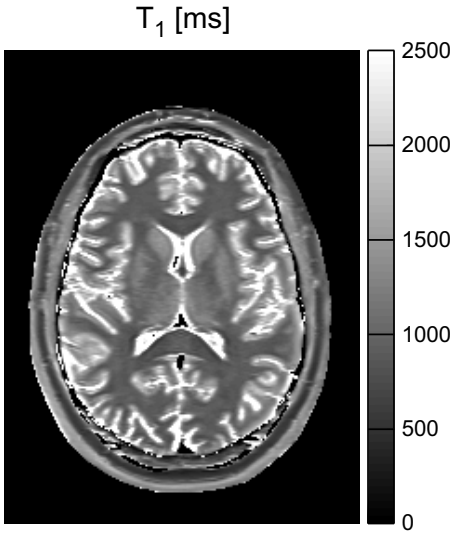

Figure 1.5: Representative axial T_1 map obtained in the human brain at 3 Tesla using a single-slice IR spin-echo sequence (parameters: TR = 10 s, TE = 15 ms, TI = {200, 400, 800, 1600, 3200} ms) and by fitting the real-valued data to a mono-exponential three-parameter model. The acquisition protocol was optimized for human brain tissue T_1 quantification. Values of zero in the ventricles (CSF) resulted due to thresholding adapted to brain tissues.

TR is infinitely long, in particular TR >> T_1. If TR is not sufficiently long, the issue of saturation where M_z does not have enough time to fully recover to the equilibrium value M_0 has to be considered and Eqs. (1.8) or (1.10) should be preferred. Eq. (1.10), on the other hand, assumes a perfect inversion pulse (180°) which, in practice, can not be achieved. Nevertheless, the models given in Eqs. (1.9) and (1.10) are attractive owing to the increased signal-to-noise ratio (SNR) in the fitted value of T_1 due to less fitting parameters as compared to Eq. (1.8) [15, 16].

If only real-valued or magnitude data are available from the MR system, T_1 can be estimated by appropriately adapting the models given in Eqs. (1.8)-(1.10). In the case of real-valued data sets, large systematic errors may arise due to phase aberrations. These errors can be reduced by using a phase-corrected real reconstruction [17]. In magnitude data sets, the issue of phase artifacts can be avoided, but the information about the polarity of the signal is lost and has to be restored in order to avoid ambiguity in the interpretation of the signal points which are close to zero along the IR curve [18].

In Figure 1.5, a representative T_1 map of an axial slice in the human brain obtained at 3 Tesla using a single-slice IR spin-echo sequence with varying inversion times and fitting the real-valued data to a mono-exponential three-parameter model is shown. The gold standard method for measuring T_1 has in general the potential to offer accurate and precise T_1 quantification but it is also limited by several instrumental factors such as noise, RF pulse amplitude errors, bi-exponential recovery of the longitudinal magnetization induced by magnetization transfer effects [19], residual transverse coherences [1], and with regard to clinical use mainly the prohibitive scan

time requirements. The issues of noise, RF pulses, and speed are outlined in more detail in the following.

Noise. The presence of noise can considerably bias the T_1 estimation based on magnitude data sets. Typically, the fitting of the acquired IR data is performed using nonlinear least-squares procedures. However, these algorithms are only optimal for data containing Gaussian distributed noise as it can be assumed for the reconstructed real and imaginary part of the MR data. For magnitude data, however, the proper probability density function is the Rice distribution and care has to be taken as, in this case, least-squares estimation is not a maximum likelihood estimator. Especially in the case of low SNR magnitude data [20], least-squares fitting will yield biased results. This bias can be reduced by using methods based on maximum likelihood parameter estimation [21, 22].

RF pulses. The acquired MR signals depend sensitively on the flip angles of the RF inversion and excitations pulses. In practice, it can not be assumed that the applied pulses have their nominal values (180° and 90°, respectively). RF pulse amplitude errors are considered to be the single most common cause of errors in T_1 measurements [1]. Deviations between the nominal and the actual flip angle may arise due to inhomogeneities in the transmit RF field (B_1) or due to slice-profile effects in the case of slice-selective pulses. Imaging only a single slice to avoid crosstalk between adjacent slices and using non-selective inversion pulses is one way to mitigate the effect of imperfect slice profiles.

Speed. The main limitation of the gold standard T_1 measurement method is the long scan time required in standard IR imaging where TR is kept very long to ensure full recovery of the longitudinal magnetization. In the fast inversion recovery (FIR) technique proposed by Gupta et al. [11], TR is held constant but shorter than $5{\cdot}T_1$ consequently preventing complete recovery of M_z. In this case, the acquired data must be fitted using Eqs. (1.8) or (1.10) to account for saturation. However, even for the FIR sequence, IR T_1 measurement is slow as the TR still needs to be on the order of seconds to allow adequate recovery between the inversion pulses. Because of the long TR required, two-dimensional (2D) imaging is more frequently used than three-dimensional (3D) mode with IR sequences. To accelerate the measurement, fast imaging techniques can be implemented for the host sequence such as echo-planar imaging (EPI) [23] or rapid acquisition with relaxation enhancement (RARE) [24]. In general, accelerating scanning and fitting comes at the expense of accuracy and precision. Even with accelerated measurement techniques, the gold standard IR T_1 mapping method generally comes along with scan time requirements which are not acceptable for daily clinical routine.

In summary, there is a large variation in the way how the underlying MR sequence for the gold-standard T_1 measurement method is implemented and how the acquired data are fitted. There exist attempts to standardize IR-based T_1 estimation. Recently, Barral et al. [12] suggested a standardized protocol that uses non-selective inversion, acquires the complex signal at four time-points, and fits the data to Eq. (1.8). This

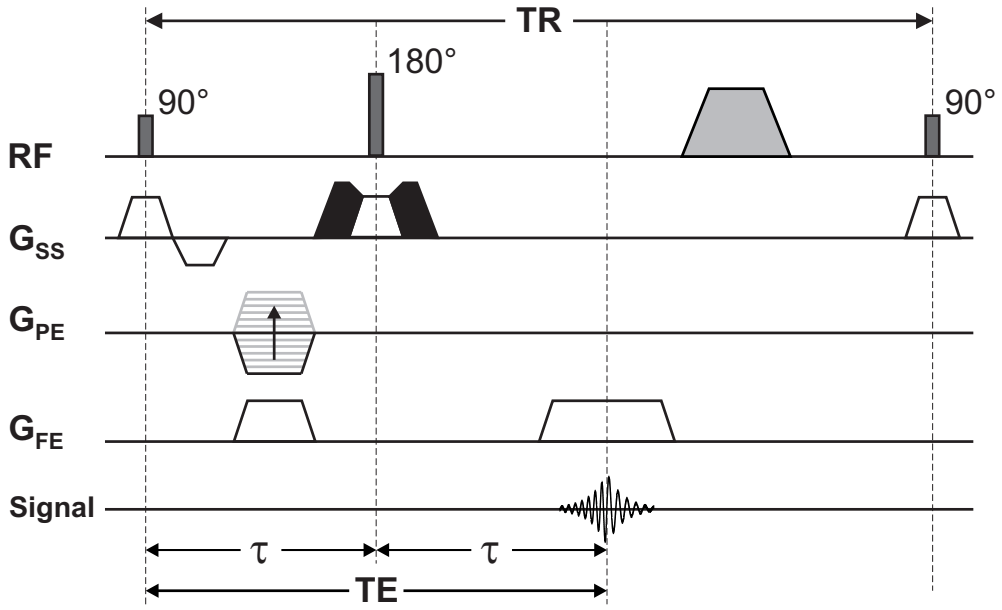

Figure 1.6: A standard single-echo RF spin-echo (SE) pulse sequence consists of a 90° excitation pulse followed by a 180° refocusing pulse. Commonly, a crusher gradient pair played along slice-selection direction accompanies the refocusing pulse in order to remove unwanted signal pathways (black-colored gradient area) and a spoiler gradient played at the end of the slice-selection waveform eliminates residual transverse coherences (gray-colored gradient area). The peak of the echo occurs when the area under the readout gradient equals the moment of the prephasing gradient. Using the timing presented here with TE = 2τ, T_2' weighting can be eliminated. (adapted from Ref. [14])

method is beneficial as it does not assume perfect inversion and excitation pulses, and it does not assume TR >> T_1. It delivers accurate and robust T_1 values, is, however, limited by long scan times and thus not suited for volumetric T_1 mapping in the clinics.

1.3.2 T_2 measurement using spin-echo sequences

The gold standard for measuring T_2 relies on the fundamental RF spin-echo (SE) sequence. The formation of a spin echo was already described in the early days of NMR by Hahn [25]. In the standard single-echo SE sequence as depicted in Figure 1.6, a 90° RF excitation pulse is followed by a 180° refocusing pulse. The excitation pulse tips the longitudinal magnetization into the transverse plane where the spins dephase due to the T_2 and T_2' relaxation mechanisms during the time interval τ until the 180° pulse is applied. It effects a rephasing of the spins owing to a reversal of the T_2' decay as described in detail in Refs. [6] and [14] such that a Hahn spin echo is formed at a time TE = 2τ (see Fig. 1.6). The spin echo does not reverse the effect of the T_2 signal loss arising from rapid local and time-dependent field variations. Therefore, the magnitude of the echo peak will be reduced by the factor $\exp(-\mathrm{TE}/T_2)$ (cf. Eqs. (1.3) and (1.4)) relative to the initial value immediately following the 90° excitation pulse.

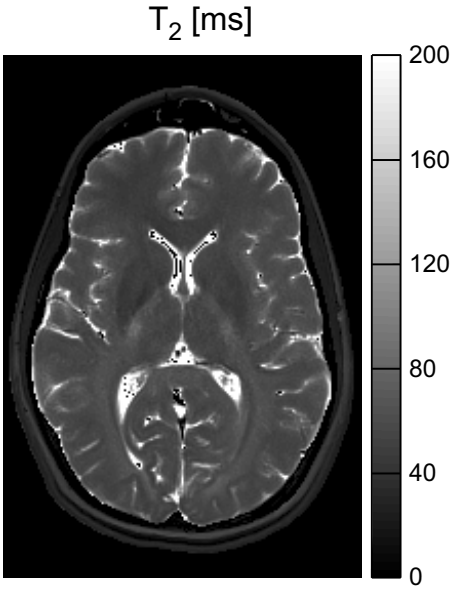

Figure 1.7: Representative axial T_2 map obtained in the human brain at 3 Tesla using single-echo SE acquisitions (sequence parameters: TR = 1410 ms, TE = {20, 40, 60, 80, 100} ms). The MR scan protocol was optimized for human brain tissue T_2 quantification and the acquired magnitude data were fitted to the model given in Eq. (1.12). Values of zero in the ventricles (CSF) indicate locations where proper fitting was not feasible.

The relaxation time T_2 can then simply be measured by performing a series of n single-echo SE experiments with varying echo times TE_n. The magnitude of the signal at the time TE_n is described by

$$S_n = a \cdot \exp(-\mathrm{TE}_n/T_2) \cdot \exp\left(-(2/3)\gamma^2 G^2 D(\mathrm{TE}_n/2)^3\right) + b \tag{1.11}$$

where a is a real-valued proportionality factor and b a real-valued, positive parameter to account for the nonzero mean of the noise floor. The second exponential is the diffusion attenuation term (D: diffusion coefficient, G: arbitrary magnetic field gradient assumed to act throughout the entire duration of the experiment). While a spin-echo experiment can recover the T_2' decay, it does not reverse the dephasing due to diffusion. Provided the echo spacings TE_n are small, the diffusion attenuation term approximates 1, and T_2 can be quantified by using a nonlinear least-squares fit of the simplified model

$$S_n = a \cdot \exp(-\mathrm{TE}_n/T_2) + b. \tag{1.12}$$

Due to the long TR required to ensure full recovery of the longitudinal magnetization within each RF cycle, SE images are typically obtained in 2D mode such that interleaved multi-slice acquisitions strategies can be used [14]. At least five single-echo SE scans are required for proper fitting of the data and thus reliable T_2 estimation. In Figure 1.7, a representative T_2 map is shown as derived in the human brain from a

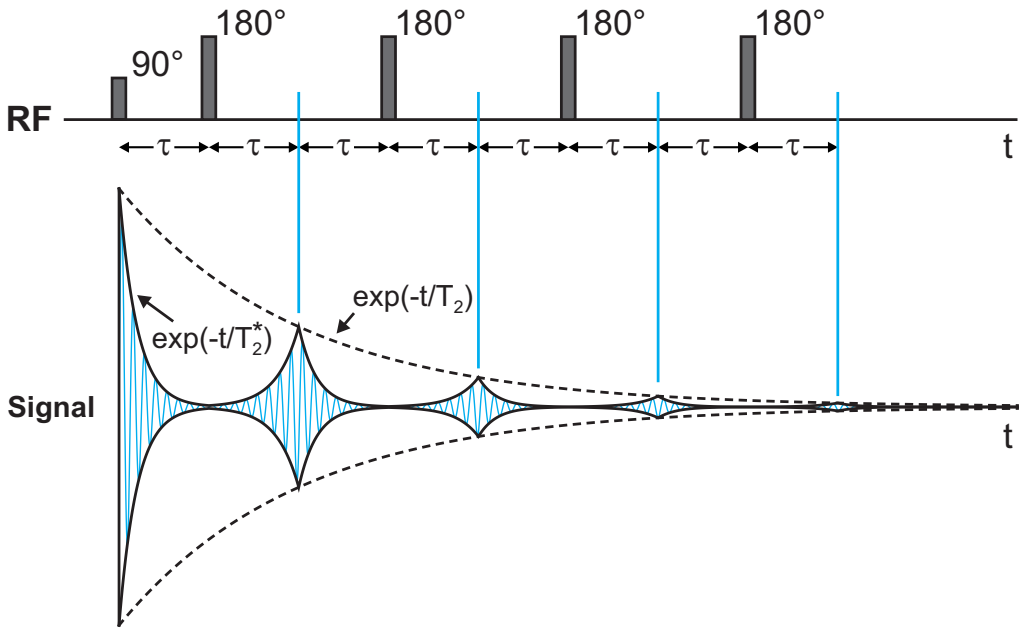

Figure 1.8: Multiple RF spin echoes generated by a train of equally spaced 180° refocusing pulses. While the subsequent echo peaks are modulated by T_2, the formation and decay of the individual echoes is governed by T_2^*. (adapted from Ref. [6])

series of axial single-echo SE acquisitions with varying echo times. As a consequence of the long TR and at least five consecutive scans required, this method is not feasible in the clinical daily routine where time is crucial. In order to accelerate the T_2 measurements, it is popular to use a multi-echo SE technique [26].

In multi-echo SE sequences, multiple 180° refocusing pulses are applied after a single 90° excitation pulse such that the transverse magnetization is repeatedly refocused into a train of spin echoes (see Fig. 1.8). In the initially proposed CP (Carr and Purcell) scheme [27], the RF pulses are played out coherently, i.e. with no phase offset (denoted $90^\circ_x - 180^\circ_x - 180^\circ_x$ ... 180°_x). In this case, any error in the amplitude of the 180° pulses will cumulate over the echo train such that the magnetization vectors giving rise to the RF spin echoes are successively rotated out of the transverse plane.

Imperfections in the refocusing pulse amplitudes can be corrected by using a modified sequence known as CPMG sequence which was developed by Meiboom and Gill [28]. It differs from the CP approach in essentially one aspect: the phases of the excitation and refocusing pulses are offset by 90° (denoted $90^\circ_x - 180^\circ_y - 180^\circ_y$ ... 180°_y). By this means, an accumulation of the errors in the refocusing pulse amplitude over the echo train can be avoided. In particular, the height of the even Hahn spin echoes is not impaired by imperfect refocusing pulses while the odd echoes experience a small but non-cumulative attenuation. Alternatively, a phase-alternated CP sequence (denoted $90^\circ_x - 180^\circ_x - 180^\circ_{\bar{x}} - 180^\circ_x - 180^\circ_{\bar{x}}$ ...) where the phases of the refocusing pulses are switched by 180° can also be used to compensate refocusing pulse amplitude errors. Using CPMG or phase-alternated CP, optimal T_2 accuracy is obtained by fitting only the even echoes. This, in turn, results in the need to double the echo train and

prolongs the measurement time. Additionally to the use of phase cycling (CPMG or phase-alternated CP), it can be beneficial in terms of accuracy to use single-slice acquisitions with non-selective refocusing pulses to minimize systematic errors arising from slice profile effects.

As in the case of the gold standard IR T_1 measurement method, care has to be taken in the presence of noise. Least squares fitting to the model given in Eq. 1.12 introduces a systematic bias into T_2 estimation of low-SNR magnitude data obtained from single-echo or multi-echo SE scans owing to the fact that magnitude data sets obey a Rice distribution and not a Gaussian distribution (see also the previous Section 1.3.1). More crucial, multi-echo SE T_2 measurements are severely impaired by stimulated echo contamination.

Stimulated echoes. RF pulse amplitude imperfections lead to the occurrence of stimulated echoes in multi-echo SE imaging. These unwanted signal pathways interfere with the desired signal pathway of the Hahn echoes [14] and may severely impair T_2 quantification. Since the formation of stimulated echoes requires at least three RF pulses, stimulated echo contamination can be avoided by measuring T_2 based on single-echo SE sequences where only two RF pulses are employed within each TR. This method is, however, too time-consuming for the clinical routine and stimulated echo contributions can thus be considered as major hindrance in the development of rapid and accurate SE-based T_2 measurements techniques.

1.4 Rapid imaging using steady-state sequences

The gold standard T_1 and T_2 estimation methods using conventional IR and SE sequences generally offer accurate results provided they are properly conducted in consideration of the potential error sources as outlined in Sections 1.3.1 and 1.3.2. However, their prohibitive scan time requirements make them not suited for the clinical practice. Any speeding up of the acquisition or fitting procedures comes at the cost of systematic errors which may severely impair the relaxation time measurements (cf. Sections 1.3.1 and 1.3.2).

Another approach for measuring T_1 and T_2 relaxation times which is receiving increased interest is based on a class of rapid gradient-echo (GRE) MR sequences referred to as steady-state free precession (SSFP) sequences. GRE-based pulse sequences do not employ the 180° refocusing pulse that is used to form an echo in SE sequences. Instead, the spin isochromats are dephased and rephased by gradients along the frequency-encoded axis to form the echo. As a consequence, GRE images are weighted by the factor $\exp(-\mathrm{TE}/T_2^*)$, instead of $\exp(-\mathrm{TE}/T_2)$ as SE images. Furthermore, the flip angle of the excitation pulse is typically far lower than 90° such that no lengthy time is needed for T_1 recovery and the repetition time TR can be kept short. In particular, if $\mathrm{TR} << T_1$, the longitudinal magnetization is prevented from returning back to the thermal equilibrium. If in addition $\mathrm{TR} \leq T_2$, the transverse magnetization does not decay to zero. Each RF excitation pulse then acts on both longitudinal and transverse magnetization components. As initially described by Carr [29] and in the 1960s and 1970s by Ernst and Anderson [30], Freeman and Hill [31],

and Hinshaw [32], a dynamic equilibrium or steady state can be established after a certain number of consecutive RF pulses. In order to reach a homogeneous steady state, the following conditions must be fulfilled [33–35]:

- The repetition time TR of the sequence must be constant.
- The flip angle α of the excitation pulse must be constant.
- The dephasing from the gradients within TR must be constant.
- The phases θ_k of the RF pulses must satisfy the equation: $\theta_k = a + bk + ck^2$, where a, b, and c are arbitrary constants.

The spatial distribution of the longitudinal and transverse magnetization vectors in the steady state can also be described as a distribution of different 'configurations' (or 'states' or 'coherences') in k-space characterized by their dephasing state. The theory of such steady-state configurations was originally developed in the context of NMR diffusion experiments [36, 37], and reintroduced by Hennig [38] and Scheffler [35] for the description of the steady-state signal amplitudes acquired in rapid MRI. A thorough derivation of how the bulk magnetization vector can be partitioned into configurations is given in Ref. [7]. A powerful tool for depicting and understanding the echo generation in SSFP sequences (and more general in a broad variety of MR sequences) based on configuration states is provided by the extended phase graph (EPG) concept [39].

As a result of the complex superposition of longitudinal and transverse magnetization states, the measured steady-state signal amplitudes show a complicated functional dependence on the protocol-specific extrinsic parameters (TR, TE, α, the RF phase difference increment φ, the gradient switching pattern), on the tissue-specific intrinsic parameters (T_1, T_2, diffusion) and on physiological effects (flow). Due to the use of short TR and the resulting acquisition speed, steady-state free precession imaging is widely performed in 3D mode. Overall, SSFP sequences can broadly be classified as follows:

- ***Incoherent (spoiled):*** The transverse magnetization components are disrupted (spoiled) prior to the next RF pulse.
- ***Coherent:*** The transverse coherences are preserved.

The second class can further be subdivided into ***nonbalanced*** and ***balanced*** SSFP sequences. The term 'nonbalanced' is used to indicate that in this type of sequence dephasing gradients are present, i.e. the net total gradient moment along at least one axis is not zero. The term 'balanced' indicates that the gradient moments are fully rephased within TR along all axes. In this thesis, the signals produced by spoiled and nonbalanced SSFP sequences and their functional dependencies on relaxation are exploited for T_1 and T_2 relaxometry. The three different types of SSFP sequences are explained in more detail in the following subsections in order to allow the reader to review and compare the characteristics, advantages, and drawbacks of these sequences. The derived steady-state signal amplitudes rely on the assumption of single-component relaxation.

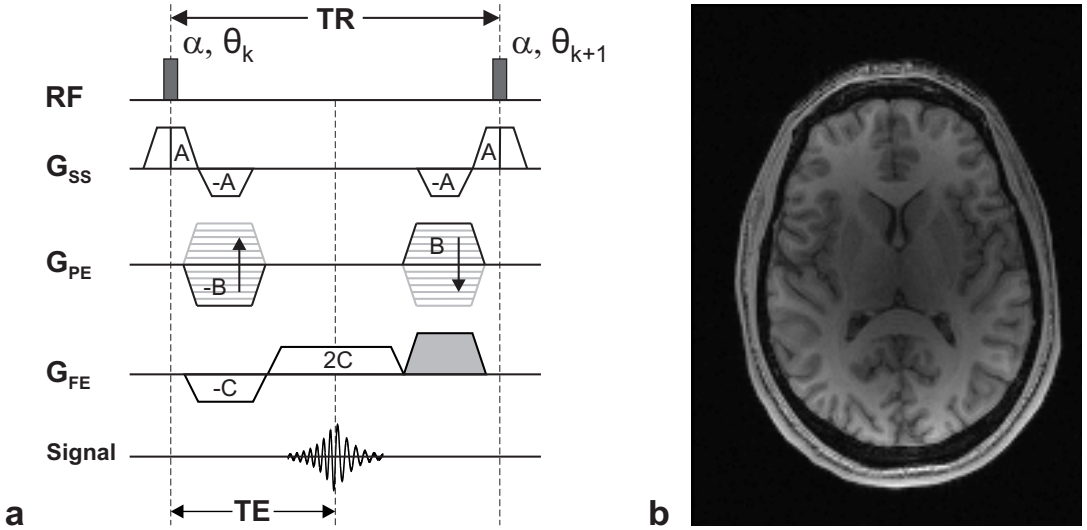

Figure 1.9: (a) Spoiled gradient-echo sequence. The gradient moments along the slice-selection and phase-encoding axes are nulled. Along the frequency-encoding axis, a spoiler gradient is played out and RF phase cycling is used according to Eq. (1.14) in order to maximize the spoiling efficiency of the sequence. Note that in 3D mode, a phase-encoding gradient (and a rewinder gradient) is applied additionally along slice-selection direction (not illustrated). (b) Representative image obtained from axial RF-spoiled 3D SPGR imaging in the human brain at 3 Tesla with TR = 7.6 ms, $\alpha = 18°$, and an isotropic resolution of 1.33 mm showing a contrast governed by T_1.

1.4.1 Spoiled gradient echo

In incoherent (spoiled) gradient-echo imaging, the transverse magnetization is assumed to be zero before each RF pulse. In this case, no residual transverse coherences contribute to the steady-state signal and the acquired images are characterized by a pure T_1 contrast without confounding influence of T_2. The steady-state signal from a perfectly spoiled gradient-echo (SPGR) acquisition immediately after the RF pulse is described by the Ernst equation [40]

$$S_{\text{spoil}} = M_0 \cdot \frac{1 - E_1}{1 - E_1 \cdot \cos\alpha} \cdot \sin\alpha \tag{1.13}$$

with $E_1 := \exp(-\text{TR}/T_1)$. The flip angle α_E which maximizes the signal in Eq. (1.13) is known as Ernst angle and given by: $\alpha_E = \cos^{-1}(E_1)$.

In practice, it is challenging to eliminate all residual transverse magnetization components prior to the next RF pulse. Effective spoiling can be achieved by using a long TR of about at least three times T_2 so that the transverse magnetization decays nearly to zero. For rapid 3D acquisitions, this approach is impractical and a different spoiling strategy has to be found. It was proven that for TR < T_2, a homogeneous steady state can be reached if sufficiently strong spoiler gradients are combined with an RF phase cycling condition (RF spoiling, see Fig. 1.9 a) such that the differences

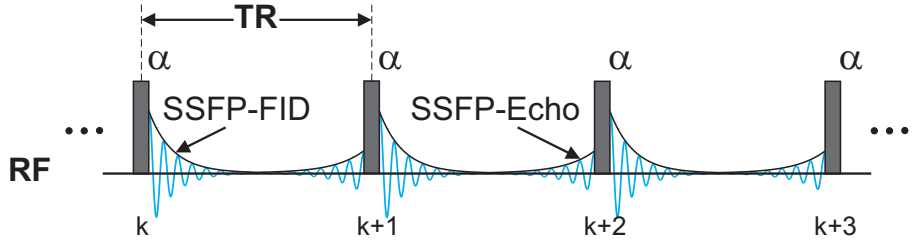

Figure 1.10: Illustration of the transverse steady state in short-repetition time sequences. Just after each RF pulse, a FID-like signal forms (SSFP-FID). Just before each pulse, a time-reversed FID signal occurs (SSFP-Echo). (adapted from Ref. [14])

between the phases θ_k of consecutive RF pulses are linearly incremented: [33]

$$\theta_k - \theta_{k-1} = \varphi_0 + k\varphi \tag{1.14}$$

where φ_0 can be chosen arbitrarily and φ is the phase shift (difference) increment. While the value of φ_0 does not affect the steady state, the choice of the phase shift increment is crucial. It has to be noted that the steady state of RF-spoiled GRE sequences depends sensitively on φ and may deviate considerably from the ideally spoiled case given in Eq. (1.13). In Ref. [33], it was reported that when φ is 117°, the transverse magnetization prior to each RF pulse is nulled over a wide range of T_1, T_2, and α values in which case the RF-spoiled gradient-echo signal is given to a good approximation by Eq. (1.13). An analytical solution for the RF-spoiled GRE steady-state magnetization has been derived in Ref. [41]. An axial sample image obtained from RF-spoiled 3D SPGR imaging in the human brain at 3 Tesla is shown in Fig. 1.9 b.

More details about the difficulty to achieve complete spoiling in practice and how this type of sequence can be used for rapid volumetric T_1 mapping is provided in Chapter 2.

1.4.2 Nonbalanced steady-state free precession

In nonbalanced SSFP imaging, the RF excitation pulses are phase coherent, i.e. they all have the same phase (in contrast to RF-spoiled GRE). The gradient moments along the frequency-encoding axis are not nulled. Instead, they induce a dephasing of 2π per voxel between the excitation pulses. The resulting two types of SSFP signals generated by such a sequence are schematically depicted in Figure 1.10. The steady-state magnetization just after the RF pulse is in the literature referred to as SSFP-FID (or S^+ or F_0). It has contributions from both longitudinal and transverse coherences present before the kth pulse which are rotated into and out of the transverse plane, respectively. The part of the signal originating from fresh longitudinal magnetization is the 'free induction decay' (fid). The steady-state magnetization that forms just before the RF pulse is referred to as SSFP-Echo (or S^- or F_{-1}). It arises due to the transverse coherences present prior to each RF pulse and has a reversed phase distribution compared to the SSFP-FID.

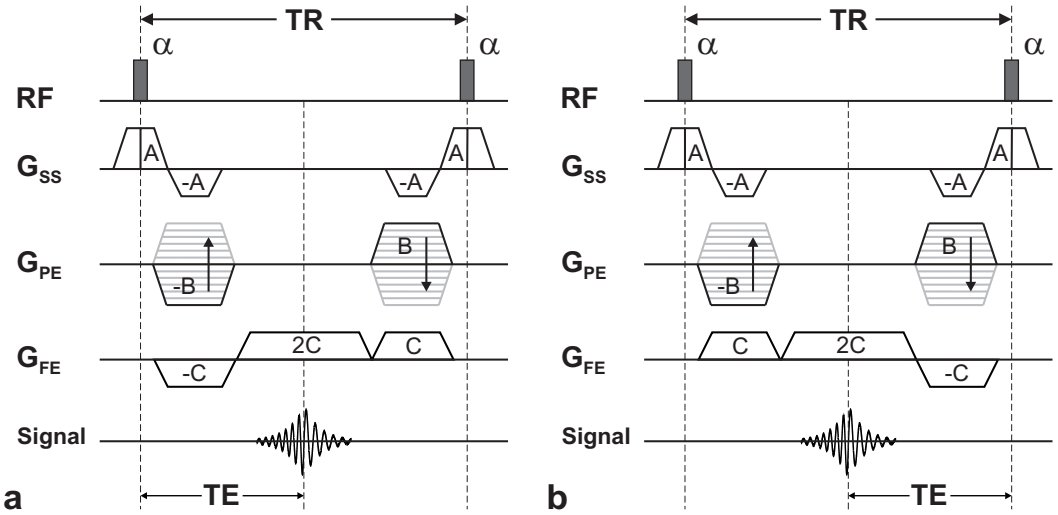

Figure 1.11: The two basic nonbalanced SSFP sequences: the SSFP-FID (a) and the SSFP-Echo (b). This type of sequence employs coherent RF excitation pulses and unbalanced gradient moments along the frequency-encoding axis inducing a dephasing of 2π per imaging voxel. The gradient waveform pattern in frequency-encoding direction can be adapted to acquire either the SSFP-FID (a) or the SSFP-Echo (b). Note that in 3D mode, a phase-encoding gradient (and a rewinder gradient) is applied additionally along slice-selection direction (not illustrated).

Depending on the gradient waveforms along the frequency-encoding axis either the SSFP-FID or the SSFP-Echo signal is acquired. For the acquisition of the SSFP-FID an ordinary bipolar readout gradient is needed (cf. Fig. 1.11 a) whereas the SSFP-Echo is selected for imaging by the time-reversed gradient waveform (cf. Fig. 1.11 b). For this reason, the SSFP-Echo is often termed time-reversed SSFP-FID.

Procedures to calculate the amplitudes of the SSFP-FID and SSFP-Echo signals are described by Zur et al. [42] and Gyngell [43]. Here, the final analytical results of the calculation for the SSFP-FID signal just after and the SSFP-Echo signal just before the pulse as presented by Hänicke and Vogel [44] are given:

$$S_{\mathrm{SSFP-FID}} = M_0 \cdot \tan\frac{\alpha}{2} \cdot (1 - (E_1 - \cos\alpha) \cdot r)\,, \tag{1.15}$$

$$S_{\mathrm{SSFP-Echo}} = M_0 \cdot \tan\frac{\alpha}{2} \cdot (1 - (1 - E_1\cos\alpha) \cdot r) \tag{1.16}$$

with definitions

$$\begin{aligned} E_{1,2} &:= \exp(-\mathrm{TR}/T_{1,2}), \\ p &:= 1 - E_1\cos\alpha - E_2^2(E_1 - \cos\alpha), \\ q &:= E_2(1 - E_1)(1 + \cos\alpha), \\ r &:= (1 - E_2^2)(p^2 - q^2)^{-1/2}. \end{aligned}$$

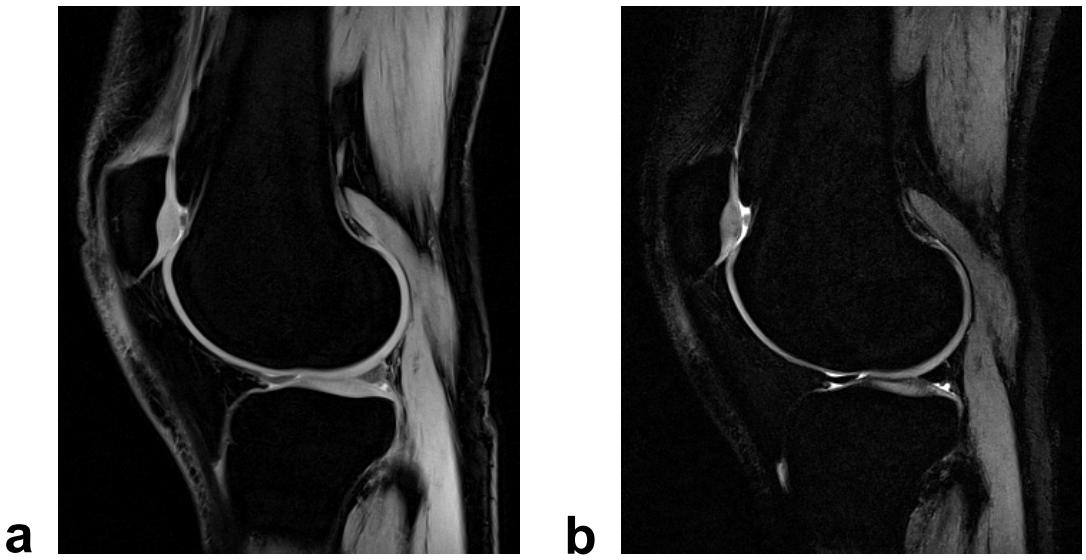

Figure 1.12: Sagittal SSFP-FID (a) and SSFP-Echo (b) sample images acquired with 3D DESS imaging in the knee joint at 3 Tesla. Water-selective pulses were used for excitation. Sequence parameters: TR = 14.19 ms, $\alpha = 15°$, in-plane resolution: 0.4×0.4 mm^2, slice thickness: 2.5 mm. The SSFP-Echo signal intensity was multiplied by a factor of 2 relative to the SSFP-FID amplitude.

In the limiting case TR >> T_2, the SSFP-FID signal amplitude (Eq. (1.15)) converges to the ideally spoiled GRE signal (Eq. (1.13)). In the small flip angle limit, the SSFP-FID signal becomes proton-density weighted similarly to the ideally spoiled case. At fixed protocol parameters (TR, TE, α, etc.), the signal from the SSFP-FID is higher than the ideally spoiled GRE signal due to the transverse coherences present just before the RF pulse which effect an increase of the detected signal. For short TR and intermediate to high flip angles, the SSFP-FID and SSFP-Echo show a mixed T_1 and T_2 contrast. The SSFP-Echo signal is stronger T_2-weighted as can be seen from the ratio of the two SSFP signals at $\alpha = 90°$ (for TR << T_1):

$$\frac{S_{\mathrm{SSFP-Echo}}}{S_{\mathrm{SSFP-FID}}} \approx E_2^2. \tag{1.17}$$

This relationship can be used for quantifying the transverse relaxation parameter T_2. More details about this T_2 estimation method and how the accuracy can be improved for low-flip angle imaging ($\alpha << 90°$) are given in Chapter 3. The acquisition of the SSFP-FID and the SSFP-Echo signal can be combined into one MR sequence which is commonly referred to as double-echo steady-state (DESS) sequence [45, 46] (cf. Chapter 3). Representative SSFP-FID and SSFP-Echo contrasts obtained from 3D DESS imaging in the knee joint at 3 Tesla are shown in Figure 1.12.

It is also possible to acquire higher-order SSFP-FID or SSFP-Echo signals in multi-echo SSFP sequences by extending and expanding the readout gradient as suggested in Ref. [47]. In Chapters 4 and 5, a triple-echo steady-state (TESS) approach is investigated for combined T_1 and T_2 mapping.

A drawback of nonbalanced SFFP sequences is their sensitivity to motion. For spins moving along a magnetic field gradient, steady state can not be attained as their phase accumulated between the pulses varies from TR to TR. As a result, motion artifacts and signal attenuation may occur in nonrigid targets such as the human brain. In Chapter 5, it is shown how rapid 2D acquisitions may overcome this limitation.

In contrast to balanced SSFP (cf. the following Section 1.4.3), nonbalanced SSFP sequences are robust in the presence of off-resonance effects. This property makes them in particular suited for imaging of targets where high susceptibility variations occur as in the musculoskeletal system (cf. Chapters 3 and 4) and for ultra-high field applications (cf. Chapter 5).

1.4.3 Balanced steady-state free precession

In balanced SSFP (bSSFP) imaging, the total gradient area on any axis is zero within each TR as illustrated in Figure 1.13. In this case, the SSFP-FID and the SSFP-Echo rephase at the same time and the balanced SSFP signal can be considered as the coherent sum of the two signals (and all higher-order echoes) [48, 49]. Balanced SSFP yields a high signal if used with sign-alternated RF pulses (i.e. using an RF phase shift increment of 180°). On-resonance, the resulting signal intensity at the echo time TE is given by [50]

$$S_{\mathrm{bSSFP}} = M_0 \cdot \sin\alpha \cdot \frac{1 - E_1}{1 - (E_1 - E_2)\cos\alpha - E_1 E_2} \cdot \exp(-\mathrm{TE}/T_2^*). \tag{1.18}$$

Typically, the bSSFP signal is acquired with TE = TR/2. In this case, the phase evolution of the transverse magnetization in a bSSFP experiment behaves similarly than a spin echo. At TE = TR/2, a complete reversal of the T_2'-related signal decay can be observed (provided the range of different frequencies within a voxel is below $\pm 1/(2\mathrm{TR})$ and T_1, $T_2 > \mathrm{TR}$ [51]). The exponential $\exp(-\mathrm{TE}/T_2^*)$ in Eq. (1.18) can then be replaced by $\exp(-\mathrm{TE}/T_2) = \exp(-\mathrm{TR}/(2T_2)) = \sqrt{E_2}$. Even if the peak of the bSSFP signal is shifted away from the center of the TR, the introduced T_2' weighting is negligible as a very short TR is used in practice.

Since in bSSFP imaging all gradients are fully refocused along any axis, the generated signal is very sensitive to residual phase accumulation within TR resulting from off-resonance effects such as main field imperfections, susceptibility variations or chemical shift. With sign-alternated RF pulses ($\varphi = 180°$), the highest bSSFP signal is achieved on-resonance (cf. Eq. (1.18)). Without sign alternation ($\varphi = 0°$), the signal is minimal on-resonance. The effect of sign alternation on the bSSFP signal is equivalent to the effect of a constant precession of the transverse magnetization by 180° per TR interval in a pulse sequence without sign alternation [32]. As a consequence, a constant resonance offset with an accumulated phase of 180° per TR results in minimal signal intensity in sign-alternated bSSFP sequences. Spatial regions showing such a prominent signal loss are referred to as bands.

The amount of phase accumulation within TR is proportional to the length of TR and the sensitivity of the bSSFP signal to off-resonances can thus be mitigated by using very short TR. In addition, it is stringent to apply a shim in order to reduce inhomogeneities in B_0. As susceptibility variation is inevitable, the most effective way

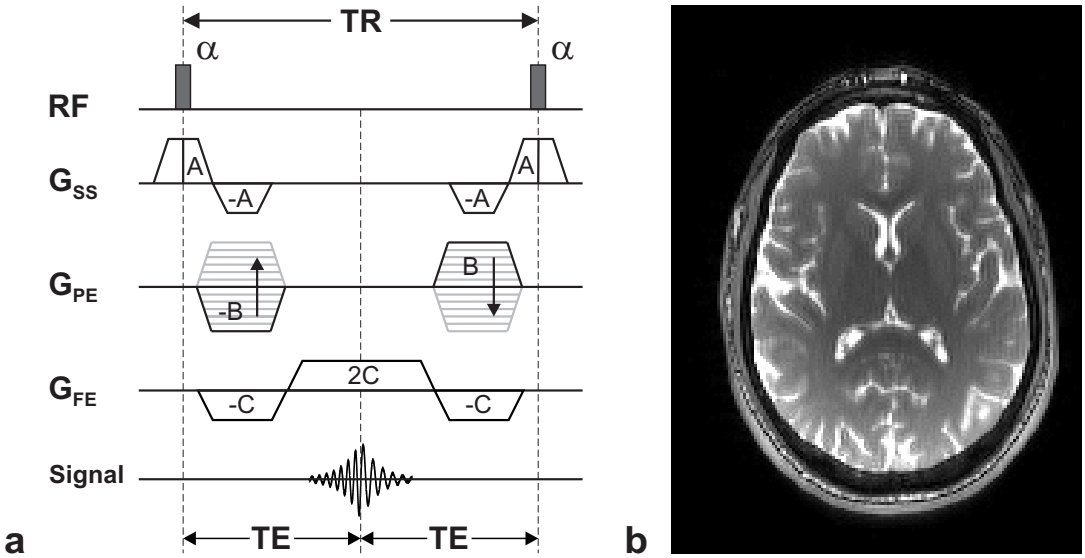

Figure 1.13: (a) Balanced SSFP sequence. The gradients are fully refocused (i.e. have a net gradient area of zero) within TR along all axes. Typically, the bSSFP signal is acquired at TE = TR/2. Note that in 3D mode, a phase-encoding gradient (and a rewinder gradient) is applied additionally along slice-selection direction (not illustrated). (b) Representative image obtained from axial 3D bSSFP imaging in the human brain at 3 Tesla with TR = 3.48 ms, $\alpha = 27°$, and an isotropic resolution of 1.33 mm showing a mixed T_1 and T_2 contrast.

of eliminating banding artifacts in bSSFP is a short TR. Under the assumption of TR << T_2 < T_1 (which is valid for most biological tissues at clinically relevant field strenghts of 1.5 – 3 Tesla and at a TR of 1 – 5 ms), the bSSFP signal equation at TE = TR/2 (cf. Eq. (1.18)) simplifies to [6]

$$S_{\mathrm{bSSFP}} \approx \frac{M_0 \cdot \sin\alpha}{1 + \cos\alpha + (1 - \cos\alpha)(T_1/T_2)} \cdot \exp(-\mathrm{TE}/T_2). \tag{1.19}$$

The signal in Eq. (1.19) is maximal at the optimal flip angle

$$\alpha_{\mathrm{opt}} = \cos^{-1}\left(\frac{T_1/T_2 - 1}{T_1/T_2 + 1}\right) \tag{1.20}$$

with the corresponding signal amplitude

$$S_{\mathrm{bSSFP}}|_{\alpha=\alpha_{\mathrm{opt}}} = \frac{1}{2} M_0 \sqrt{\frac{T_2}{T_1}} \cdot \exp(-\mathrm{TE}/T_2). \tag{1.21}$$

From this equation, it is apparent that the contrast of short-TR bSSFP is essentially T_2/T_1-weighted. If the T_1 and T_2 relaxation times are similar (e.g. for CSF or fat), the optimal signal (cf. Eq. (1.21)) approaches 50 % of the available total equilibrium magnetization M_0. This is an exceptionally high signal for a short-TR steady-state pulse sequence.

Furthermore, bSSFP imaging shows a considerably reduced sensitivity to motion and flow compared to nonbalanced SSFP sequences. For spins moving with constant velocity, steady state can only be retained if the zeroth gradient moment (i.e. the net area under the gradients) is nulled over TR along all axes as in bSSFP imaging [52]. In this case, the dephasing accumulated by the moving spins (under the assumption of constant velocity) is constant within TR. Additionally to zeroth-order gradient moment nulling, the first-order gradient moments along slice-selection and frequency-encoding direction are nulled in bSSFP sequences. As a consequence, spins moving at constant velocity along these axes do not accrue any phase shift during TR. First-order gradient moment nulling is thus also known as velocity or flow compensation.

In summary, bSSFP has the potential to provide the highest signal among all steady-state sequences, and it is less sensitive to motion and flow dephasing compared to nonbalanced SSFP. However, it is limited by its high sensitivity to off-resonances which make it progressively more difficult to implement with increasing strength of the static magnetic field B_0. At higher field strengths, also SAR becomes an issue because of the very short TR used with this type of sequence. The fundamentals of balanced SSFP imaging are reviewed in Refs. [53] and [54].

1.5 Aim of this thesis

Relaxation time measurements have demonstrated value for medical diagnosis and progression monitoring of several diseases. The acquisition times required by the current gold standard methods for accurate quantification of T_1 and T_2 are, however, too long for clinical practice (cf. Section 1.3). Rapid imaging in the steady state using SSFP sequences offers the acquisition of high SNR MR data sets in clinically acceptable scan times (cf. Section 1.4) and is thus a promising tool for relaxation time mapping in the daily clinical routine. Many SSFP-based relaxometry techniques have been proposed in the recent past, but their acquisition speed comes in general at the cost of increased sensitivity to several instrumental factors which adversely affect the quantification accuracy and reproducibility. The most relevant among these factors considered in this thesis are summarized in the following:

Transmit field inhomogeneity. The SSFP signals (cf. Section 1.4) are highly sensitive to the flip angle. Deviations of the actual transmitted flip angle from the nominal prescribed one are thus a major potential error source in SSFP-based relaxometry. Inhomogeneities in the transmitted field B_1 and consequently the flip angle distribution are related to the RF coil geometry, RF attenuation due to tissue conductivity, and the varying dielectric properties of tissues. At high field strength (> 3 Tesla), the RF wavelength in human tissue becomes smaller than the body extensions and dielectric resonance effects develop in the object resulting in a spatially varying RF amplitude and hence flip angle [55]. For accurate relaxometry, additional scans are commonly required in order to map the actual flip angle [56–58].

Imperfect slice profiles. Beside transmit field inhomogeneity, also imperfect slice profiles lead to deviations of the actual from the nominal flip angle. Ideally, the RF

excitation pulse profile should be rectangular producing the desired nominal flip angle across the selected imaging slice or slab. In practice, the actual slice profile is far from ideal. In the case of 3D acquisitions, this effect can be neglected provided the anatomy of interest lies in the center of the imaged volume. In the case of 2D acquisitions, slice profile effects yield varying flip angles through the imaged slice. In order to obtain accurate relaxometry results based on single-slice or multi-slice 2D SSFP imaging, the measured signal has to be considered as a function integrated across the slice profile [59].

Static (main) field inhomogeneity. In principle, the homogeneity of the static magnetic field produced by the empty magnet is very high as hardware imperfections can be well controlled by B_0 shim strategies. However, substantial B_0 field variations causing off-resonance effects are induced by the object inside the magnet due to magnetic susceptibility effects. Susceptibility variations are inevitable and can rarely be eliminated by shimming procedures. In imaging settings where B_0 inhomogeneities are prominent (e.g. in targets with high susceptibility variations or at ultra-high field strengths), spoiled and nonbalanced SSFP techniques may be favored over balanced SSFP as they are highly insensitive to the off-resonance related dephasing of the spins.

Residual coherent transverse magnetization. Accurate T_1 measurements require minimizing T_2 influences. Conventional variable flip angle (VFA) T_1 quantification techniques relying on spoiled gradient-echo imaging usually assume complete spoiling of the transverse magnetization prior to each RF pulse [60, 61]. However, complete elimination of transverse coherences can not be achieved in practice with fast short-TR spoiled GRE imaging. The presence of residual coherent transverse magnetization at the end of the TR interval and its effect on the acquired steady-state signal have to be properly considered in order to yield accurate T_1 relaxometry.

Prior knowledge impairment. In practice, all measured SSFP signals show a mixed dependence on both, T_1 and T_2. Even the spoiled GRE signal which ideally depends purely on T_1, is generally subdue to residual T_2 weighting because of imperfect spoiling. Relaxometry techniques based on SSFP acquisitions thus require prior knowledge about either T_1 or T_2. The existing SSFP methods do commonly not provide proper prior knowledge information for accurate relaxometry. As an example, conventional double-echo steady-state (DESS) T_2 relaxometry entirely neglects the T_1 dependency by using a simplified signal model which introduces a substantial systematic quantification error for low-flip angle imaging [62].

Diffusion. For SPGR imaging, diffusion is a beneficial process since it enhances the spoiling efficiency of the sequence. In nonbalanced SSFP imaging, diffusion causes signal modulations which are in particular prominent in the low-flip angle regime and at high-resolution as a result of the increased dephasing gradient moments[63]. The balanced steady-state signal is not affected by diffusion provided the imaged object is magnetically homogeneous. In practice, the object inside the magnet induces B_0 variations. Diffusion through magnetic field inhomogeneities effects a reduction of the balanced SSFP signal amplitude [64].

Bulk motion and physiological motion. Subject (bulk) motion results in ghosting and blurring artifacts, and overall degrades the image quality. Such artifacts visible in the base images are similarly present in the calculated relaxation time maps. More subtle physiological motion such as cerebrospinal fluid (CSF) pulsations in the human brain or blood flow are of particular concern in nonbalanced SSFP imaging.

Magnetization transfer. Magnetization transfer (MT) refers to the magnetization exchange between protons with free mobility and bound protons with restricted mobility [65]. Due to the very short TR used in combination with rather high flip angles and correspondingly increased specific absorption rate (SAR), MT-related signal modulations are most prominent in balanced SSFP imaging [66, 67].

In this thesis, the clinical need for fast, accurate, and precise T_1 and T_2 relaxometry is attempted to be met by the use of SSFP sequences. The derived new postprocessing and acquisition techniques rely on spoiled and nonbalanced SSFP imaging. The instrumental factors outlined above are addressed in order to achieve highly accurate relaxation time measurements of universal nature, i.e. largely independent of the MR protocol and of the available MR hardware. It has to be noted that the investigated methods assume ***single-component relaxation***, i.e. only a single T_1 and a single T_2 component are assumed to contribute to the signal from each imaging voxel. As the biochemical composition and microstructure of many biological tissues is heterogeneous, the mapped T_1 and T_2 values have to be considered as apparent relaxation times. In particular, techniques are developed in order to substantially reduce or even eliminate the T_2-related bias in conventional T_1 estimation and the T_1-related bias in conventional T_2 estimation. Overall, the aim of this thesis is to contribute a small piece to the search for the common ground in MR relaxometry.

The novel methods are investigated in proof-of-principles studies: first in simulations, then in vitro, and as a last step in healthy volunteers. The results obtained in vitro and in vivo are compared to the gold standard techniques.

1.6 Outline of this thesis

In Chapters 2 and 3, new postprocessing approaches are suggested based on existing T_1 (Chapter 2) and T_2 (Chapter 3) quantification techniques in order to substantially reduce the T_2- and T_1-related bias, respectively, present in the conventional methods. In Chapters 4 and 5, a novel acquisition and postprocessing scheme using a triple-echo steady-state (TESS) sequence is proposed and investigated for simultaneous T_1 and T_2 mapping within a single scan. The T_1 and T_2 calculation is combined into an iterative approach in order to entirely eliminate any confounding influence of either T_2 on T_1 or T_1 on T_2. In more detail, this thesis is concerned with:

Chapter 2. Variable flip angle (VFA) T_1 quantification using 3D RF-spoiled gradient-echo imaging offers the acquisition of whole-brain T_1 maps in clinically acceptable times. Conventional VFA T_1 relaxometry is biased by incomplete spoiling (i.e. resid-

ual T_2 dependency). In this chapter, a new postprocessing approach is proposed to overcome this T_2-related bias. The longitudinal relaxation time T_1 is quantified from the signal ratio of two spoiled GRE images acquired at different flip angles using an analytical solution for the RF-spoiled steady-state signal [41] in combination with a global T_2 guess. The accuracy of T_1 relaxometry is evaluated by means of simulations and in vivo 3D SPGR imaging of the human brain at 3 Tesla.

Chapter 3. Double-echo steady-state (DESS) sequences provide morphological and quantitative T_2 imaging of cartilage within one single scan. Conventional T_2 estimation using DESS is impaired by its prominent T_1 dependency in the limit of low flip angles as generally used to image cartilage morphology. In this chapter, a new postprocessing approach is introduced to overcome this T_1-related bias for rapid DESS-based T_2 quantification in the low flip angle regime. Based on a rough global T_1 estimator and a golden section search, the transverse relaxation time T_2 is extracted from the ratio of the two echoes acquired with DESS. The new relaxometry method is evaluated by means of simulations and in vivo 3D measurements of the knee joint at 3 Tesla.

Chapter 4. Many SSFP-based relaxometry techniques have been proposed, but none are perfect: they are prone to static and transmit field heterogeneities, and commonly biased by either T_2 on T_1 or T_1 on T_2 quantification. In the two previous chapters, it was demonstrated how the T_2- and T_1-bias present in conventional methods can substantially be reduced, however, not entirely be eliminated. This chapter is concerned with the development of a new rapid combined T_1 and T_2 relaxometry method that is completely (T_2) and partly (T_1) bias-free. A triple-echo steady-state (TESS) sequence is investigated in order to acquire in addition to the lowest SSFP-FID (F_0) and SSFP-Echo (F_{-1}) mode as with DESS (cf. Chapter 3) a third independent SSFP mode (namely a higher order SSFP-FID signal: F_1) within a single scan. The calculation of the T_1 and T_2 relaxation times is based on two independent signal ratios and the interacting T_2- and T_1-sensitivity, respectively, is eliminated in an iterative approach. TESS relaxometry is optimized and evaluated in 3D mode by means of simulations, in vitro studies at 1.5 Tesla, and in vivo experiments of the musculoskeletal system at 3 Tesla.

Chapter 5. TESS relaxometry as proposed in Chapter 4 is robust in the presence of B_0 inhomogeneities as it relies on a nonbalanced SSFP sequence. In addition, TESS-based T_2 quantification is intrinsically insensitive to B_1 field variations. This empirical outcome is of special interest at high to ultra-high field strengths where quantitative MR-based tissue characterization benefits from the higher signal-to-noise ratio traded for either improved resolution or reduced scan time, but is impaired by severe static and transmit field heterogeneities. In Chapter 4, 3D TESS imaging is demonstrated to be suitable for fast intrinsically B_1-insensitive T_2 relaxometry of rigid targets. In this chapter, 3D TESS imaging is adapted for rapid high to ultra-high field 2D acquisitions. The achieved short scan times of 2D TESS measurements reduce motion sensitivity and make TESS-based T_2 quantification feasible in the human brain. After validation in vitro and in vivo at 3 Tesla, T_2 maps of the human brain are obtained at 7 Tesla and 9.4 Tesla.

References

[1] P. Tofts. *Quantitative MRI of the Brain.* John Wiley & Sons Ltd, Chichester, 2003.

[2] L. Kelvin. Lecture on *Electrical units of measurement*, May 3, 1883. Published in *Popular Lectures and Addresses* Vol. I. Macmillan and Co., 1889.

[3] R. Damadian. Tumor detection by nuclear magnetic resonance. *Science*, 171 (3976):1151–53, 1971.

[4] H. L. Cheng, N. Stikov, N. R. Ghugre, and G. A. Wright. Practical medical applications of quantitative MR relaxometry. *J Magn Reson Imaging*, 36(4): 805–24, 2012.

[5] F. Bloch. Nuclear induction. *Phys Rev*, 70(7):460–74, 1946.

[6] E. M. Haacke, R. W. Brown, M. R. Thompson, and R. Venkatesan. *Magnetic Resonance Imaging: Physical Principles and Sequence Design.* John Wiley & Sons, Inc, 1999.

[7] M. T. Vlaardingerbroek and J. A. den Boer. *Magnetic Resonance Imaging.* Springer-Verlag, Berlin, 3rd edition, 2003.

[8] L. E. Drain. A direct method of measuring nuclear spin-lattice relaxation times. *Proc Phys Soc A*, 62(5):301–6, 1949.

[9] E. L. Hahn. An accurate nuclear magnetic resonance method for measuring spin-lattice relaxation times. *Phys Rev*, 76(1):145–6, 1949.

[10] P. B. Kingsley, R. J. Ogg, W. E. Reddick, and R. G. Steen. Correction of errors caused by imperfect inversion pulses in MR imaging measurement of T1 relaxation times. *Magn Reson Med*, 16(9):1049–55, 1998.

[11] R. K. Gupta. A modified fast inversion-recovery technique for spin-lattice relaxation measurements. *J Magn Reson*, 38(3):447–52, 1980.

[12] J. K. Barral, E. Gudmundson, N. Stikov, M. Etezadi-Amoli, P. Stoica, and D. G. Nishimura. A robust methodology for in vivo T1 mapping. *Magn Reson Med*, 64 (4):1057–67, 2010.

[13] N. Stikov, M. Boudreau, I. R. Levesque, C. L. Tardif, J. K. Barral, and G. B. Pike. On the accuracy of T1 mapping: searching for common ground. *Magn Reson Med*, 73(2):514–22, 2015.

[14] M. A. Bernstein, K. F. King, and X. J. Zhou. *Handbook of MRI Pulse Sequences.* Elsevier Academic Press, 2004.

[15] G. H. Weiss, R. K. Gupta, J. A. Ferretti, and E. D. Becker. The choice of optimal parameters for measurement of spin-lattice relaxation times. I. Mathematical formulation. *J Magn Reson*, 37(3):369–79, 1980.

[16] E. D. Becker, J. A. Ferretti, R. K. Gupta, and G. H. Weiss. The choice of optimal parameters for measurement of spin-lattice relaxation times. II. Comparison of saturation recovery, inversion recovery, and fast inversion recovery experiments. *J Magn Reson*, 37(3):381–94, 1980.

[17] M. A. Bernstein, D. M. Thomasson, and Perman W. H. Improved detectability in low signal-to-noise ratio magnetic resonance images by means of a phase-corrected real reconstruction. *Med Phys*, 16(5):813–7, 1989.

[18] P. A. Gowland and Leach M. O. A simple method for the restoration of signal polarity in multi-image inversion recovery sequences for measuring T1. *Magn Reson Med*, 18(1):224–31, 1991.

[19] R. D. Dortch, K. Li, D. F. Gochberg, E. B. Welch, A. N. Dula, A. A. Tamhane, J. C. Gore, and S. A. Smith. Quantitative magnetization transfer imaging in human brain at 3 T via selective inversion recovery. *Magn Reson Med*, 66(5): 1346–52, 2011.

[20] R. M. Henkelman. Measurement of signal intensities in the presence of noise in MR images. *Med Phys*, 12(2):232–3, 1985.

[21] O. T. Karlsen, R. Verhagen, and W. M. Bove. Parameter estimation from Rician-distributed data sets using a maximum likelihood estimator: application to T1 and perfusion measurements. *Magn Reson Med*, 41(3):614–23, 1999.

[22] J. Sijbers, A. J. den Dekker, E. Raman, and D. Van Dyck. Parameter estimation from magnitude MR images. *Int J Imaging Syst Technol*, 10(2):109–14, 1999.

[23] P. Mansfield. Multi-planar image formation using NMR spin echoes. *J Phys C: Solid State Physics*, 10(3):L55, 1977.

[24] J. Hennig, A. Nauerth, and H. Friedburg. RARE imaging: a fast imaging method for clinical MR. *Magn Reson Med*, 3(6):823–33, 1986.

[25] E. L. Hahn. Spin echoes. *Phys Rev*, 80(4):580–594, 1950.

[26] D. A. Feinberg, C. M. Mills, J. P. Posin, D. A. Ortendahl, N. M. Hylton, L. E. Crooks, J. C. Watts, L. Kaufman, M. Arakawa, and J. C. Hoenninger. Multiple spin-echo magnetic resonance imaging. *Radiology*, 155(2):437–42, 1985.

[27] H. Y. Carr and E. M. Purcell. Effects of diffusion on free precession in nuclear magnetic resonance experiments. *Phys Rev*, 94(3):630–638, 1954.

[28] S. Meiboom and D. Gill. Modified spin-echo method for measuring nuclear relaxation times. *Rev Sci Instrum*, 29:688–691, 1958.

[29] H. Y. Carr. Steady-state free precession in nuclear magnetic resonance. *Phys Rev*, 112(5):1693–1701, 1958.

[30] R. R. Ernst and W. A. Anderson. Application of Fourier transform spectroscopy to magnetic resonance. *Rev Sci Instrum*, 37(1):93–102, 1966.

[31] R. Freeman and H. D. W. Hill. Phase and intensity anomalies in fourier transform NMR. *J Magn Reson*, 4(3):366–83, 1971.

[32] W. S. Hinshaw. Image formation by nuclear magnetic resonance: the sensitive-point method. *J Appl Phys*, 47(8):3709–21, 1976.

[33] Y. Zur, M. L. Wood, and L. J. Neuringer. Spoiling of transverse magnetization in steady-state sequences. *Magn Reson Med*, 21(2):251–63, 1991.

[34] W. T. Sobol and D. M. Gauntt. On the stationary states in gradient echo imaging. *J Magn Reson Imaging*, 6(2):384–98, 1996.

[35] K. Scheffler. A pictorial description of steady-states in rapid magnetic resonance imaging. *Concepts Magn Reson*, 11(5):291–304, 1999.

[36] D. E. Woessner. Effects of diffusion in nuclear magnetic resonance spin-echo experiments. *J Chem Phys*, 34(6):2057–61, 1961.

[37] R. Kaiser, E. Bartholdi, and R. R. Ernst. Diffusion and field-gradient effects in NMR Fourier spectroscopy. *J. Chem. Phys.*, 60:2966–2979, 1974.

[38] J. Hennig. Echoes–how to generate, recognize, use or avoid them in MR-imaging sequences. Part I + II. *Concepts Magn Reson*, 3(3+4):125–43, 179–92, 1991. ISSN 1099-0534.

[39] M. Weigel. Extended phase graphs: dephasing, RF pulses, and echoes - pure and simple. *J Magn Reson Imaging*, 41(2):266–95, 2015.

[40] R. R. Ernst, G. Bodenhausen, and A. Wokaun. *Principles of Nuclear Magnetic Resonance in One and Two Dimensions*. Clarendon Press, Oxford, 1987.

[41] C. Ganter. Steady state of gradient echo sequences with radiofrequency phase cycling: analytical solution, contrast enhancement with partial spoiling. *Magn Reson Med*, 55(1):98–107, 2006.

[42] Y. Zur, S. Stokar, and P. Bendel. An analysis of fast imaging sequences with steady-state transverse magnetization refocusing. *Magn Reson Med*, 6(2):175–93, 1988.

[43] M. L. Gyngell. The steady-state signals in short-repetition-time sequences. *J Magn Reson*, 81(3):474–83, 1989.

[44] W. Hänicke and H. U. Vogel. An analytical solution for the SSFP signal in MRI. *Magn Reson Med*, 49(4):771–5, 2003.

[45] H. Bruder, H. Fischer, R. Graumann, and M. Deimling. A new steady-state imaging sequence for simultaneous acquisition of two MR images with clearly different contrasts. *Magn Reson Med*, 7(1):35–42, 1988.

[46] T. W. Redpath and R. A. Jones. FADE–A new fast imaging sequence. *Magn Reson Med*, 6(2):224–234, 1988.

[47] C. T. Mizumoto and E. Yoshitome. Multiple echo SSFP sequences. *Magn Reson Med*, 18(1):244–250, 1991.

[48] A. Oppelt, R. Graumann, H. Barfuss, H. Fischer, W. Hartl, and W. Shajor. FISP: a new fast MRI sequence. *Electromedica*, 54:15–18, 1986.

[49] J. L. Duerk, J. S. Lewin, M. Wendt, and C. Petersilge. Remember true FISP? A high SNR, near 1-second imaging method for T2-like contrast in interventional MRI at .2 T. *J Magn Reson Imaging*, 8(1):203–8, 1998.

[50] K. Sekihara. Steady-state magnetizations in rapid NMR imaging using small flip angles and short repetition intervals. *IEEE Trans Med Imaging*, 6(2):157–64, 1987.

[51] K. Scheffler and J. Hennig. Is TrueFISP a gradient-echo or a spin-echo sequence? *Magn Reson Med*, 49(2):395–7, 2003.

[52] Y. Zur, M. L. Wood, and L. J. Neuringer. Motion-insensitive, steady-state free precession imaging. *Magn Reson Med*, 16(3):444–59, 1990.

[53] K. Scheffler and S. Lehnhardt. Principles and applications of balanced ssfp techniques. *Eur Radiol*, 13(11):2409–18, 2003.

[54] O. Bieri and K. Scheffler. Fundamentals of balanced steady state free precession MRI. *J Magn Reson Imaging*, 38(1):2–11, 2013.

[55] T. S. Ibrahim, R. Lee, A. M. Abduljalil, B. A. Baertlein, and P. M. Robitaille. Dielectric resonances and B1 field inhomogeneity in UHFMRI: computational analysis and experimental findings. *Magn Reson Imaging*, 19(2):219–26, 2001.

[56] V. L. Yarnykh. Actual flip-angle imaging in the pulsed steady state: a method for rapid three-dimensional mapping of the transmitted radiofrequency field. *Magn Reson Med*, 57(1):192–200, 2007.

[57] L. I. Sacolick, F. Wiesinger, I. Hancu, and M. W. Vogel. B1 mapping by Bloch-Siegert shift. *Magn Reson Med*, 63(5):1315–22, 2010.

[58] C. Ganter, M. Settles, I. Dregely, F. Santini, K. Scheffler, and O. Bieri. B1+-mapping with the transient phase of unbalanced steady-state free precession. *Magn Reson Med*, 70(6):1515–23, 2013.

[59] G. J.M. Parker, G. J. Barker, and P. S. Tofts. Accurate multislice gradient echo T1 measurement in the presence of non-ideal RF pulse shape and RF field nonuniformity. *Magn Reson Med*, 45(5):838–45, 2001.

[60] E. K. Fram, R. J. Herfkens, G. A. Johnson, G. H. Glover, J. P. Karis, A. Shimakawa, T. G. Perkins, and N. J. Pelc. Rapid calculation of T1 using variable flip angle gradient refocused imaging. *Magn Reson Imaging*, 5(3):201–208, 1987.

[61] S. C. Deoni, B. K. Rutt, and T. M. Peters. Rapid combined T1 and T2 mapping using gradient recalled acquisition in the steady state. *Magn Reson Med*, 49(3): 515–26, 2003.

[62] G. H. Welsch, K. Scheffler, T. C. Mamisch, T. Hughes, S. Millington, M. Deimling, and S. Trattnig. Rapid estimation of cartilage T2 based on double echo at steady state (DESS) with 3 Tesla. *Magn Reson Med*, 62(2):544–9, 2009.

[63] O. Bieri, C. Ganter, and K. Scheffler. On the fluid-tissue contrast behavior of high-resolution steady-state sequences. *Magn Reson Med*, 68(5):1586–92, 2012.

[64] O. Bieri and K. Scheffler. Effect of diffusion in inhomogeneous magnetic fields on balanced steady-state free precession. *NMR Biomed*, 20(1):1–10, 2007.

[65] R. M. Henkelman, G. J. Stanisz, and S. J. Graham. Magnetization transfer in MRI: a review. *NMR Biomed*, 14(2):57–64, 2001.

[66] O. Bieri and K. Scheffler. On the origin of apparent low tissue signals in balanced SSFP. *Magn Reson Med*, 56(5):1067–74, 2006.

[67] M. Gloor, K. Scheffler, and O. Bieri. Quantitative magnetization transfer imaging using balanced SSFP. *Magn Reson Med*, 60(3):691–700, 2008.

Chapter 2

Variable flip angle T_1 mapping in the human brain with reduced T_2 sensitivity using fast RF-spoiled gradient-echo imaging

A modified version of this chapter has been published as:
Heule R, Ganter C, Bieri O. Variable flip angle T_1 mapping in the human brain with reduced T_2 sensitivity using fast radiofrequency-spoiled gradient echo imaging. Magn Reson Med, doi: 10.1002/mrm.25668, 2015.

2.1 Introduction

Measurements of NMR relaxation times offer quantitative determination of tissue parameters and direct comparison of MR images across subjects, time-points and imaging centers. Compared to conventional weighted imaging, quantitative relaxometry provides improved tissue discrimination and classification, thus having the potential to fundamentally advance the diagnostic power of MRI. The diagnostic value of mapping the longitudinal relaxation time (T_1) has been investigated in several studies, particularly in the field of the clinical neurosciences, e.g. in the context of multiple sclerosis [1, 2] and other neurodegenerative disorders such as Parkinson's disease [3, 4].

Many T_1 mapping methods have been developed [5], however, they deliver substantially varying quantification results for the same tissues and at equal field strength. Three commonly used techniques are inversion recovery (IR) [6, 7] which is considered to be the gold standard, Look-Locker (LL) [8, 9], and variable flip angle (VFA) [10, 11]. For these three methods, brain white matter T_1 values measured at 3 Tesla (T) were reported to range from 690 ms to 1100 ms. Moreover, even with IR protocols, literature values vary by more than 50 % as pointed out in a recent comparative study on the accuracy of existing T_1 relaxometry methods [12]. The authors of this study found that LL consistently underestimated the IR T_1 values in vivo while VFA consistently overestimated them and they concluded that incomplete spoiling and inaccurate mapping of the inhomogeneities in the transmit field (B_1) may account for the observed differences.

T_1 estimation based on the conventional two-dimensional (2D) IR or LL sequences is not suited for whole-brain imaging in the clinical setting due to prohibitively long measurement times. In contrast, the VFA method provides three-dimensional (3D) MR data sets and allows for volumetric T_1 mapping in clinically feasible times [13]. This approach requires the acquisition of at least two spoiled gradient-echo (SPGR) images at equal pulse sequence repetition time (TR) and echo time (TE) but varying flip angle (α). In the case of ideal spoiling, i.e. complete elimination of any residual coherent transverse magnetization, the obtained steady state depends only on T_1 without confounding influence of transverse relaxation (T_2). From the set of acquired MR images with different flip angles, T_1 can then be quantified through a linearization of the steady-state signal equation. It has been demonstrated that for the narrow range of T_1 values present in human brain tissues (with the exception of subcutaneous fat), a set of only two flip angles yields optimal T_1 precision [11, 14].

The simplest way of effectively destroying the residual transverse magnetization prior to each radiofrequency (RF) excitation pulse is to select a long TR with $T_2/\mathrm{TR} \to 0$. However, as the main advantage of 3D SPGR sequences is acquisition speed, a more appropriate spoiling method has to be used. Nowadays, sufficiently strong spoiler gradients are generally applied in combination with a predetermined RF phase cycling scheme. It was observed that, with time-varying spoiler gradient moments or randomly distributed RF phases, the achieved spoiling will be spatially nonuniform [15, 16] or associated with statistical fluctuations among TR [17], respectively. In contrast, a homogeneous steady state can be generated by linearly incrementing the differences between the phases of subsequent pulses, in the following referred to as RF spoiling [15, 17]. It must be noted that the obtained steady state depends sensitively

on the choice of the RF phase difference increment (φ) and may deviate considerably from the case of ideal spoiling due to the arising T_2 dependency [18]. As a consequence, complete spoiling can generally not be achieved with the common SPGR sequences and a systematic error is introduced into T_1 quantification based on the VFA technique.

Different values for the RF phase difference increment have been proposed, e.g. 117° [17] and 150° [19] due to the good agreement with the ideally spoiled case, 84° [20] and 96.5° [21] due to the better convergence properties of the approach to the steady state, or 50° [22] due to the higher stability. Recent attempts to improve the accuracy of VFA T_1 mapping are mostly based on optimizing the spoiling efficiency of the underlying sequence in combination with suitable B_1 mapping techniques to correct the errors arising from inhomogeneous flip angle distributions [19, 23–25]. The results obtained in Ref. [24] demonstrate that correct interpretation of spoiling phenomena in VFA methods requires accurate consideration of the diffusion effect. The influence of the chosen RF phase difference increment on the stability and accuracy of T_1 quantification has been evaluated in Ref. [22]. It was shown that a choice of 118.2° or 121.8° yields correct and robust T_1 values in phantom measurements but instable results in the human brain, possibly because of physiological effects (e.g. CSF pulsations or perfusion) and subject motion, while a choice of 50° considerably increased the stability. It thus seems advisable to select the phase difference increment with regard to stability and use suitable postprocessing methods to compute accurate T_1 values.

In this work, a new postprocessing approach is presented for VFA-based T_1 quantification of human brain tissues which, rather than assuming ideal spoiling, makes use of a recently derived analytical solution for the steady state of gradient-echo sequences with RF spoiling [18]. Based on this analytical formula and a global T_2 estimate, T_1 can be extracted from the ratio of the two MR signals acquired at different flip angles. By this means, the sensitivity of VFA T_1 mapping to T_2 can considerably be reduced. The presented postprocessing method is combined with a novel B_1 mapping technique (in the literature referred to as B1-TRAP) [26] to account for flip angle miscalibrations.

2.2 Methods

2.2.1 Variable flip angle (VFA) T_1 quantification

The steady-state signal from an ideally spoiled gradient-echo acquisition is given by

$$S_{\text{ideal}} = K \cdot \frac{1 - E_1}{1 - E_1 \cdot \cos\alpha} \cdot \sin\alpha \tag{2.1}$$

with $E_1 := \exp(-\text{TR}/T_1)$ and a proportionality factor K that incorporates the proton density, the coil sensitivity, and T_2^* relaxation. From at least two measurements at different flip angles, T_1 and K can be determined by casting Eq. (2.1) into a linear form and using linear least squares regression [10, 11]. This conventional approach commonly used for brain tissue T_1 quantification is biased by incomplete spoiling.

More general, an exact analytical solution has been derived for the steady-state

signal of RF-spoiled gradient-echo sequences [18]

$$S_{\mathrm{RFspoil}} = K \cdot \left| -i \frac{1 - E_1}{D} \cdot \sin\alpha \cdot (1 - \Lambda^*) \right| \tag{2.2}$$

with

$$D := 1 - E_1 \cos\alpha - \frac{1}{2}(1 - \cos\alpha) \cdot (1 + E_1)(\Lambda + \Lambda^*) + (E_1 - \cos\alpha)|\Lambda|^2.$$

The parameter Λ is defined by a continued fraction expansion (detailed formulas can be found in Ref. [18]) and depends on TR, α, φ, T_1, and T_2. Note that both signal models (Eq. (2.1) and Eq. (2.2)) neglect the effect of diffusion.

Here, we propose T_1 quantification based on Eq. (2.2) as follows: SPGR imaging with RF spoiling is performed at two different flip angles (α_1 and α_2). From the acquired signal amplitudes S_{α_1} and S_{α_2}, the signal ratio $s := S_{\alpha_1}/S_{\alpha_2}$ is calculated. The equation to solve is given by

$$s = s_{\mathrm{TR},\alpha_1,\alpha_2,\varphi}(T_1, T_2) \tag{2.3}$$

with

$$s_{\mathrm{TR},\alpha_1,\alpha_2,\varphi}(T_1, T_2) := \frac{S_{\mathrm{RFspoil},\alpha_1}}{S_{\mathrm{RFspoil},\alpha_2}}.$$

The left-hand side of Eq. (2.3) represents the measured signal ratio whereas the right-hand side derives from the given protocol specific extrinsic parameters (TR, α_1, α_2, and φ) and from the variable intrinsic relaxation times (T_1 and T_2) according to Eq. (2.2). The proportionality factor K cancels out in the signal ratio. By using a simple global T_2 estimator ($T_{2,\mathrm{est}}$) and a search interval for T_1 with a (dummy) upper guess of $T_{1,u} = 10$ s, Eq. (2.3) can be solved by numerical minimization:

$$T_1 = \arg\min\{T_1 \in [0, T_{1,u}] : |s - s_{\mathrm{TR},\alpha_1,\alpha_2,\varphi,T_{2,\mathrm{est}}}(T_1)|\}. \tag{2.4}$$

A golden section search [27] is used as fast minimization method and it is verified that the function to be minimized (cf. Eq. (2.4)) is continuous over $[0, T_{1,u}]$ and contains only one minimum inside this interval.

2.2.2 Simulation and sequence parameters

All numerical simulations, data analysis and visualization were done using Matlab R2012b (The MathWorks, Inc., Natick, MA). The default measurement protocol of 3D SPGR imaging used in this work for T_1 estimation includes the parameters TR = 7.6 ms, $\alpha_1 = 4°$, $\alpha_2 = 18°$, and $\varphi = 50°$ (default RF phase difference increment in the Siemens product implementation of the SPGR sequence). Similar protocols are commonly employed for VFA-based T_1 mapping in the human brain [22, 28]. In Ref. [28], flip angles of 4° and 18° were reported to be optimal at a similar TR for the mean white and gray matter T_1. If not otherwise stated, the numerical simulations were performed with TR, α_1, α_2, and φ as in the investigated default acquisition protocol including a gradient dephasing moment ($G\tau$) of 23.5 (mT/m)ms (minimal

moment required to achieve a 2π dephasing per voxel at an in-plane resolution of 1 mm). For human brain tissues at 3 T, a T_1 of 1000 ms, a T_2 of 70 ms, and a diffusion coefficient D of 1.0 $\mu m^2/ms$ (upper limit of reported values in white and gray matter) were assumed [29–32]. As global T_2 estimate, a value of 70 ms was used consistently in all simulations as well as for the in vivo T_1 quantification of human brain tissues.

SPGR signal ratios (s) were simulated based on the extended phase graph (EPG) formalism [33] to include the effect of diffusion (free and isotropic assumed) using a sequence of 1000 RF pulses. The deviation of the signal ratios calculated based on the models given in Eqs. (2.1) and (2.2) from the EPG simulation was quantified as

$$|\Delta s| = \mathrm{abs}[(s - s_{\mathrm{model}})/s] \tag{2.5}$$

with model = {ideal, RFspoil}, and the corresponding error in the T_1 calculation was obtained from

$$|\Delta T_1| = \mathrm{abs}[(T_1 - T_{1,\mathrm{calc}})/T_1] \tag{2.6}$$

(T_1: true T_1 relaxation time, $T_{1,\mathrm{calc}}$: calculated T_1 relaxation time). The accuracy of the proposed method was compared to the standard VFA T_1 calculation.

2.2.3 Correction of transmit field inhomogeneities

In the presence of B_1 field inhomogeneities, the actual flip angle differs from the nominal one: $\alpha_{\mathrm{act}} = c_{B_1} \cdot \alpha_{\mathrm{nom}}$ where c_{B_1} reflects the local sensitivity of the transmit coil and the varying dielectric properties of different tissues. This introduces an error into all VFA-based T_1 relaxometry methods as they incorporate the flip angle directly into the T_1 calculation (cf. Eqs. (2.1) to (2.4)). In this work, an additional measurement with a recently presented B_1 mapping sequence (called B1-TRAP) [26] was performed in order to yield α_{act} pixelwise. B1-TRAP measures the actual flip angle from the angular frequency of the distinct signal oscillations in the transient phase of unbalanced steady-state free precession (SSFP) sequences. 2D multi-slice B1-TRAP acquisitions were demonstrated to deliver robust and highly accurate B_1 maps of the human head in short time and with minimal sensitivity to off-resonance [26].

2.2.4 Correction factors for $\varphi = 50°$

For a T_1 mapping experiment performed with TR = 7.6 ms, $\alpha_1 = 4°$, $\alpha = 18°$, and $\varphi = 50°$ (default protocol in this work), an alternative calculation of T_1 based on correction factors was presented in Ref. [22] as follows:

$$T_1 = A(c_{B_1}) + B(c_{B_1}) \cdot T_{1,\mathrm{app}} \tag{2.7}$$

where $T_{1,\mathrm{app}}$ is the apparent T_1 calculated based on the assumption of ideal spoiling (Eq. (2.1)). The dependence of the parameters A and B on c_{B_1} was approximated by parabolic functions:

$$\begin{aligned} A &= 275\,\mathrm{ms} \cdot {c_{B_1}}^2 - 359\,\mathrm{ms} \cdot c_{B_1} + 142\,\mathrm{ms}, \\ B &= -0.33 \cdot {c_{B_1}}^2 + 0.25 \cdot c_{B_1} + 0.92. \end{aligned}$$

Computation of correction factors in this way is dependent on the acquisition parameters and the influence of T_2 variations is entirely neglected. Here, this approach was used as an additional reference for T_1 relaxometry based on acquisitions with the default protocol.

2.2.5 In vivo measurements

All MRI scans were performed on a 3 T system (Magnetom Prisma, Siemens Medical Solution, Erlangen, Germany) using the standard 20-channel receive head coil of the manufacturer and approved by the local ethics committee. All experiments were conducted on the same healthy volunteer in order to ensure direct comparability of the calculated T_1 values. Axial 3D SPGR scans of the human head were accomplished according to similar protocols described in the literature [22, 28]:

- 3D SPGR (default)
    - o isotropic resolution: 1.33 mm × 1.33 mm × 1.33 mm
    - o 128 partitions
    - o slab-selective excitation
    - o 25 % oversampling in partition encoding direction
    - o receive bandwidth: 228 Hz/pixel
    - o TR = 7.6 ms / TE = 3.43 ms
    - o $G\tau$ = 38.2 (mT/m)ms
    - o acquisition time per measurement: 2 min 55 s
    - o nominal flip angles: 4° (measurement 1) and 18° (measurement 2)

The 3D SPGR measurements were performed for a range of RF phase difference increments (15°, 27°, 50°, 57°, 60°, 63°, 69°, 72°, 75°, 86°, 90°, 94°, 114°, 120°, 126°, 141°, 144°, 147°, 173°) to evaluate the influence of diffusion (50° was considered to be the default value).

Additionally, 3D SPGR imaging was performed with shortened and lengthened TR. The corresponding optimal flip angles for T_1 quantification were derived according to Ref. [11], Eq. (11) assuming a true T_1 of 1000 ms. The parameters (where they differed from the default protocol using a phase difference increment of 50°) were as follows:

- 3D SPGR (shortened TR)
    - o non-selective excitation (hard pulse)
    - o 100 % oversampling in partition encoding direction
    - o receive bandwidth: 704 Hz/pixel
    - o TR = 3.8 ms / TE = 1.63 ms
    - o acquisition time per measurement: 2 min 20 s
    - o nominal flip angles: 2° (measurement 1) and 12° (measurement 2)

- 3D SPGR (lengthened TR)
  - receive bandwidth: 122 Hz/pixel
  - TR = 11.4 ms / TE = 5.32 ms
  - parallel imaging technique: GRAPPA[a] (acceleration factor: 2, reference lines: 24)
  - acquisition time per measurement: 2 min 31 s
  - nominal flip angles: 4° (measurement 1) and 21° (measurement 2)

[a]GRAPPA: generalized autocalibrating partially parallel acquisition

Correction of transmit field inhomogeneities was obtained from an additional B_1 mapping scan using the following protocol:

- 2D multi-slice B1-TRAP [26]
  - resolution: 4 mm × 4 mm × 6 mm
  - 12 slices, slice gap: 6 mm
  - slice-selective excitation
    - duration: 1800 μs
    - bandwidth: 1.78 kHz
  - receive bandwidth: 1220 Hz/pixel
  - TR = 4.19 ms / TE = 2.46 ms
  - acquisition time: 56 s
  - nominal flip angle: 60°

The images from 3D SPGR and 2D multi-slice B1-TRAP measurements were registered (including segmentation of the skull in the case of 3D SPGR) using the software packages FSL [34] and AFNI [35]. After image registration, T_1 maps were derived based on Eqs. (2.2)-(2.4) and for comparison based on the standard VFA method (cf. Eq. (2.1)) by using the actual flip angle delivered by B1-TRAP to eliminate the B_1 bias in both methods. For the default protocol, T_1 values were also calculated based on correction factors (cf. Eq. (2.7)).

For reference, T_1 was quantified with the current gold-standard method based on an IR turbo spin-echo (TSE) sequence. In order to mitigate the influence of magnetization transfer effects and imperfection in the inversion pulse profile, only a single slice was imaged with non-selective inversion. The IR slice was picked to match one of the central slices reconstructed from 3D SPGR imaging. The following setting was used:

- single-slice IR-TSE
  - resolution: 1 mm × 1 mm × 2 mm
  - non-selective inversion

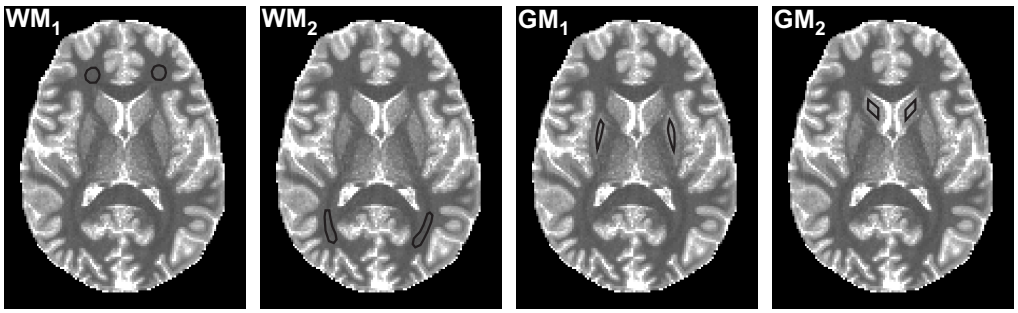

Figure 2.1: Mean T_1 values were assessed for four regions of interest in white matter (WM) and gray matter (GM) as drawn here in the VFA T_1 map obtained based on Eqs. (2.2)-(2.4) for a healthy volunteer: frontal white matter (WM_1), occipital white matter (WM_2), putamen (GM_1), and caudate nucleus head (GM_2).

- reconstruction: real part
- receive bandwidth: 130 Hz/pixel
- TR = 10 s / TE = 15 ms
- turbo factor 7
- acquisition time per measurement: 2 min 32 s
- inversion times: 200 ms, 400 ms, 800 ms, 1600 ms, and 3200 ms (measurements 1 to 5)

From the five scans at different inversion times (TI), T_1 values were calculated using a nonlinear least squares fit of the mono-exponential three parameter model: $p_1(1 - p_2 \cdot \exp(TI/p_3))$, p_1: proton density / coil sensitivity, p_2: parameter to account for imperfect inversion (ideally 2), p_3: T_1 estimate. The final T_1 map was segmented (skull stripped) using an FSL routine.

Brain T_1 histograms of bin size 15 ms were calculated for the T_1 maps obtained from VFA and IR in order to assess the WM T_1 peak. In addition, T_1 was analyzed for selected regions of interest (ROIs) in white matter (WM) and gray matter (GM). Mean ± SD (standard deviation in the regions) T_1 values across both hemispheres were computed for frontal white matter (WM_1), occipital white matter (WM_2), and in gray matter for the putamen (GM_1) and the caudate nucleus head (GM_2) (cf. Fig. 2.1).

2.3 Results

2.3.1 Simulations

The signal models given in Eqs. (2.1) and (2.2) are biased by incomplete spoiling (Eq. (2.1)) and diffusion (Eq. (2.2)). This bias ($|\Delta s|$, see Eq. (2.5)) is analyzed in Figures 2.2 a and 2.2 b as a function of φ for a T_1 value of 1000 ms and a T_2 value of 70 ms. It is observed that the two models exhibit peaks in $|\Delta s|$ at the same locations over the whole range of φ values ($0° - 180°$, Fig. 2.2 a). The RF-spoiled signal model (blue curve) proves to be highly insensitive to diffusion for φ values in the plateau areas

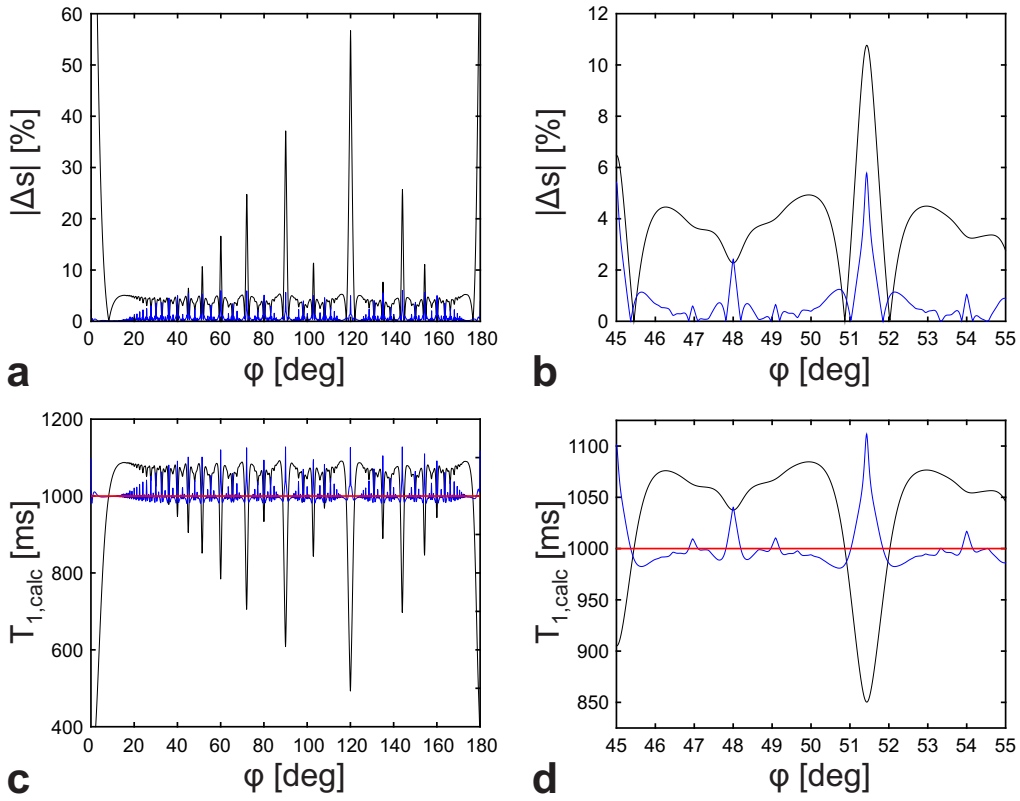

Figure 2.2: In (a) and (b), $|\Delta s|$ (see Eq. (2.5)) is simulated versus the RF phase difference increment φ for a whole range of φ values ($0° - 180°$, a) and an expanded region centered at $50°$ ($45° - 55°$, b). The ideally spoiled signal model (Eq. (2.1), black curve) is compared to the RF-spoiled signal model (Eq. (2.2), blue curve). The corresponding calculated T_1 values ($T_{1,\mathrm{calc}}$) are shown in (c) and (d), respectively. A global T_2 guess of 70 ms was used for the proposed T_1 quantification method (blue curves). The SPGR signal amplitudes were generated for a true T_1 of 1000 ms (red horizontal line in c and d), a true T_2 of 70 ms, and a diffusion coefficient D of 1.0 $\mu\mathrm{m}^2/\mathrm{ms}$.

(diffusion-related simulation parameters: D = 1.0 $\mu\mathrm{m}^2/\mathrm{ms}$, $G\tau = 23.5$ (mT/m)ms) as apparent in the plot of an expanded region centered at $50°$ (Fig. 2.2 b). In contrast, the plateaus of the ideally spoiled signal model (black curve) are clearly biased by incomplete spoiling.

The corresponding calculated T_1 values are shown in Figures 2.2 c (whole range of φ values) and 2.2 d (expanded region centered at $50°$), respectively. For the new method, it is assumed that a good global T_2 guess is available (as feasible in the human brain). If the true T_2 value coincides with the estimate, the calculated T_1 is close to the true value (Figs. 2.2 c and 2.2 d, blue curves). The standard VFA method, on the other hand, substantially overestimates the true T_1 value of up to 10 % in the plateau regions (Figs. 2.2 c and 2.2 d, black curves).

The rapid oscillations visible in Figure 2.2 indicate that a proper choice of φ

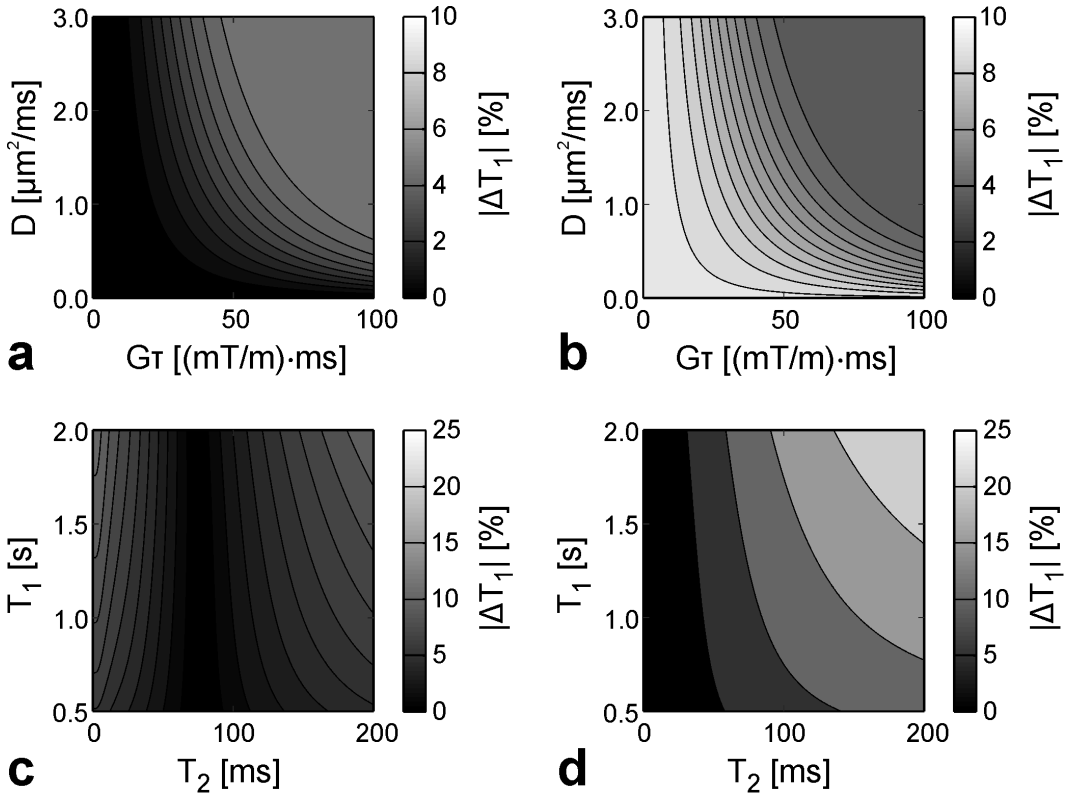

Figure 2.3: Effect of diffusion and relaxation times on the accuracy of VFA T_1 quantification. (a) and (b): Error in the T_1 calculation as a function of the diffusion coefficient D and the gradient dephasing moment $G\tau$ (assuming a true T_1 of 1000 ms and a true T_2 of 70 ms). (c) and (d): Error in the T_1 calculation as a function of the relaxation times T_1 and T_2 (assuming a D value of 1.0 μm^2/ms and a $G\tau$ value of 23.5 (mT/m)ms). The proposed method using a global T_2 guess of 70 ms (a and c) is compared to standard VFA T_1 determination assuming complete spoiling (b and d).

is crucial for the accuracy and precision of VFA T_1 calculation. In Figure 2.3, the influence of the diffusion parameters (D, $G\tau$) and the relaxation times (T_1, T_2) on the accuracy of VFA T_1 mapping is analyzed for a phase difference increment of 50°. This value lies on a plateau area (cf. Figs. 2.2 b and 2.2 d) and was reported in Ref. [22] to provide stable T_1 measurements in the human brain.

Simulations of $|\Delta T_1|$ (see Eq. (2.6)) as a function of D and $G\tau$ reveal that, generally, VFA T_1 quantification based on Eqs. (2.2)-(2.4) performs better the smaller the influence of diffusion (i.e. the smaller D and $G\tau$, Fig. 2.3 a) while conventional VFA T_1 mapping performs better the stronger the diffusion effect (Fig. 2.3 b). For typical spoiler gradient moments used in SPGR imaging at short TR and regular resolution (~ 20 – 40 (mT/m)ms [24]), the new method yields a considerable improvement in terms of accuracy as compared to standard VFA. In the range of D = 0.6 – 0.9 μm^2/ms (mean apparent diffusion coefficient values reported for white and gray mat-

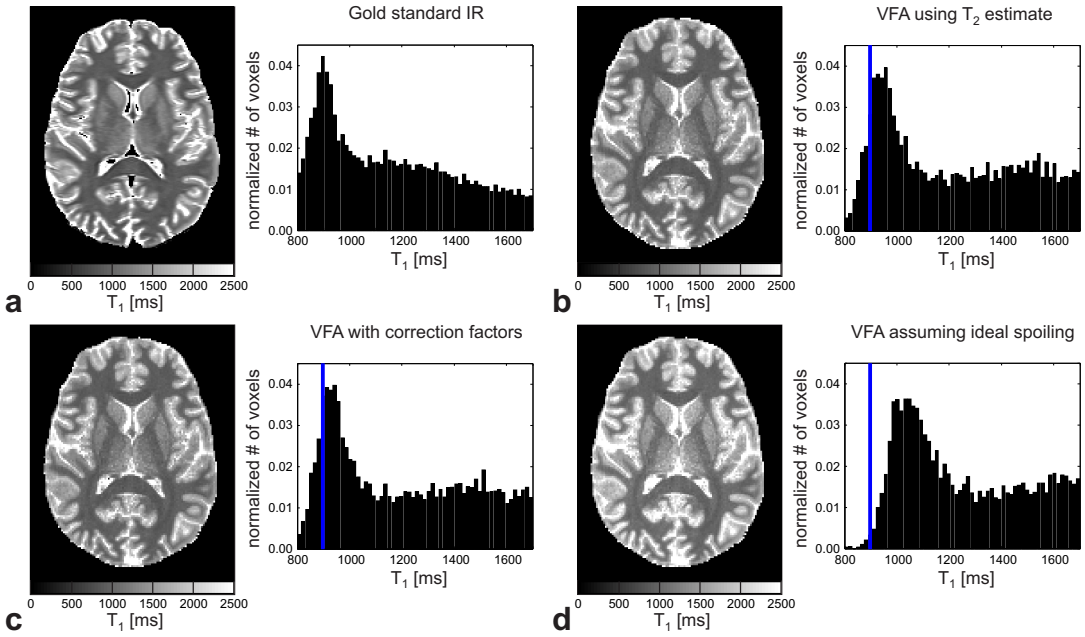

Figure 2.4: Representative T_1 maps and corresponding T_1 histograms obtained at 3 T for a selected slice in the human brain of a healthy volunteer using single-slice IR measurements for reference (a) and 3D VFA SPGR imaging (b-d). VFA T_1 calculation was performed using a global T_2 estimate of 70 ms according to Eqs. (2.2)-(2.4) (b), with correction factors according to Eq. (2.7) (c), and assuming ideal spoiling using Eq. (2.1) (d). The blue vertical line in (b-d) depicts the location of the white matter T_1 peak from the IR reference measurement displayed in (a).

ter structures in Ref. [31]) and 20 – 40 (mT/m)ms, the error in T_1 calculated based on Eqs. (2.2)-(2.4) is overall below 1.7 % (cf. Fig. 2.3 a) as compared to an error of 7.3 – 8.8 % in conventional T_1 estimation (cf. Fig. 2.3 b).

In Figures 2.3 c and 2.3 d, the residual sensitivity of the VFA T_1 calculation to T_2 is analyzed as a function of T_1. For the expected range of relaxation times observed in human brain tissues (T_1 = 800 – 1600 ms, T_2 = 45 – 110 ms [29, 30, 32]), VFA T_1 estimation using Eqs. (2.2)-(2.4) in combination with a global T_2 guess of 70 ms provides improved accuracy in comparison to standard VFA. In particular, $|\Delta T_1| \leq$ 4 % in the range of relaxation times relevant for this work (cf. Fig. 2.3 c) while the conventional method is prone to a substantial error of up to 15 % in this range (cf. Fig. 2.3 d).

2.3.2 In vivo T_1 mapping

In Figure 2.4, the final brain T_1 maps of a healthy volunteer with the corresponding T_1 histograms are shown as acquired using the IR-TSE and the default SPGR protocols. The WM T_1 histogram peak of the reference IR measurement occurs at 890 ms to 905 ms (cf. Fig. 2.4 a). Conventional VFA T_1 mapping substantially overestimates the IR T_1 values (WM T_1 peak located at around 1010 ms to 1040 ms, cf. Fig. 2.4 d).

Table 2.1: Comparison of mean ± SD (standard deviation in the regions) IR-SE and VFA (default protocol) T_1 values corresponding to the T_1 maps shown in Figure 2.4 obtained for a healthy volunteer at 3 T and the selected regions of interest defined in Figure 2.1.

Brain tissue	IR-SE T_1 [ms]	VFA T_1 [ms]		
		Using T_2 estimate	With correction factors	Assuming ideal spoiling
WM				
Frontal WM (WM_1)	913 ± 23	923 ± 34	910 ± 32	1002 ± 39
Occipital WM (WM_2)	885 ± 47	902 ± 43	889 ± 41	1005 ± 54
GM				
Putamen (GM_1)	1275 ± 50	1309 ± 91	1277 ± 89	1502 ± 108
Caudate nucleus head (GM_2)	1424 ± 50	1432 ± 94	1402 ± 93	1632 ± 115

In contrast, T_1 calculation according to Eqs. (2.2)-(2.4) using a global T_2 estimate of 70 ms demonstrates clearly improved agreement with IR as seen from the location of the WM T_1 peak in Figure 2.4 b which occurs in the close vicinity of the IR reference value (blue vertical line). Excellent agreement is observed between the WM T_1 peak locations using a T_2 estimate (Fig. 2.4 b) and correction factors according to Eq. (2.7) (as computed for the specific parameters of the default SPGR protocol, cf. Fig. 2.4 c) demonstrating the validity of the proposed T_1 calculation approach.

Mean T_1 values in Figure 2.4 calculated for selected ROIs in white and gray matter (cf. Fig. 2.1 and Table 2.1) using a global T_2 guess (cf. Eqs. (2.2)-(2.4)) deviate overall less than 4 % from the IR reference T_1 values and agree well with the mean T_1 yielded from Eq. (2.7) given for comparison. In contrast, the assumption of ideal spoiling (cf. Eq. (2.1)) results in substantial deviations from the IR reference measurement of up to 18 %.

In Figure 2.5, the results from a series of VFA T_1 measurements with different φ values are displayed for the selected ROIs in white and gray matter as indicated in Figure 2.1. For φ values on plateau areas, good agreement is observed between mean T_1 values derived from VFA T_1 mapping based on Eqs. (2.2)-(2.4) and a preceding IR reference T_1 measurement of the same volunteer (cf. Fig. 2.4, Table 2.1). Conventional VFA shows a substantial overestimation of T_1 on the plateaus for all ROIs of about 10 – 15 %.

The impact of the protocol setting was further evaluated by varying the repetition time (and correspondingly the optimal flip angles). The results for measurements at TR = 3.8 ms, TR = 7.6 ms (default), and TR = 11.4 ms are summarized in Table 2.2 for the ROIs displayed in Figure 2.1. A slight increase in the mean T_1 values derived by using a T_2 estimate is observed for shorter TR, particularly visible in the mean T_1 of frontal white matter. Nevertheless, the new method performs in all cases clearly better than the conventional approach with regard to accuracy (cf. the T_1 reference values in Table 2.1 obtained from IR scans of the same volunteer at equal slice position) and

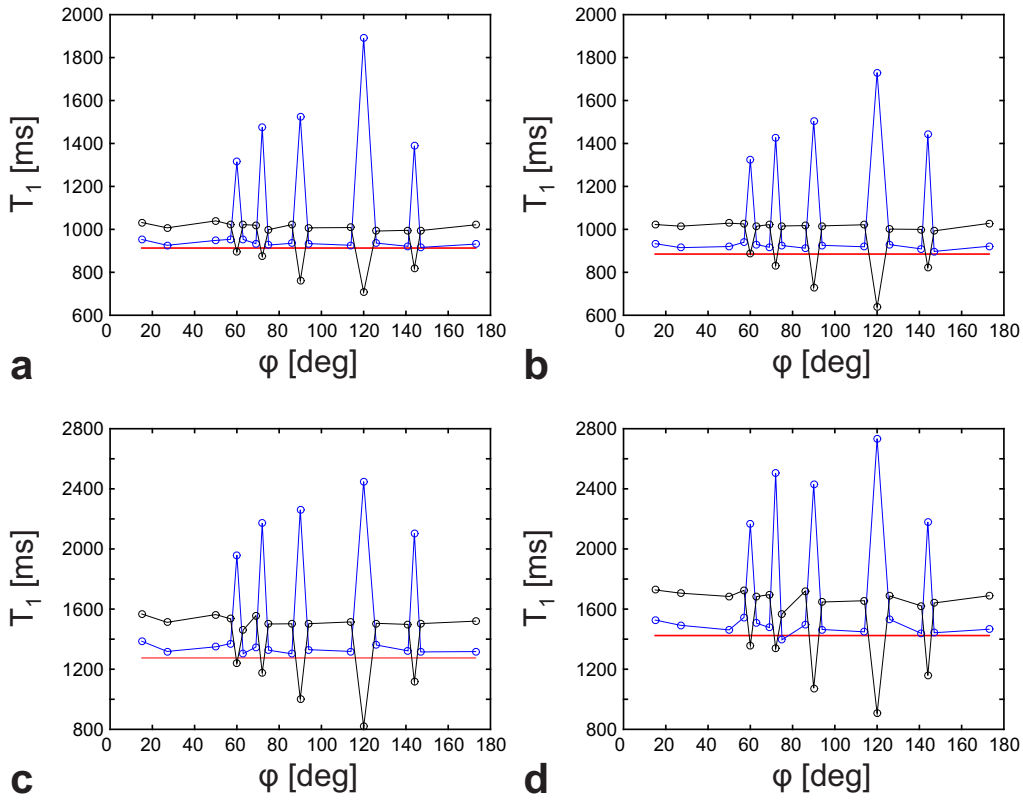

Figure 2.5: Mean T_1 values derived from VFA imaging in the human brain at 3 T for regions of interest in frontal white matter (a), occipital white matter (b), putamen (c), and caudate nucleus head (d) of a healthy volunteer (for definition of the regions of interest, see Fig. 2.1). The measurements were repeated for a range of RF phase difference increments φ. The blue circles refer to T_1 estimation based on Eqs. (2.2)-(2.4), the black circles to the standard VFA T_1 mapping method. For better visibility of the peaks, the T_1 measurements (circles) are connected by straight lines. The red horizontal line indicates the level of the reference IR T_1 value obtained for the same volunteer in a preceding scan (cf. Fig. 2.4, Table 2.1).

comparably with regard to precision. In addition, mean T_1 values obtained at TR = 7.6 ms agree well with the ones given in Table 2.1 reflecting good reproducibility.

2.4 Discussion

The conventional approach for T_1 estimation in the human brain based on VFA SPGR imaging relies on the crucial assumption of ideal spoiling [11]. However, this assumption is generally wrong. In fact, there exists no universal RF phase increment which assures ideal spoiling for a complete range of T_1 and T_2 values of interest and sequence parameters. Furthermore, the default phase increments implemented by the major MRI vendors are different and may not be chosen with regard to maximizing the spoiling efficiency but rather with regard to achieving maximal stability in vivo as in

Table 2.2: Mean ± SD (standard deviation in the regions) VFA T_1 values obtained from the measurement of a healthy volunteer at 3 T with varied repetition times for the selected regions of interest defined in Figure 2.1.

Brain tissue	VFA T_1 [ms]					
	TR = 3.8 ms		TR = 7.6 ms		TR = 11.4 ms	
	Using T_2 estimate	Assuming ideal spoiling	Using T_2 estimate	Assuming ideal spoiling	Using T_2 estimate	Assuming ideal spoiling
WM						
Frontal WM (WM_1)	963 ± 41	1004 ± 44	931 ± 28	1025 ± 34	916 ± 28	984 ± 32
Occipital WM (WM_2)	946 ± 49	997 ± 55	915 ± 40	1024 ± 43	911 ± 35	992 ± 42
GM						
Putamen (GM_1)	1305 ± 65	1397 ± 70	1297 ± 72	1511 ± 87	1267 ± 55	1413 ± 63
Caudate nucleus head (GM_2)	1462 ± 114	1559 ± 125	1438 ± 101	1667 ± 126	1422 ± 73	1582 ± 86

the case of the Siemens SPGR sequence setting (default value of 50°). Neglecting the issue of incomplete spoiling (i.e. using the ideally spoiled steady-state signal equation given in Eq. (2.1)) leads to a considerable systematic error in VFA T_1 relaxometry. As demonstrated in this work, a pronounced reduction in this T_2-related bias can be achieved by making use of the analytical expression for the RF-spoiled steady-state signal (cf. Eqs. (2.2)-(2.4)) in combination with a global T_2 guess (cf. Table 2.1).

In this study, a small systematic T_1 overestimation of the IR reference values (~ 1 – 3.5 %) is observed for the suggested VFA T_1 quantification method (cf. Figs. 2.4 a and 2.4 b, Table 2.1). First, there may be partial volume effects explaining the qualitatively different histogram shapes of the IR and VFA methods (cf. Fig. 2.4). Note that for the IR scans a larger slice thickness (2 mm) was used compared to the SPGR scans (1.33 mm). Second, T_1 overestimation in VFA may be caused by a residual inaccuracy in the used B_1 mapping method or it may originate from a noise-induced bias. In Ref. [36], noise threshold was identified as a source of systematic error in VFA T_1 calculation. However, this effect is generally subtle at suitable signal-to-noise ratio levels. Third, also the IR reference scans may be prone to systematic errors due to imperfections in the inversion pulse or magnetization transfer (MT) effects. It is known that MT induces bi-exponential recovery of longitudinal magnetization in white and gray matter in the human brain [37].

In general, the effect of diffusion adversely affects the accuracy of VFA T_1 mapping based on the RF-spoiled signal model. However, the spoiler gradient areas used in common VFA imaging applications at clinically relevant resolutions (typically ~ 20 – 40 (mT/m)ms [24]) introduce a minor diffusion effect. For this weak spoiling regime, VFA T_1 quantification of human brain tissues based on Eqs. (2.2)-(2.4) is only negligibly impaired as demonstrated in this work, provided the chosen RF phase difference increment lies on a plateau region (cf. Figs. 2.2 and 2.5). In standard VFA T_1 relax-

ometry, spoiler gradient moments are often increased in order to smooth the spoiling profiles by benefiting from the diffusion effect. However, an increase in the gradient area comes generally along with an increase in TR due to hardware limitations and may lead to prohibitive measurement time requirements. The suggested method offers highly accurate T_1 quantification in the human brain in acceptable scan times for the clinical routine.

Apart from the choice of φ, the proposed postprocessing method is largely independent of the sequence parameters as has been verified by varying TR and correspondingly the optimal flip angles (cf. Table 2.2). Only small variations were observed; in particular a slight increase in the mean T_1 values derived using Eqs. (2.2)-(2.4) for shorter TR which may be attributed to higher diffusion sensitivity.

Frequently, VFA SPGR imaging is combined with VFA balanced SSFP (bSSFP) imaging [11, 13, 38, 39]. The T_1 information extracted from the two acquired SPGR images can be used to quantify T_2 from two bSSFP images acquired at constant TR and different flip angles. This procedure offers rapid high-resolution whole-brain T_1 and T_2 mapping in clinically feasible measurement times [13]. However, the achieved T_1 and T_2 maps are confoundingly biased by T_2 and T_1 respectively, if T_1 is determined in the conventional way. Quantifying T_1 as suggested in this work and combining the obtained T_1 with VFA bSSFP imaging to determine T_2 allows to eliminate the T_2-related bias in T_1 (and correspondingly the T_1-related bias in T_2) in an iterative calculation. Note that such an iterative T_1 and T_2 quantification is only feasible if the bias from diffusion is small, i.e. if conventional spoiling gradient moments are applied. As a result, the proposed postprocessing method has the potential to deliver accurate T_1 values in other targets of the human body with higher T_2 variations than in the brain in combination with VFA bSSFP T_2 quantification.

2.5 Conclusions

Conventional VFA T_1 relaxometry based on RF-spoiled SPGR imaging suffers from incomplete spoiling. By making use of a global T_2 guess and an analytical solution for the RF-spoiled steady-state signal, the sensitivity of the T_1 calculation to T_2 can substantially be reduced as demonstrated within the scope of this work for human brain imaging at 3 T. In combination with appropriate B_1 mapping techniques and additional T_2 determination as frequently used in the clinical setting, the suggested method offers highly accurate and robust whole-brain T_1 quantification at high-resolution in clinically feasible times.

References

[1] H. Vrenken, J. J. Geurts, D. L. Knol, L. N. van Dijk, V. Dattola, B. Jasperse, R. A. van Schijndel, C. H. Polman, J. A. Castelijns, F. Barkhof, and P. J. Pouwels. Whole-brain T1 mapping in multiple sclerosis: global changes of normal-appearing gray and white matter. *Radiology*, 240(3):811–20, 2006.

[2] F. Manfredonia, O. Ciccarelli, Z. Khaleeli, D. J. Tozer, J. Sastre-Garriga, D. H. Miller, and A. J. Thompson. Normal-appearing brain T1 relaxation time predicts

disability in early primary progressive multiple sclerosis. *Arch Neurol*, 64(3):411–5, 2007.

[3] J. Vymazal, A. Righini, R. A. Brooks, M. Canesi, C. Mariani, M. Leonardi, and G. Pezzoli. T1 and T2 in the brain of healthy subjects, patients with Parkinson disease, and patients with multiple system atrophy: relation to iron content. *Radiology*, 211(2):489–95, 1999.

[4] S. Baudrexel, L. Nurnberger, U. Rub, C. Seifried, J. C. Klein, T. Deller, H. Steinmetz, R. Deichmann, and R. Hilker. Quantitative mapping of T1 and T2* discloses nigral and brainstem pathology in early Parkinson's disease. *Neuroimage*, 51(2):512–20, 2010.

[5] P. B. Kingsley. Methods of measuring spin-lattice (T1) relaxation times: an annotated bibliography. *Concepts Magn Reson*, 11(4):243–276, 1999.

[6] L. E. Drain. A direct method of measuring nuclear spin-lattice relaxation times. *Proc Phys Soc A*, 62(5):301–306, 1949.

[7] E. L. Hahn. An accurate nuclear magnetic resonance method for measuring spin-lattice relaxation times. *Phys Rev*, 76(1):145–146, 1949.

[8] D. C. Look and D. R. Locker. Time saving in measurement of NMR and EPR relaxation times. *Rev Sci Instrum*, 41:250–251, 1970.

[9] G. Brix, L. R. Schad, M. Deimling, and W. J. Lorenz. Fast and precise T1 imaging using a TOMROP sequence. *Magn Reson Imaging*, 8(4):351–6, 1990.

[10] E. K. Fram, R. J. Herfkens, G. A. Johnson, G. H. Glover, J. P. Karis, A. Shimakawa, T. G. Perkins, and N. J. Pelc. Rapid calculation of T1 using variable flip angle gradient refocused imaging. *Magn Reson Imaging*, 5(3):201–208, 1987.

[11] S. C. Deoni, B. K. Rutt, and T. M. Peters. Rapid combined T1 and T2 mapping using gradient recalled acquisition in the steady state. *Magn Reson Med*, 49(3): 515–26, 2003.

[12] N. Stikov, M. Boudreau, I. R. Levesque, C. L. Tardif, J. K. Barral, and G. B. Pike. On the accuracy of T1 mapping: searching for common ground. *Magn Reson Med*, 73(2):514–22, 2015.

[13] S. C. Deoni, T. M. Peters, and B. K. Rutt. High-resolution T1 and T2 mapping of the brain in a clinically acceptable time with DESPOT1 and DESPOT2. *Magn Reson Med*, 53(1):237–41, 2005.

[14] S. C. Deoni, T. M. Peters, and B. K. Rutt. Determination of optimal angles for variable nutation proton magnetic spin-lattice, T1, and spin-spin, T2, relaxation times measurement. *Magn Reson Med*, 51(1):194–9, 2004.

[15] A. P. Crawley, M. L. Wood, and R. M. Henkelman. Elimination of transverse coherences in FLASH MRI. *Magn Reson Med*, 8(3):248–260, 1988.

[16] M. L. Wood and V. M. Runge. Artifacts due to residual magnetization in 3-dimensional magnetic-resonance imaging. *Med Phys*, 15(6):825–831, 1988.

[17] Y. Zur, M. L. Wood, and L. J. Neuringer. Spoiling of transverse magnetization in steady-state sequences. *Magn Reson Med*, 21(2):251–63, 1991.

[18] C. Ganter. Steady state of gradient echo sequences with radiofrequency phase cycling: analytical solution, contrast enhancement with partial spoiling. *Magn Reson Med*, 55(1):98–107, 2006.

[19] R. Treier, A. Steingoetter, M. Fried, W. Schwizer, and P. Boesiger. Optimized and combined T1 and B1 mapping technique for fast and accurate T1 quantification in contrast-enhanced abdominal MRI. *Magn Reson Med*, 57(3):568–76, 2007.

[20] F. H. Epstein, 3rd Mugler, J. P., and J. R. Brookeman. Spoiling of transverse magnetization in gradient-echo (GRE) imaging during the approach to steady state. *Magn Reson Med*, 35(2):237–45, 1996.

[21] R. F. Busse and S. J. Riederer. Steady-state preparation for spoiled gradient echo imaging. *Magn Reson Med*, 45(4):653–61, 2001.

[22] C. Preibisch and R. Deichmann. Influence of RF spoiling on the stability and accuracy of T1 mapping based on spoiled FLASH with varying flip angles. *Magn Reson Med*, 61(1):125–35, 2009.

[23] W. Lin and H. K. Song. Improved signal spoiling in fast radial gradient-echo imaging: applied to accurate T(1) mapping and flip angle correction. *Magn Reson Med*, 62(5):1185–94, 2009.

[24] V. L. Yarnykh. Optimal radiofrequency and gradient spoiling for improved accuracy of T1 and B1 measurements using fast steady-state techniques. *Magn Reson Med*, 63(6):1610–26, 2010.

[25] S. A. Hurley, V. L. Yarnykh, K. M. Johnson, A. S. Field, A. L. Alexander, and A. A. Samsonov. Simultaneous variable flip angle-actual flip angle imaging method for improved accuracy and precision of three-dimensional T1 and B1 measurements. *Magn Reson Med*, 68(1):54–64, 2012.

[26] C. Ganter, M. Settles, I. Dregely, F. Santini, K. Scheffler, and O. Bieri. B1+-mapping with the transient phase of unbalanced steady-state free precession. *Magn Reson Med*, 70(6):1515–23, 2013.

[27] W. H. Press, S. A. Teukolsky, W. T. Vetterling, and B. P. Flannery. *Numerical Recipes: The Art of Scientific Computing*. Cambridge University Press, Cambridge, 2007.

[28] S. C. Deoni. High-resolution T1 mapping of the brain at 3T with driven equilibrium single pulse observation of T1 with high-speed incorporation of RF field inhomogeneities (DESPOT1-HIFI). *J Magn Reson Imaging*, 26(4):1106–11, 2007.

[29] J. P. Wansapura, S. K. Holland, R. S. Dunn, and Jr. Ball, W. S. NMR relaxation times in the human brain at 3.0 Tesla. *J Magn Reson Imaging*, 9(4):531–8, 1999.

[30] G. J. Stanisz, E. E. Odrobina, J. Pun, M. Escaravage, S. J. Graham, M. J. Bronskill, and R. M. Henkelman. T1, T2 relaxation and magnetization transfer in tissue at 3T. *Magn Reson Med*, 54(3):507–12, 2005.

[31] H. R. Underhill, C. Yuan, and V. L. Yarnykh. Direct quantitative comparison between cross-relaxation imaging and diffusion tensor imaging of the human brain at 3.0 T. *Neuroimage*, 47(4):1568–78, 2009.

[32] R. Heule, P. Bar, C. Mirkes, K. Scheffler, S. Trattnig, and O. Bieri. Triple-echo steady-state T2 relaxometry of the human brain at high to ultra-high fields. *NMR Biomed*, 27(9):1037–45, 2014.

[33] M. Weigel. Extended phase graphs: dephasing, RF pulses, and echoes - pure and simple. *J Magn Reson Imaging*, 41(2):266–95, 2015.

[34] S. M. Smith, M. Jenkinson, M. W. Woolrich, C. F. Beckmann, T. E. J. Behrens, H. Johansen-Berg, P. R. Bannister, M. De Luca, I. Drobnjak, D. E. Flitney, R. K. Niazy, J. Saunders, J. Vickers, Y. Y. Zhang, N. De Stefano, J. M. Brady, and P. M. Matthews. Advances in functional and structural MR image analysis and implementation as FSL. *Neuroimage*, 23:S208–S219, 2004.

[35] R. W. Cox. AFNI: software for analysis and visualization of functional magnetic resonance neuroimages. *Comput Biomed Res*, 29(3):162–73, 1996.

[36] H. L. M. Cheng and G. A. Wright. Rapid high-resolution T1 mapping by variable flip angles: accurate and precise measurements in the presence of radiofrequency field inhomogeneity. *Magn Reson Med*, 55(3):566–574, 2006.

[37] R. D. Dortch, K. Li, D. F. Gochberg, E. B. Welch, A. N. Dula, A. A. Tamhane, J. C. Gore, and S. A. Smith. Quantitative magnetization transfer imaging in human brain at 3 T via selective inversion recovery. *Magn Reson Med*, 66(5): 1346–52, 2011.

[38] S. C. Deoni, M. J. Josseau, B. K. Rutt, and T. M. Peters. Visualization of thalamic nuclei on high resolution, multi-averaged T1 and T2 maps acquired at 1.5 T. *Hum Brain Mapp*, 25(3):353–9, 2005.

[39] S. C. Deoni, S. C. Williams, P. Jezzard, J. Suckling, D. G. Murphy, and D. K. Jones. Standardized structural magnetic resonance imaging in multicentre studies using quantitative T1 and T2 imaging at 1.5 T. *Neuroimage*, 40(2):662–71, 2008.

Chapter 3

Rapid estimation of cartilage T_2 with reduced T_1 sensitivity using double-echo steady-state imaging

A modified version of this chapter has been published as:
Heule R, Ganter C, Bieri O. Rapid estimation of cartilage T_2 with reduced T_1 sensitivity using double echo steady state imaging. Magn Reson Med, 71(3):1137-1143, 2014.

3.1 Introduction

Transverse relaxation (T_2) is a fundamental parameter in MR, reflecting the interaction of water molecules on a cellular level. Hence, it is able to detect tissue alterations with high specificity and sensitivity, and its quantification, being objective and bias-free, has attracted increased interest as a potential biomarker for the detection of even subtle or diffuse pathological changes.

In principle, single-echo spin-echo (SE) techniques offer precise estimation of T_2, but require multiple scans and are hence too time-consuming for clinical use. As a result, in practice, multi-echo spin-echo methods are used, allowing estimation of T_2 from one single scan. In the presence of transmit field (B_1) heterogeneities, however, imperfect refocusing pulses lead, due to stimulated echo contributions, to an overestimation of T_2 [1]. Furthermore, especially at ultra-high field strengths, short echo spacing is likely to be restricted by the specific absorption rate (SAR).

Fast imaging, such as steady-state free precession (SSFP) techniques [2], shows potential for rapid and accurate relaxometry with good spatial coverage, offering high resolution and short acquisition times as required for clinical acceptance and practice. SSFP-based quantitative imaging can be classified into transient and steady-state methods: transient techniques make use of the time-dependent approach of the magnetization to steady state [3–7], whereas steady-state techniques use the functional dependence of the dynamic equilibrium to relaxation parameters [8–14].

In contrast to transient methods, steady-state techniques are considerably faster: using a variable flip angle technique, the feasibility of high-resolution T_2 mapping was demonstrated in-vivo based on two balanced SSFP scans, however, requiring prior knowledge of the longitudinal relaxation (T_1) for accurate T_2 estimation [10, 12]. Furthermore, balanced SSFP suffers from off-resonance related banding artifacts and phase cycling is likely to be needed in the presence of strong susceptibility variation [11]. A similar, but off-resonance insensitive method for fast T_2 quantification is based on partial spoiling of the free induction decay (FID) of two non-balanced SSFP scans [14]. It allows accurate estimation of T_2 in the limit of large flip angles, $\alpha \sim 90°$, but becomes more and more biased by T_2/T_1 with decreasing flip angles. Since generally signal-to-noise ratio (SNR) is low for SSFP in this limit, in practice, smaller flip angles are required and thus, some systematic error in the estimated T_2 values must be expected, especially for $T_2/T_1 \sim 1$ that is for fluids.

Only recently, a double-echo steady-state (DESS) technique was proposed for rapid estimation of cartilage T_2 [13]. In contrast to the aforementioned dual-scan SSFP techniques, only one scan is required for DESS-T_2 mapping: relaxometry is based on the signal ratio of the SSFP-FID and the SSFP-Echo signal acquired within every repetition time (TR). Similar to partial spoiling, the ratio of these two signals becomes independent of T_1 only in the limit of $\alpha \sim 90°$. However, to achieve sufficient SNR for cartilage imaging, much reduced flip angles have to be used, leading to systematic deviations between the estimated and true T_2 values, clearly observable for flip angles lower than about 45° [13].

Morphological DESS imaging offers high contrast between cartilage and synovial fluid and has demonstrated successful detection of chondral abnormalities [15, 16]. Not surprisingly, it is becoming increasingly popular: recently, sagittal 3D DESS with

water-selective excitation has been included into the acquisition protocol of the osteoarthritis initiative a multi-center, longitudinal study aiming to establish a large database for knee osteoarthritis [17–19]. Ideally, morphological and quantitative approaches should be used complimentary in order to assess the status and progression of knee osteoarthritis [20]. DESS has the unique potential to simultaneously obtain morphological as well as biochemical information about cartilage from only one single high-resolution data set, but unfortunately requires diametrical flip angle settings: high flip angles for accurate T_2 estimation, and low ones for morphological imaging.

In this work, we show that based on a rough global T_1 estimator, a considerable reduction in the systematic error of DESS-T_2 can be achieved. The improvement becomes especially prominent in the low flip angle regime ($\alpha < 45°$), as commonly used for morphological DESS imaging ideally 20° to 25° at 3 Tesla (T) as reported in Refs. [21] and [22], respectively. For these reasons, the proposed method is of high interest for rapid combined morphological and accurate quantitative T_2 imaging of the musculoskeletal system.

3.2 Methods

All numerical simulations, data analysis and visualization were done using Matlab 7.5 (The MathWorks, Inc., Natick, MA). Simulations were performed with a TR of 10 ms, echo time (TE) → 0 ms, and assuming a true T_2 of 35 ms (cartilage at 3 T (23)). As global T_1 estimate, a value of 1200 ms was used in all simulations as well as for the in vivo T_2 quantification of patellar cartilage at 3 T [23, 24].

3.2.1 DESS signals

DESS sequences, as presented by Bruder et al. [25] or Redpath et al. [26], acquire two separate SSFP echoes within every TR (see Fig. 3.1 a), denoted FID (or S^+) and Echo (S^-). Since the S^- signal is partially made up of the S^+ signal refocused from the previous TR interval, it is sometimes considered as a time-reversed FID. The contrast of the FID is mainly determined by T_1/T_2, whereas the Echo shows for TR ~ T_2 a strong T_2 weighting. DESS imaging thus allows the simultaneous acquisition of two images with markedly different contrasts (see Figs. 3.1 b and 3.1 c). As shown in Ref. [27], analytical expressions for the S^+ signal (acquired just after the RF pulse, i.e. at t → 0) and the S^- signal (acquired just before the RF pulse, i.e. at t → TR) are

$$S^+(\alpha, \mathrm{TR}, T_1, T_2) \propto 1 - (E_1 - \cos\alpha)\cdot r \quad \text{and} \tag{3.1}$$

$$S^-(\alpha, \mathrm{TR}, T_1, T_2) \propto 1 - (1 - E_1\cos\alpha)\cdot r \tag{3.2}$$

using the definitions

$$\begin{aligned} E_{1,2} &:= \exp(-\mathrm{TR}/T_{1,2}),\\ p &:= 1 - E_1\cos\alpha - E_2^2(E_1 - \cos\alpha),\\ q &:= E_2(1 - E_1)(1 + \cos\alpha),\\ r &:= (1 - E_2^2)(p^2 - q^2)^{-1/2}. \end{aligned}$$

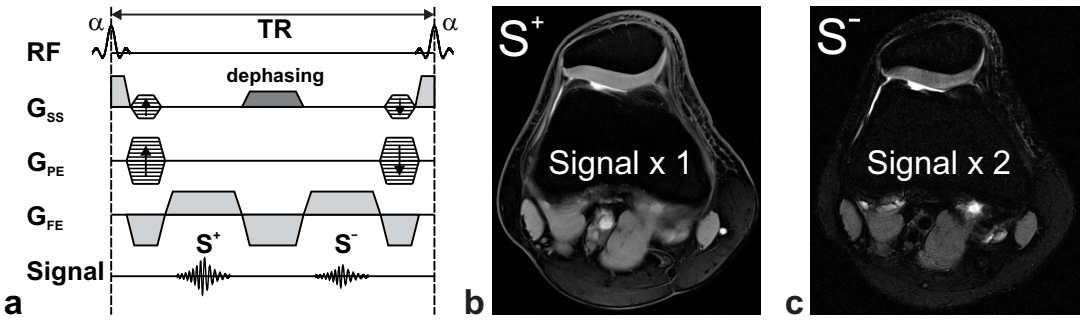

Figure 3.1: (a) 3D DESS sequence scheme. Two echoes are formed within every TR: the first one refers to the SSFP-FID (denoted by S^+) and the second one to the SSFP-Echo (S^-) signal. Dephasing is applied along the slice selection direction to minimize the loss of contrast between fluids and tissues due to diffusion. (b) SSFP-FID (S^+) and (c) SSFP-Echo (S^-) images obtained from one axial DESS scan of the knee joint at 3 T.

For $\alpha = 90°$ (and for $E_1 \to 1$), it is found that the S^- signal is primarily composed of the S^+ signal refocused after two repetition times,

$$S^-_{\alpha=90°}(\mathrm{TR}, T_1, T_2) \approx S^+_{\alpha=90°} \cdot \exp\left(\frac{-2 \cdot \mathrm{TR}}{T_2}\right). \tag{3.3}$$

As a result, the signal ratio $s := S^-/S^+$ becomes in this limit independent of T_1 and reads

$$s_{\alpha=90°}(\mathrm{TR}, T_1, T_2) \approx \exp\left(\frac{-2 \cdot \mathrm{TR}}{T_2}\right). \tag{3.4}$$

3.2.2 T_2 mapping with DESS

Generally, all factors leading to inconsistencies between the theoretical framework and the experiment, such as magnetization transfer [28] or diffusion [29–32], may adversely affect quantification accuracy. In contrast to balanced SSFP, from the long TR and the low flip angles used with DESS, magnetization transfer effects are expected to be negligible. However, the expected signal modulations from diffusion, being especially prominent in the Echo in the low flip angle regime [30] and at high-resolution [32], may result in a loss of contrast between fluids and tissues. To address this issue, a rephased 3D DESS sequence [32] was used (recall Fig. 3.1 a). Here, frequency encoding is rephased, i.e. balanced, and spin dephasing applied along the direction of slice encoding which is typically the lowest resolution axis (being in contrast to the common DESS scheme where dephasing is applied along the frequency encoding axis).

Taking into account that the S^+ and S^- signals are acquired with t = TE rather than t = 0 and t = TR−TE rather than t = TR, respectively (see Fig. 3.1 a), Eq. (3.4) can be used to yield an estimate for T_2 from the measured $s_{\mathrm{meas}} := S^-_{\mathrm{meas}}/S^+_{\mathrm{meas}}$ signal

intensities, according to Ref. [13]

$$T_2|_{\alpha=90^\circ} \approx \frac{-2 \cdot (\mathrm{TR} - \mathrm{TE})}{\ln(s_{\mathrm{meas}})}. \tag{3.5}$$

A T_2 rather than a T_2^* weighting is introduced to Eq. (3.5); the error arising from this approximation is small for short enough TE as reported in Ref. [25]. Generally, Eq. (3.5) is a good approximation for $\alpha \sim 90^\circ$, but becomes more and more biased by T_1 with decreasing flip angles. Thus in general, the equation to solve is given by

$$s_{\mathrm{meas}} = s_{\alpha,\mathrm{TR},\mathrm{TE}}(T_1, T_2) \tag{3.6}$$

with

$$s_{\alpha,\mathrm{TR},\mathrm{TE}}(T_1, T_2) := \frac{S^-(\alpha, \mathrm{TR}, T_1, T_2)}{S^+(\alpha, \mathrm{TR}, T_1, T_2)} \cdot \exp\left(\frac{2 \cdot \mathrm{TE}}{T_2}\right).$$

The left-hand side of Eq. (3.6) represents the measured signal ratio between the two echoes whereas the right-hand side derives from given protocol specific extrinsic parameters (α, TR, and TE) and from variable intrinsic relaxation times (T_1 and T_2). We try to solve Eq. (3.6) using prior knowledge about T_1. To this end, we make use of a simple global T_1 estimator ($T_{1,\mathrm{est}}$) and define a search interval for T_2 with a (dummy) upper guess of $T_{2,u} = 5$ s. Then, Eq. (3.6) can be solved by numerical minimization:

$$T_2|_{T_1=T_{1,\mathrm{est}}} = \arg\,\min\{T_2 \in [0, T_{2,u}] : |s_{\mathrm{meas}} - s_{\alpha,\mathrm{TR},\mathrm{TE},T_{1,\mathrm{est}}}(T_2)|\}. \tag{3.7}$$

A golden section search [33] is used as fast minimization method since this algorithm calls the function in each step only once without time-consuming evaluations of the functions derivative. This approach is appropriate for functions that are continuous over the minimization interval containing only one minimum, as in our case (Fig. 3.2). In each step, the algorithm brackets the minimum and shortens the search interval by $(-1 + \sqrt{5})/2)$. Therefore, the ratio of the new interval and the preceding one is just the one of the golden mean, and hence the name. The algorithm stops as soon as the size of the bracketing interval reaches a user defined convergence tolerance, i.e. 0.1 ms. Using an upper guess of $T_{2,u} = 5$ s and a convergence tolerance of 0.1 ms, typically, only of the order of 20 iterations (or functions evaluations) are required until convergence of the golden section search algorithm. The relative residual T_1-related error in T_2 either derived from Eq. (3.5) or Eq. (3.7), is estimated in simulations from $\mathrm{abs}[(T_2|_{\alpha=90^\circ} - T_2)/T_2]$ or $\mathrm{abs}[(T_2|_{T_1=T_{1,\mathrm{est}}} - T_2)/T_2]$, given and displayed in percentage units.

3.2.3 In vivo experiments

In vivo anisotropic 3D DESS scans of the human knee joint were performed on a 3 T system (Magnetom Verio, Siemens Medical Solution, Erlangen, Germany) using a dedicated 15-channel transmit and receive knee coil (Quality Electrodynamics, Mayfield Village, OH). Morphological DESS images refer to the combined magnitude image of the corresponding FID and Echo signals, $|S^+| + |S^-|$. The field-of-view (FOV) was rectangular with a matrix size of 384 × 312, resulting in an in-plane resolution of 0.4

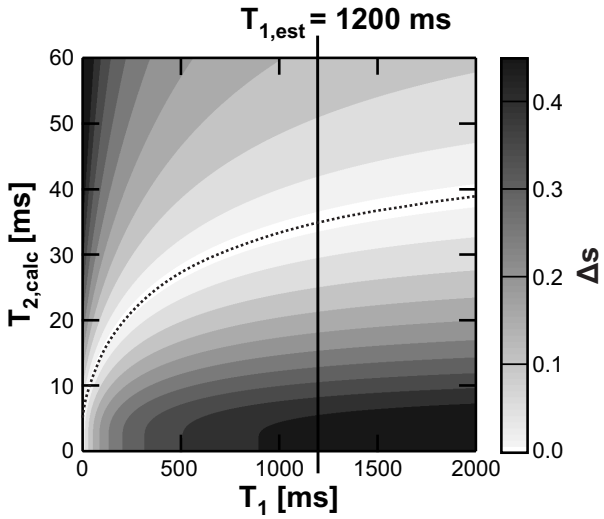

Figure 3.2: Contour plot of Δs – the function to minimize in order to find the true T_2 of the tissue, $\Delta s(T_1, T_{2,\mathrm{calc}}) := \mathrm{abs}[s_{\alpha,\mathrm{TR},\mathrm{TE},T_2}(T_1) - s_{\alpha,\mathrm{TR},\mathrm{TE},T_{1,\mathrm{est}}}(T_{2,\mathrm{calc}})]$ – versus T_1 (true) and T_2 (calculated) for a flip angle of 15°. Here, $s_{\alpha,\mathrm{TR},\mathrm{TE},T_2}(T_1)$ can be considered as a simulation of the measured signal ratio, $S^-_{\mathrm{meas}}/S^+_{\mathrm{meas}}$, with T_1 and T_2 representing the true relaxation times of the tissue. T_1 is kept variable whereas T_2 is fixed to 35 ms. As global estimator for T_1 a value of 1200 ms is used which goes into the ratio $s_{\alpha,\mathrm{TR},\mathrm{TE},T_{1,\mathrm{est}}}(T_{2,\mathrm{calc}})$, yielding an estimate for T_2, denoted here $T_{2,\mathrm{calc}}$. The dotted line tracks the minimal values of Δs along T_1 revealing that there is a global minimum for any T_1. The gradient of the dashed curve gives a measure for the sensitivity of the T_2 calculation to T_1.

× 0.4 mm^2, and 12 axial slices with 2.5 mm thickness were acquired. Other imaging parameters included a bandwidth of 334 Hz/pixel, a TR of 14.2 ms, and a TE of 3.97 ms. In order to enhance the SNR in the base data, three averages of the DESS scan were taken, yielding a total acquisition time of 3 min 15 s. All images were obtained with water-selective excitation pulses to reduce chemical shift artifacts and enhance the contrast at the interface of bone and cartilage. Results are shown for scans at two different nominal flip angles (15° and 45°) to probe for the residual T_1-related bias in the T_2 estimates using Eqs. (3.5) and (3.7).

Transverse relaxation times were calculated pixel-wise from the FID and Echo images based on Eqs. (3.5) and (3.7), both offline using Matlab and online using a free scripting language (Lua) [34]. In addition, to assess zonal T_2 variation, regions of interest (ROIs) in the patella were subdivided into deep and superficial cartilage layers. Only the central slices within the excited 3D volume were used for the evaluation to avoid possible issues from slice profile effects.

For reference, a single-echo SE technique was used for T_2 calculation. We decided on a single-echo rather than a multi-echo approach to avoid errors in the estimated T_2 arising from stimulated echo contributions. Six consecutive single-echo SE scans with echo times ranging from 11 ms up to 76 ms were performed. Resolution, matrix size, slice thickness and positioning were identical to the DESS measurements in order to

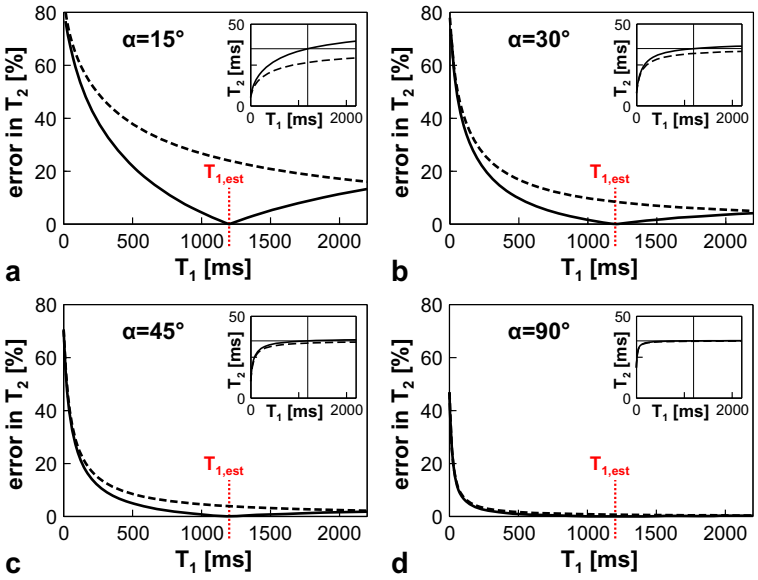

Figure 3.3: Plots of the error in the T_2 calculation versus the true T_1 of the tissue for flip angles α of (a) 15°, (b) 30°, (c) 45°, and (d) 90°. The true T_2 of the tissue is set to 35 ms. The insets show the corresponding calculated T_2 values (the thin horizontal line identifies the value of the true T_2, the thin vertical line the value of $T_{1,\mathrm{est}}$). The approximate T_2 quantification in the limit of $\alpha = 90°$ (dashed line), cf. Eq. (3.5), is compared to the new method using a global T_1 guess of 1200 ms (solid line), cf. Eq. (3.7).

ensure exact comparability. A bandwidth of 228 Hz/Pixel was used, yielding a TR of 1330 ms and an acquisition time of 2 min 56 s for one single-echo SE scan.

3.3 Results

Simulations reveal that the T_1-related bias for DESS-based T_2 calculation can considerably be reduced over a large range of T_1 values (0.5 s < T_1 < 2 s) using a global estimator of $T_1 = 1200$ ms compared to the T_2 approximation derived in the $\alpha = 90°$ limit (Fig. 3.3). The improvement is particularly evident in the range of low flip angles ($\alpha < 45°$) while the two approaches converge towards the limit of $\alpha = 90°$, as can be expected (see Eq. (3.5)). Furthermore, it can be seen from the insets of Figure 3.3 that the approximate calculation underestimates T_2 for tissues characterized by any T_1. The new method proposed here, on the other hand, underestimates T_2 only if the global T_1 estimator is larger than the true T_1 of the tissue. Otherwise T_2 is overestimated. Coincides the estimate with the true T_1, the error in the T_2 calculation becomes minimal.

The same behavior is observed for in vivo T_2 quantification of patellar articular cartilage in the knee joint (Fig. 3.4). DESS-T_2 mapping is demonstrated at low (15°) and intermediate (45°) flip angles (Figs. 3.4 a and 3.4 b) and compared to a contemporary single-echo SE method (Fig. 3.4 c). Morphological DESS imaging is preferably

performed in the low flip angle regime (at $\alpha \sim 20 - 25°$), due to contrast and SNR reasons [21, 22]. Similar results are reported in Ref. [35] for quantitative diffusion-weighted DESS imaging where a flip angle of 15° revealed to be optimal with respect to SNR.

At such a dedicated, low flip angle, the color-coded T_2 map obtained with DESS using a global T_1 estimate of 1200 ms shows clearly elevated T_2 values as opposed to the approximate calculation using Eq. (3.5) (Fig. 3.4 a). As it is known from Figure 3.3, T_2 is considerably underestimated in the low flip angle regime when completely neglecting the dependence of the signal ratio upon T_1. Hence, the observed increase in T_2 indicates that even a rough global T_1 estimator may markedly reduce the sensitivity of the T_2 calculation to T_1. The difference between the two methods diminishes as the flip angle increases, and at 45° both T_2 maps become comparable (Fig. 3.4 b), in accordance with the results obtained in Ref. [13].

In Figure 3.4 c, reference T_2 mapping based on a single-echo SE technique is shown and reveals excellent correspondence between SE-T_2 and DESS-T_2 at 45°. While this result is rather expected because of the negligible T_1-dependence in this limit [13], it is remarkable to observe good correspondence even at a much reduced flip angle of 15° if a global T_1 estimate is used to calculate T_2.

Considering the zonal organization, cartilage layers are subdivided into a superficial zone located near the articular surface and a deep zone oriented towards the bone-cartilage interface (see dotted curve in Fig. 3.4 which divides the two areas). Overall, higher T_2 values are observed in the superficial layer in comparison to the deep one. This spatial variation in T_2 is an expected feature of cartilage in the knee joint [36, 37]. Mean DESS-T_2 values calculated based on a global T_1 guess and evaluated for the deep area at flip angles of 15° and 45°, respectively, are: 24.1 ± 6.0 ms (18.1 ± 3.7 ms) and 24.7 ± 5.5 ms (23.7 ± 5.2 ms), where, in brackets, mean T_2 values derived according to Ref. [13] are given for reference. Corresponding values for the superficial zone are: 31.2 ± 5.6 ms (22.3 ± 3.0 ms) and 31.3 ± 6.2 ms (29.8 ± 5.5 ms). T_2 calculation based on six consecutive single-echo SE scans yields mean T_2 values of 24.5 ± 6.7 ms and 31.0 ± 5.7 ms for the deep and superficial regions, respectively. All values refer to the T_2 maps shown in Figure 3.4.

3.4 Discussion and conclusions

We have shown that a considerable reduction in the T1-related bias for DESS-based T_2 estimation can be achieved by using a simple global T_1 estimate. The introduced new T_2 quantification method removes the constraint on finding a compromise between morphological contrast (SNR) and T_2 accuracy, and results overall in an improvement of DESS-T_2 mapping. If strong correlations between T_1 and T_2 are observed, it might be possible to improve the suggested procedure even further by using an estimation of the T_1 versus T_2 correlation instead of just a simple global T_1 guess. Moreover, DESS-T_2 relaxometry can be combined with DESS-based diffusion imaging, only requiring one extra diffusion-weighted scan with additional dephasing moments [35].

Furthermore, rather unanticipated, we observe enhanced zonal variation in T_2 between deep and superficial cartilage layers (see Fig. 3.5). Mean T_2 values are plotted

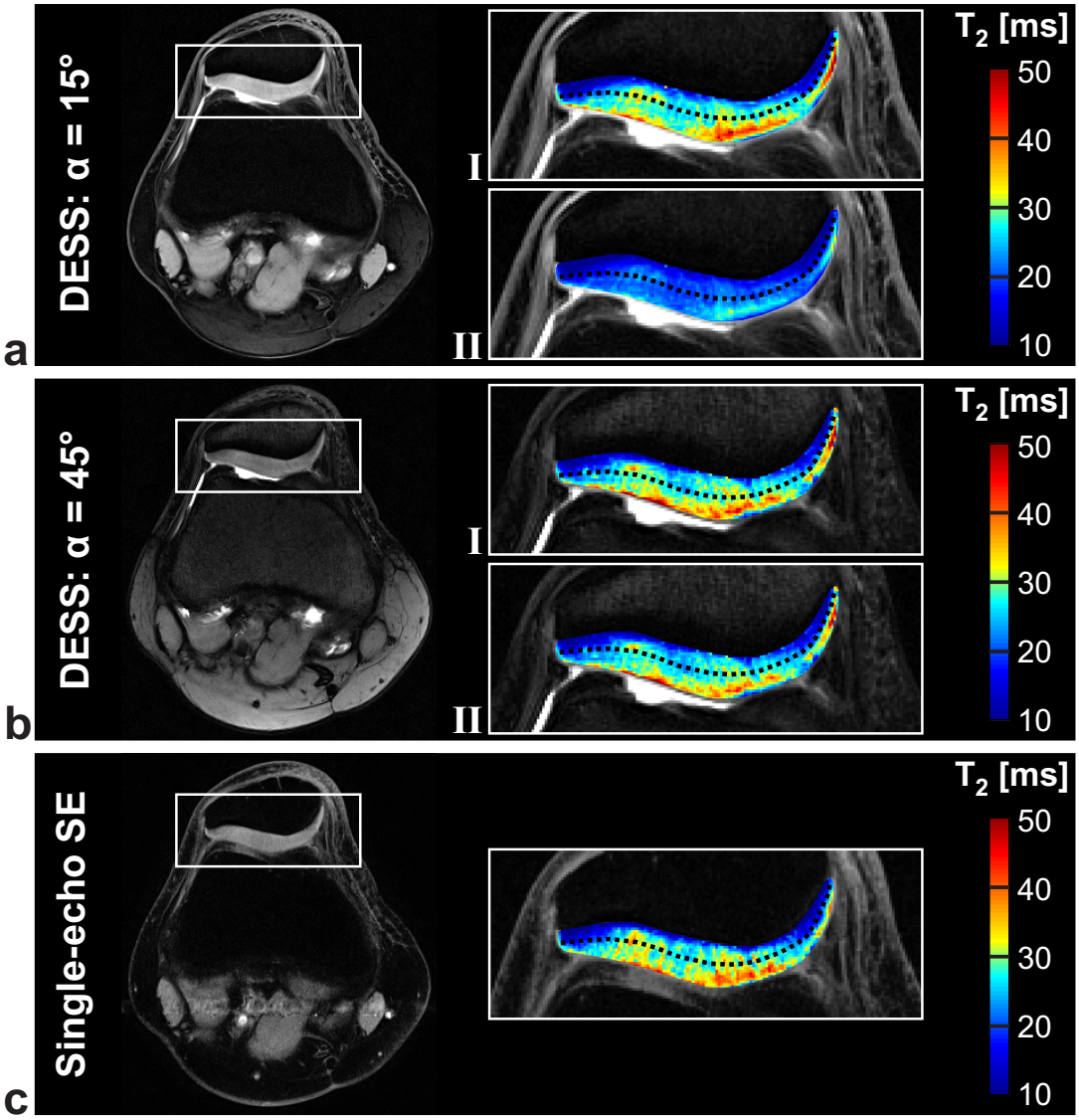

Figure 3.4: Morphological DESS images at 3 T of a healthy volunteer with colored T_2 maps of patellar cartilage in the knee joint for flip angles of 15° (a) and 45° (b). T_2 mapping with reduced T_1 sensitivity using a global estimator for T_1 is shown in (I). For comparison, approximate T_2 quantification derived in the $\alpha = 90°$ limit as proposed in Ref. [13] is also shown (II). DESS-T_2 mapping is compared to a reference calculation based on six consecutive single-echo SE scans (c). The dotted black curve subdivides the patellar cartilage layers into two regions of interest: deep (above) and superficial (below).

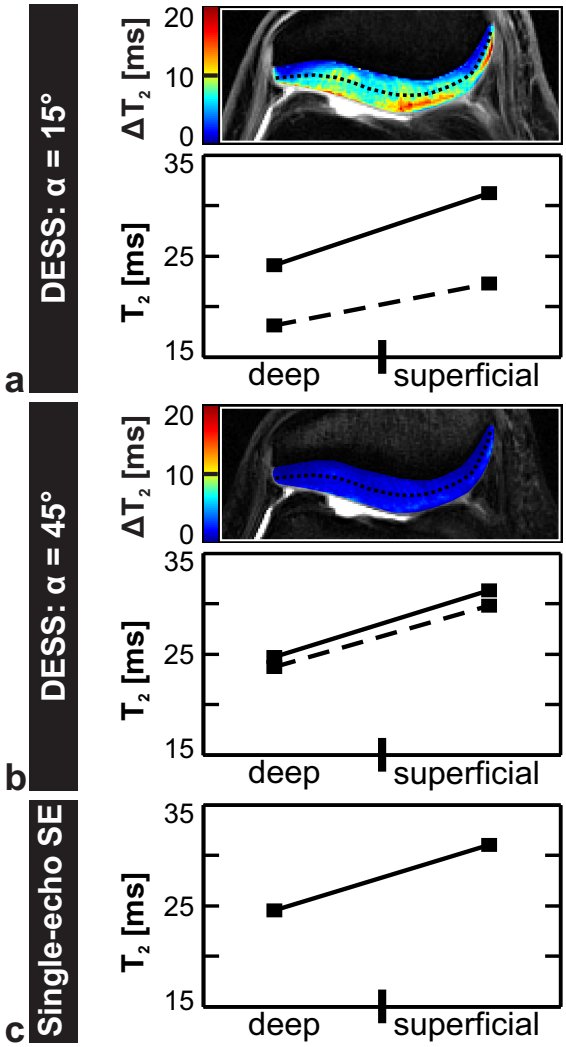

Figure 3.5: Zonal variation in T_2 from deep to superficial cartilage areas of the patella is illustrated for the three cases shown in Figure 3.4, corresponding to DESS-measurements at flip angles of 15° (a) and 45° (b) as well as to a reference single-echo SE-measurement (c). Mean T_2 values are plotted for deep and superficial cartilage layers as assessed for the two regions of interest divided by the dotted black curve (see Fig. 3.4). Solid and dashed lines in (a) and (b) refer to the here proposed method with reduced T_1 sensitivity and to the approximate T_2 calculation derived in the $\alpha = 90°$ limit, respectively. Color maps of the absolute difference between the T_2 values obtained using these two methods, denoted ΔT_2, are shown additionally. Again, the dotted line subdivides the patellar cartilage zones into deep (above) and superficial (below).

as assessed for deep and superficial regions of interest. At low flip angle (here, 15°), the gradient in T_2 from deep to superficial is increased for the DESS-T_2 calculation if we make use of prior knowledge about T_1. The enhancement is clearly visible in the corresponding color-coded difference map (see Fig. 3.5 a). At 45°, the influence of T_1 vanishes and the two methods do not differ considerably as expected (Fig. 3.5 b). For comparison, zonal variation obtained with a reference SE-T_2 measurement is plotted as well, indicating good agreement with the here proposed method to estimate DESS-T_2 (Fig. 3.5 c). Recent studies suggest that spatial analysis could improve the classification between subjects with and without osteoarthritis [38] as well as increase the sensitivity to detect longitudinal T_2 changes [39]. Hence, the observed increased gradient depicts a further benefit of using a global T_1 estimator for T_2 quantification and emphasizes the potential of DESS-T_2 to act as a biomarker for the detection of early degenerative changes in cartilage.

In conclusion, our results accentuate the unique possibility offered by DESS to combine accurate quantitative T_2 and morphological image analysis of the musculoskeletal system with high resolution.

References

[1] R. M. Lebel and A. H. Wilman. Transverse relaxometry with stimulated echo compensation. *Magn Reson Med*, 64(4):1005–14, 2010.

[2] H. Y. Carr. Steady-state free precession in nuclear magnetic resonance. *Phys Rev*, 112(5):1693–1701, 1958.

[3] D. C. Look and D. R. Locker. Time saving in measurement of NMR and EPR relaxation times. *Rev Sci Instrum*, 41:250–251, 1970.

[4] K. Scheffler and J. Hennig. T(1) quantification with inversion recovery TrueFISP. *Magn Reson Med*, 45(4):720–3, 2001.

[5] K. Scheffler. On the transient phase of balanced SSFP sequences. *Magn Reson Med*, 49(4):781–3, 2003.

[6] P. Schmitt, M. A. Griswold, P. M. Jakob, M. Kotas, V. Gulani, M. Flentje, and A. Haase. Inversion recovery TrueFISP: quantification of T(1), T(2), and spin density. *Magn Reson Med*, 51(4):661–7, 2004.

[7] P. Ehses, N. Seiberlich, Ma D., Breuer F. A., P. M. Jakob, M. A. Griswold, and V. Gulani. IR TrueFISP with a golden-ratio-based radial readout: fast quantification of T1, T2, and proton density. *Magn Reson Med*, 69(1):71–81, 2013.

[8] K. A. Christensen, D. M. Grand, E. M. Schulman, and C. Walling. Optimal determination of relaxation times of Fourier transform nuclear magnetic resonance. determination of spin-lattice relaxation times in chemically polarized species. *J Phys Chem*, 78:1971–1977, 1974.

[9] J. Homer and M. S. Beevers. Driven-equilibrium single-pulse observation of T1 relaxation. A reevaluation of a rapid "new" method for determining NMR spin-lattice relaxation times. *J Magn Reson*, 63(2):287–297, 1985.

[10] S. C. Deoni, B. K. Rutt, and T. M. Peters. Rapid combined T1 and T2 mapping using gradient recalled acquisition in the steady state. *Magn Reson Med*, 49(3): 515–26, 2003.

[11] S. C. Deoni, H. A. Ward, T. M. Peters, and B. K. Rutt. Rapid T2 estimation with phase-cycled variable nutation steady-state free precession. *Magn Reson Med*, 52 (2):435–9, 2004.

[12] S. C. Deoni, T. M. Peters, and B. K. Rutt. High-resolution T1 and T2 mapping of the brain in a clinically acceptable time with DESPOT1 and DESPOT2. *Magn Reson Med*, 53(1):237–41, 2005.

[13] G. H. Welsch, K. Scheffler, T. C. Mamisch, T. Hughes, S. Millington, M. Deimling, and S. Trattnig. Rapid estimation of cartilage T2 based on double echo at steady state (DESS) with 3 Tesla. *Magn Reson Med*, 62(2):544–9, 2009.

[14] O. Bieri, K. Scheffler, G. H. Welsch, S. Trattnig, T. C. Mamisch, and C. Ganter. Quantitative mapping of T2 using partial spoiling. *Magn Reson Med*, 66(2): 410–8, 2011.

[15] T. J. Mosher and S. W. Pruett. Magnetic resonance imaging of superficial cartilage lesions: role of contrast in lesion detection. *J Magn Reson Imaging*, 10(2): 178–82, 1999.

[16] S. Ruehm, M. Zanetti, J. Romero, and J. Hodler. MRI of patellar articular cartilage: evaluation of an optimized gradient echo sequence (3D-DESS). *J Magn Reson Imaging*, 8(6):1246–51, 1998.

[17] F. Eckstein, M. Hudelmaier, W. Wirth, B. Kiefer, R. Jackson, J. Yu, C. B. Eaton, and E. Schneider. Double echo steady state magnetic resonance imaging of knee articular cartilage at 3 Tesla: a pilot study for the Osteoarthritis Initiative. *Ann Rheum Dis*, 65(4):433–41, 2006.

[18] F. Eckstein, M. Kunz, M. Schutzer, M. Hudelmaier, R. D. Jackson, J. Yu, C. B. Eaton, and E. Schneider. Two year longitudinal change and test-retest-precision of knee cartilage morphology in a pilot study for the osteoarthritis initiative. *Osteoarthritis Cartilage*, 15(11):1326–32, 2007.

[19] W. Wirth, M. Nevitt, M. P. Hellio Le Graverand, O. Benichou, D. Dreher, R. Y. Davies, J. Lee, K. Picha, A. Gimona, S. Maschek, M. Hudelmaier, and F. Eckstein. Sensitivity to change of cartilage morphometry using coronal FLASH, sagittal DESS, and coronal MPR DESS protocols–comparative data from the Osteoarthritis Initiative (OAI). *Osteoarthritis Cartilage*, 18(4):547–54, 2010.

[20] F. Eckstein and W. Wirth. Quantitative cartilage imaging in knee osteoarthritis. *Arthritis*, 2011:475684, 2011.

[21] S. Moriya, Y. Miki, Y. Matsuno, and M. Okada. Three-dimensional double-echo steady-state (3D-DESS) magnetic resonance imaging of the knee: establishment of flip angles for evaluation of cartilage at 1.5 T and 3.0 T. *Acta Radiol*, 53(7): 790–4, 2012.

[22] C. G. Peterfy, E. Schneider, and M. Nevitt. The osteoarthritis initiative: report on the design rationale for the magnetic resonance imaging protocol for the knee. *Osteoarthritis Cartilage*, 16(12):1433–41, 2008.

[23] G. E. Gold, E. Han, J. Stainsby, G. Wright, J. Brittain, and C. Beaulieu. Musculoskeletal MRI at 3.0 T: relaxation times and image contrast. *Am J Roentgenol*, 183(2):343–51, 2004.

[24] L. Wang, M. E. Schweitzer, A. Padua, and R. R. Regatte. Rapid 3D-T(1) mapping of cartilage with variable flip angle and parallel imaging at 3.0T. *J Magn Reson Imaging*, 27(1):154–61, 2008.

[25] H. Bruder, H. Fischer, R. Graumann, and M. Deimling. A new steady-state imaging sequence for simultaneous acquisition of two MR images with clearly different contrasts. *Magn Reson Med*, 7(1):35–42, 1988.

[26] T. W. Redpath and R. A. Jones. FADE–A new fast imaging sequence. *Magn Reson Med*, 6(2):224–234, 1988.

[27] W. Hänicke and H. U. Vogel. An analytical solution for the SSFP signal in MRI. *Magn Reson Med*, 49(4):771–5, 2003.

[28] O. Bieri and K. Scheffler. On the origin of apparent low tissue signals in balanced SSFP. *Magn Reson Med*, 56(5):1067–74, 2006.

[29] R. Kaiser, E. Bartholdi, and R. R. Ernst. Diffusion and field-gradient effects in NMR Fourier spectroscopy. *J. Chem. Phys.*, 60:2966–2979, 1974.

[30] E. X. Wu and R. B. Buxton. Effect of diffusion on the steady-state magnetization with pulsed field gradients. *J Magn Reson*, 90(2):243–253, 1990.

[31] D. E. Freed, U. M. Scheven, L. J. Zielinski, P. N. Sen, and M. D. Hürlimann. Steady-state free precession experiments and exact treatment of diffusion in a uniform gradient. *J Chem Phys*, 119(9):4249–58, 2001.

[32] O. Bieri, C. Ganter, and K. Scheffler. On the fluid-tissue contrast behavior of high-resolution steady-state sequences. *Magn Reson Med*, 68(5):1586–92, 2012.

[33] W. H. Press, S. A. Teukolsky, W. T. Vetterling, and B. P. Flannery. *Numerical Recipes: The Art of Scientific Computing*. Cambridge University Press, Cambridge, 2007.

[34] F. Santini, S. Patil, and K. Scheffler. IceLuva: a scripting framework for MR image reconstruction based on free software. *Concepts Magn Reson*, 39B(1): 1–10, 2011.

[35] O. Bieri, C. Ganter, and K. Scheffler. Quantitative in vivo diffusion imaging of cartilage using double echo steady-state free precession. *Magn Reson Med*, 68(3): 720–729, 2012.

[36] B. J. Dardzinski, T. J. Mosher, S. Li, M. A. Van Slyke, and M. B. Smith. Spatial variation of T2 in human articular cartilage. *Radiology*, 205(2):546–50, 1997.

[37] H. E. Smith, T. J. Mosher, B. J. Dardzinski, B. G. Collins, C. M. Collins, Q. X. Yang, V. J. Schmithorst, and M. B. Smith. Spatial variation in cartilage T2 of the knee. *J Magn Reson Imaging*, 14(1):50–5, 2001.

[38] J. Carballido-Gamio, R. Stahl, G. Blumenkrantz, A. Romero, S. Majumdar, and T. M. Link. Spatial analysis of magnetic resonance T1rho and T2 relaxation times improves classification between subjects with and without osteoarthritis. *Med Phys*, 36(9):4059–67, 2009.

[39] J. Carballido-Gamio, G. B. Joseph, J. A. Lynch, T. M. Link, and S. Majumdar. Longitudinal analysis of MRI T2 knee cartilage laminar organization in a subset of patients from the osteoarthritis initiative: a texture approach. *Magn Reson Med*, 65(4):1184–94, 2011.

Chapter 4

Triple-echo steady-state (TESS) relaxometry

A modified version of this chapter has been published as:
Heule R, Ganter C, Bieri O. Triple echo steady-state (TESS) relaxometry. Magn Reson Med, 71(1):230-237, 2014.

4.1 Introduction

Since its introduction more than half a century ago, the use of steady-state free precession (SSFP) [1] has become increasingly popular, and a large number of SSFP imaging techniques have been described so far (e.g., see Handbook of MRI Pulse Sequences [2]). Besides morphological imaging, SSFP has also attracted considerable interest for fast quantitative MRI. Quantitative imaging is thought to represent an important future step towards a significant improvement of the diagnostic potential of MRI, for the early detection of subtle or diffuse pathological changes with high specificity and sensitivity, for an unbiased assessment of treatment or drug effects, as well as for clinical trials in drug research across different sites. Compared to morphological imaging, however, quantification requires longer scan time and the overall success and applicability of quantitative MRI methods in the clinical setting will depend greatly on the overall acquisition speed. As a result, SSFP-based imaging techniques have come into the research focus, e.g. for relaxation time mapping [3–10], for measuring molecular proton diffusion [11–15], for the assessment of magnetization transfer effects [16–18], or for the characterization of flow or motion [19–21].

Relaxation is one of the most fundamental fingerprints of NMR: It not only defines contrast in conventional MRI, but also reflects the local interaction of water on a molecular and thus very fundamental level. Longitudinal relaxation (T_1) is typically assessed from inversion recovery (IR) spin-echo (SE) techniques whereas transverse relaxation (T_2) is commonly based on sampling the decay of the transverse magnetization using single-echo or multi-echo SE methods. Acquiring the complete T_1 recovery or T_2 decay curve is time-consuming and frequently requires segmented imaging strategies. In contrast, quantification techniques that make use of the functional dependence of the steady state on its intrinsic and extrinsic parameters are considerably faster. A common feature of rapid SSFP sequences is their mixed T_2/T_1 imaging contrast; a natural consequence of a pulse repetition time (TR) being much shorter than T_2. As a result, accurate quantification of relaxation times using SSFP-based imaging techniques is hampered by a varying marginal T_2-related bias in T_1 estimates, as seen in RF spoiled SSFP [22], or by a more or less pronounced T_1-related bias in T_2, as seen in balanced SSFP [23], partially spoiled SSFP [10], and double-echo SSFP [9]. Moreover, all SSFP imaging techniques proposed so far, as well as multi-echo SE techniques commonly used for T_2 mapping, are highly sensitive to transmit field (B_1) inhomogeneities that become especially prominent at high (3 Tesla) to ultra-high (7 Tesla and higher) field strength. As a result, without additional corrective data, accurate and thus fast and reliable quantification of relaxation times is not feasible in practice.

In summary, several different steady-state methods have been proposed for relaxometry, but none are perfect: all of them are B_1-sensitive, require multiple scans (except for the dual echo approach [9]), suffer from a T_2/T_1 related bias, or are prone to static (B_0) field inhomogeneities [24]. Hence, there is much room for methodological improvement. In this work, we present a completely new approach for rapid quantification of both, T_1 and T_2 relaxation times, within one single scan using a triple-echo steady-state (TESS) approach. Here, we make use of the different functional dependence of the two lowest order SSFP-FID modes (FID: free induction decay) and of

the lowest order SSFP-Echo mode, acquired within every TR, for rapid relaxometry using an iterative golden section search algorithm. The accuracy of TESS-based relaxometry is evaluated from simulations and in vitro experiments, and the feasibility of high-resolution three dimensional (3D) T_1 and T_2 mapping is presented in vivo for human articular cartilage at 3 Tesla (T).

4.2 Methods

All numerical simulations, data analysis and visualization were done using Matlab 7.5 (The MathWorks, Inc., Natick, MA). Measurements and calibrations were performed on a clinical 1.5 T and a 3 T system equipped with actively shielded magnetic field gradient coils.

4.2.1 Triple Echo Steady State (TESS)

Multi Echo SSFP, as displayed in Figure 4.1, was already proposed by Mizumoto and Yoshitome for imaging different contrast dependencies [25]. Generally, the ideal SSFP signal (no motion, no diffusion, quasi-instantaneous RF pulses) can be written in a representation that is closely related to configuration theory [26]. Expressions for the two lowest order modes (F_0, representing the FID, and F_{-1} representing the Echo) immediately following the excitation pulse can be found e.g. in Ref. [27],

$$F_0 \propto 1 - (E_1 - \cos\alpha)\cdot r, \tag{4.1}$$

$$F_{-1} \propto (1 - (1 - E_1\cos\alpha)\cdot r)E_2^{-1} \tag{4.2}$$

with definitions

$$\begin{aligned} E_{1,2} &:= \exp(-\mathrm{TR}/T_{1,2}),\\ p &:= 1 - E_1\cos\alpha - E_2^2(E_1 - \cos\alpha),\\ q &:= E_2(1 - E_1)(1 + \cos\alpha),\\ r &:= (1 - E_2^2)(p^2 - q^2)^{-1/2}. \end{aligned}$$

All higher order modes can then be derived from F_0 and F_{-1} as

$$F_n = \begin{cases} \left(\frac{u_1}{u_0}\right)^n \cdot F_0 & for \quad n \geq 0 \\ \left(\frac{u_1}{u_0}\right)^{|n|-1} \cdot F_{-1} & for \quad n < 0 \end{cases} \tag{4.3}$$

using

$$\begin{aligned} u_0 &:= p(p^2 - q^2)^{-1/2} \quad \text{and}\\ u_1 &:= \frac{p}{q}(u_0 - 1). \end{aligned}$$

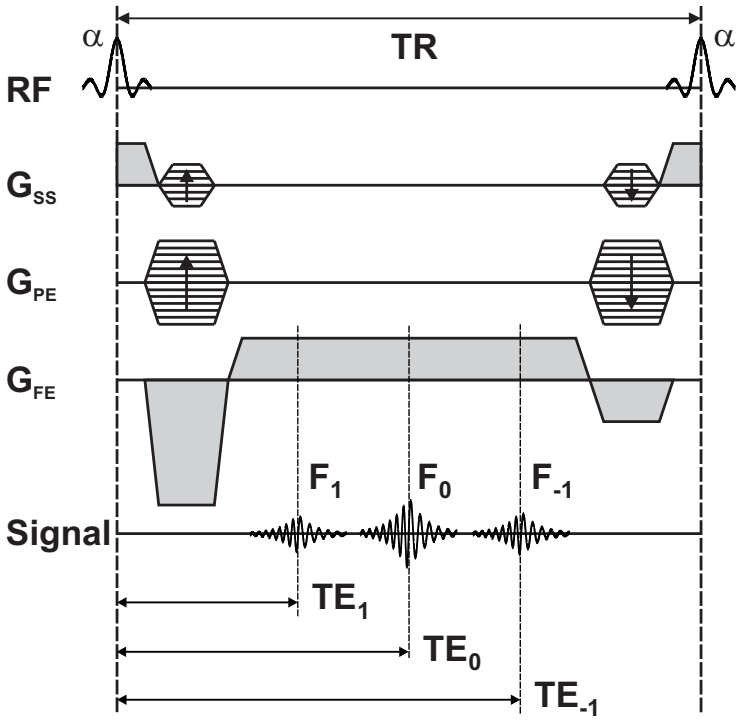

Figure 4.1: Illustration of a triple-echo steady-state (TESS) sequence. The center FID (F_0) is flanked by a higher order FID to the left (F_1) and by the lowest order Echo (F_{-1}) to the right, with echo times TE_1, TE_0, and TE_{-1}, respectively.

For the F_1 mode, we thus find

$$F_1 \propto q^{-1} \cdot \left(p - \sqrt{p^2 - q^2}\right) \cdot (1 - (E_1 - \cos\alpha) \cdot r). \tag{4.4}$$

Note that all modes F_n in Eq. (4.3) are positive by definition (in contrast to Eq. (21) given in Ref. [27], where the modes are negative for n < 0). Representative F_1, F_0, and F_{-1} steady-state signal levels for tissues and fluids are shown in Figures 4.2 a and 4.2 b as a function of the flip angle. Taking now into account that the signals are acquired with t > 0 (rather than t = 0), the signal expressions become weighted by the corresponding echo time (TE_1, TE_0, and TE_{-1}; for details, see Fig. 4.1)

$$F_{1,0,-1} \rightarrow F_{1,0,-1} \cdot \exp(-TE_{1,0,-1}/T_2). \tag{4.5}$$

For short enough TEs, a T_2 rather than a T_2^* weighting is introduced to Eqs. (4.1), (4.2), and (4.4). As reported in Ref. [28], the error arising from such an approximation is small.

4.2.2 Relaxometry with TESS

As proposed for rapid quantification of T_2 from DESS [9], we follow the initial idea of exploiting the dependencies of the modes on relaxation to quantify T_1 and T_2. To this end, we investigate the following signal ratios (see Fig. 4.3):

$$
\begin{aligned}
s_{T_2}(T_1) &:= \frac{F_1}{F_0} \quad \text{and} \\
s_{T_1}(T_2) &:= \frac{F_{-1}}{F_0 - F_1}.
\end{aligned} \tag{4.6}
$$

Here, the subscript T_2 (T_1) is used to indicate that for the ratio $s_{T_2}(T_1)$ ($s_{T_1}(T_2)$) the relaxation time T_2 (T_1) is considered to be a bound variable: formally, the signal ratios then depend for any given set of extrinsic parameters (TR, $\mathrm{TE}_{1,0,-1}$, and α) only on one running variable, namely T_1 or T_2.

From this, an easy and fast iterative procedure based on a one dimensional numerical minimization can be used for the derivation of T_1 and T_2, as described in the following: A search interval for T_1 and T_2 with a (dummy) upper guess of $T_{1,u} = T_{2,u} = 5$ s is defined. The iteration is initialized with a global estimate for the longitudinal relaxation time, $T_{1,i=0} \in [0, T_{1,u}]$, and a golden section search [29] performed to calculate an estimate for the transverse relaxation time, $T_{2,i+1}$, based on the measured signal ratio s_{T_1} (see Eq. (4.6)),

$$
T_{2,i+1} = \arg\min\{T_2 \in [0, T_{2,u}] : |s_{T_1,\mathrm{meas}} - s_{T_{1,i}}(T_2)|\}. \tag{4.7}
$$

Now, the obtained guess of $T_{2,i+1}$ is used to yield an improved $T_{1,i+1}$ estimate based on the signal ratio s_{T_2} (see Eq. (4.6)), according to

$$
T_{1,i+1} = \arg\min\{T_1 \in [0, T_{1,u}] : |s_{T_2,\mathrm{meas}} - s_{T_{2,i+1}}(T_1)|\} \tag{4.8}
$$

again using a golden section search, but now on T_1. The improved $T_{1,i+1}$ estimate can then be used again to calculate an updated $T_{2,i+2}$ estimate based on Eq. (4.7), and so on. The iteration stops as soon as the change in both T_1 and T_2 is less than a user defined convergence tolerance, i.e. 0.1 ms. While iterating, the whole search procedure becomes independent of the initial T_1 estimate. In this work, we use a consistent rough global estimate of $T_1 = 1000$ ms for all simulations, as well as in vitro and in vivo relaxometry. Even with such a rough guess, typically less than 10 iterations are required for convergence of the algorithm.

The specific choice of the signal ratios given in Eq. (4.6) is motivated as follows: Instead of the basic ratio which is used with DESS for T_2 quantification, we investigate the ratio $F_{-1}/(F_0 - F_1)$ since it shows a stronger sensitivity to T_2 (see Fig. 4.3 b where the good T_2 sensitivity of this ratio is apparent). For T_1 estimation using TESS, another independent ratio is required and we choose F_1/F_0 because of its strong sensitivity to T_1 (see Fig. 4.3 a). The investigated signal ratios necessarily have to be bijective functions of either T_1 or T_2. More precisely, $s_{T_2}(T_1)$ ($s_{T_1}(T_2)$) has to be bijective with respect to T_1 (T_2) which holds for our choice. Otherwise the minimization might run into local rather than global minima.

4.2.3 Simulations

Optimal signal-to-noise ratio (SNR) is not only achieved at different flip angles for different modes, but also depends on relaxation times (see Figs. 4.2 a and 4.2 b). We

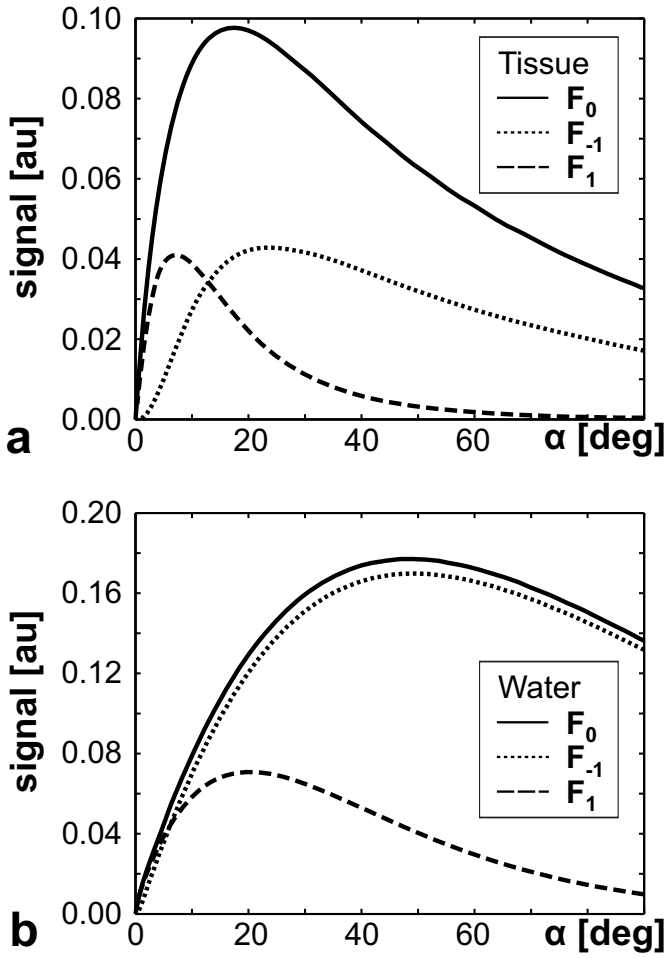

Figure 4.2: (Simulated TESS signals for tissues (a) and water (b) as a function of the flip angle α. Simulation parameters: TR = 16 ms, $TE_1 = TE_0 \rightarrow 0$, and $TE_{-1} \rightarrow$ TR, tissues: T_1 / T_2 = 1000 ms / 50 ms, water: T_1 / T_2 = 3000 ms / 1000 ms.

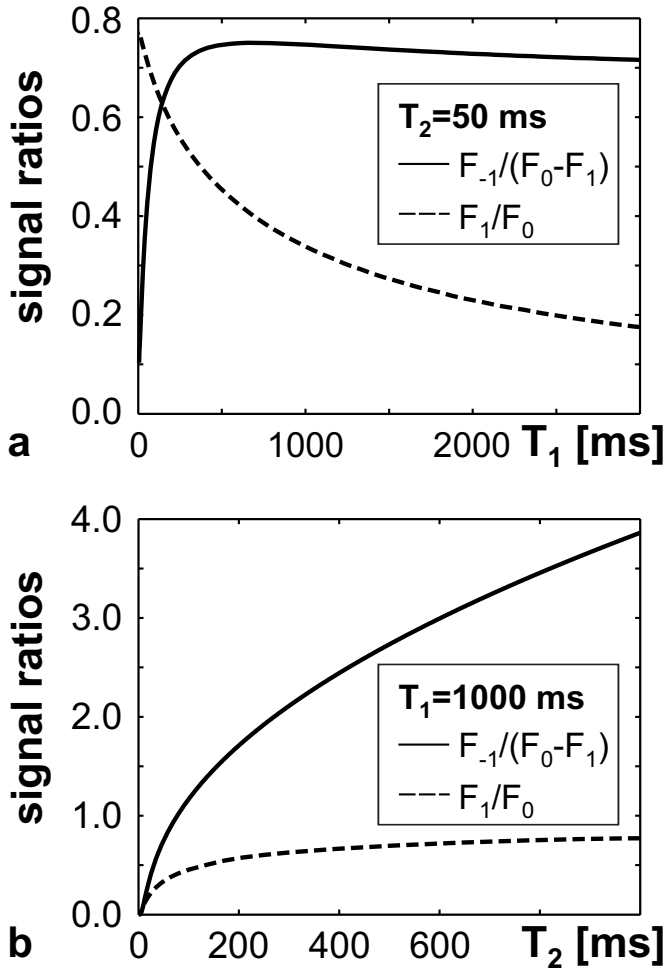

Figure 4.3: Simulation of relevant signal ratios (s_{T_1}, s_{T_2}) according to Eq. (4.6) using a flip angle of 15°, derived from the three base modes, as acquired with TESS (see Fig. 4.1). (a) Signal ratios as a function of T_1 for a fixed T_2 of 50 ms. Only the F_1/F_0 signal ratio shows a bijective behavior and a good sensitivity for $T_2 \ll T_1$. (b) Signal ratios as a function of T_2 for a fixed T_1 of 1000 ms. Only the $F_{-1}/(F_0 - F_1)$ signal ratio is sensitive to the limit of $T_2/T_1 \to 1$.

aim at finding optimal flip angle settings for TESS-based relaxometry and analyze the impact of noise on the T_1 and T_2 calculation. To this end, a Monte-Carlo simulation is performed for a range of idealized homogeneous T_2/T_1-probes with signal amplitudes according to Eqs. (4.1)-(4.5). Optimal flip angle settings are explored based on 100'000 $F_{1,0,-1}$ drawings with mean zero and 0.001 M_0 standard deviation. The value of the standard deviation directly relates to the amount of noise in the acquired MR images. From the sample of noisy signal amplitudes, distributions of $T_{1,2}$ with mean $< T_{1,2} >$ and standard deviation $\Delta T_{1,2}$ are calculated based on Eqs. (4.6)-(4.8). The SNR for relaxation time mapping using TESS can then be estimated from $\mathrm{SNR}_{T_1,T_2} := < T_{1,2} > / \Delta T_{1,2}$. Relative SNR is evaluated according to $\mathrm{rSNR}_{T_1,T_2} := \mathrm{SNR}_{T_1,T_2} / \max\{\mathrm{SNR}_{T_1}, \mathrm{SNR}_{T_2}\}$ for flip angles ranging from 5° to 40° and for T_2/T_1 ratios ranging from 0.01 to 1.0, using logarithmically spaced T_2 values between 10 ms and 1000 ms, but a fixed T_1 of 1000 ms.

4.2.4 Measurements

A contemporary DESS sequence was adapted for the acquisition of F_1, F_0, and F_{-1} within every TR, as displayed in Figure 4.1. Generally, although not limited to, the same bandwidth was used for the acquisition of all echoes. To provide enough SNR in the base data for T_1 and T_2 calculation, some averages of the TESS scan were taken as specified below.

In vitro relaxation time mapping with TESS was performed at 1.5 T on manganese-doped spherical phantoms (0 mM, 0.05 mM, 0.125 mM, 0.25 mM, 0.5 mM $MnCl_2$ in H_2O) of about 14 cm in diameter. Longitudinal relaxation was assessed from single-slice inversion recovery (IR) turbo spin-echo (TSE) experiments with inversion times (TI) ranging between 25 ms and 9.6 s. For a single IR-TSE scan with 2.5 × 2.5 mm^2 in-plane resolution (128 × 64 matrix) and 5 mm slice thickness, using a turbo factor of 7, a TR of 10 s, a TE of 12 ms, and a bandwidth of 130 Hz/pixel, image acquisition was completed within 1 min 22 s. Transverse relaxation was measured from a contemporary single-echo SE method with a TE ranging from 5 ms up to 3.2 s. One single scan was completed within 3 min 18 s, yielding 2.5 × 5.0 mm^2 in-plane resolution (128 × 32 matrix) and 5 mm slice thickness, using a turbo factor of 1, a TR of 6 s, and a bandwidth of 592 Hz/pixel. A single-echo rather than a multi-echo approach was used to avoid any possible bias in T_2 from stimulated echo contributions [30]. TESS imaging was performed in 3D with 4 mm isotropic resolution (64 × 64 × 44 matrix). Scans were performed with a nominal flip angle of 40° and a constant bandwidth of 240 Hz/pixel for all three echoes, yielding an overall TR of 15.7 ms with corresponding echo times TE_1 = 3.6 ms, TE_0 = 8.0 ms, and TE_{-1} = 12.4 ms. Four averages were taken and the 3D TESS scan was completed within 2 min and 58 s.

In vivo human knee scans at 3 T of two healthy volunteers were performed with 3D TESS in axial and sagittal orientation (the slab consisted of 12 slices with 3 mm resolution) using a dedicated 15-channel transmit and receive knee coil (QED) yielding 0.6 × 0.6 mm^2 in-plane resolution (256 × 232 × 18 image encoding matrix). Imaging was performed with water-selective excitation pulses ($1\bar{2}1$-binomials) of nominal 15° flip angle. The bandwidth was set to 230 Hz/pixel, yielding a TR of 20.6 ms and corresponding echo times TE_1 = 6.6 ms, TE_0 = 11.0 ms, and TE_{-1} = 15.4 ms.

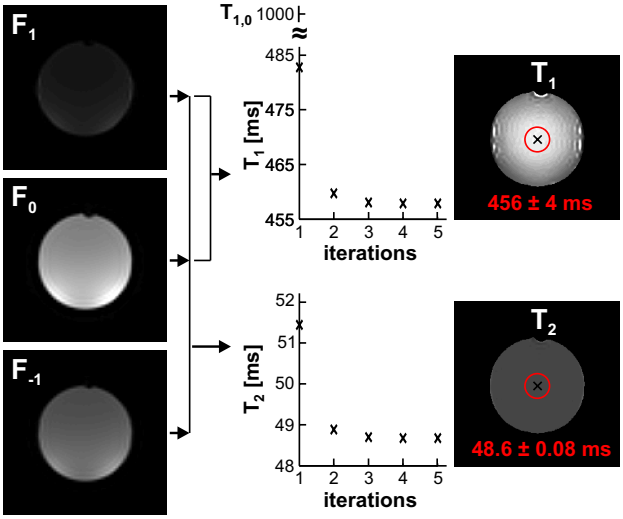

Figure 4.4: Illustration of iterative relaxometry calculations from F_1, F_0, and F_{-1} base images, as presented in Eqs. (4.7) and (4.8). The iteration is exemplarily shown for a pixel in the center of the phantom (black cross). Based on the s_{T_1} signal ratio (with an initial guess of $T_{1,0} = 1$ s), a guess of $T_{2,1} \sim 51.5$ ms is derived from Eq. (4.7) using a golden section search. This first guess of T_2 is then used to find an updated estimate of $T_{1,1} \sim 483$ ms based on Eq. (4.8), again using a golden section search. This procedure is repeated until the change in both T_1 and T_2 falls below a certain threshold (here, 0.1 ms); typically, requiring less than 10 iterations. Relaxation parameters were assessed for a region of interest, as indicated in the relaxation maps by the circle.

Seven averages were taken. The 3D TESS scan was completed within 4 min and 24 s. Reference T_1 values were calculated from six consecutive IR-TSE scans (12 slices, 0.3 mm gap, 2.7 mm slice thickness, 0.6 × 0.6 mm^2 in-plane resolution using a 256 × 232 matrix, turbo factor 8, a TR of 6 s, a TE of 10 ms, and a bandwidth of 227 Hz/pixel) with inversion times ranging between 25 ms and 2.35 s. A single scan took 1 min 44 s to complete. Reference T_2 values were derived based on nine consecutive single-echo SE scans (12 slices, no gap, 3 mm slice thickness, 0.6 × 0.6 mm^2 in-plane resolution using a 256 × 232 matrix, turbo factor 1, a TR of 1210 ms, and a bandwidth of 227 Hz/pixel) with corresponding echo times of 10, 20, 30,..., 90 ms. One single-echo SE scan was completed within 2 min 39 s. For comparison, a multi-echo spin-echo approach (nine echoes: starting from 10 ms, and having an echo spacing of 10 ms) was also used with identical settings as the single-echo scan.

4.3 Results

Relaxometry based on TESS is exemplarily illustrated in Fig. 4.4 at 1.5 T for one of the manganese-doped spherical probes (0.25 mM $MnCl_2$ in H_2O) with a nominal T_1 of 456 ms and a nominal T_2 of 48.5 ms, derived by spin-echo techniques (see Section 'Methods' for details) and regarded in the following as gold standard [31]. From a

Table 4.1: In vitro comparison of single-echo spin-echo and TESS relaxometry data (T_1 and T_2) on manganese-doped aqueous probes at 1.5 T (for protocol details, see Section 'Methods').

[$MnCl_2$]	TESS	IR-SE	TESS	SE
	T_1 [ms]	T_1 [ms]	T_2 [ms]	T_2 [ms]
0.000 mM	3208 ± 126	2995 ± 2	2082 ± 79	1903 ± 7
0.050 mM	1481 ± 12	1485 ± 2	240 ± 1.0	241 ± 1.1
0.125 mM	871 ± 10	858 ± 1	104.0 ± 0.27	104.7 ± 0.28
0.250 mM	456 ± 4	456 ± 1	48.6 ± 0.08	48.5 ± 0.17
0.500 mM	263 ± 2	272 ± 1	27.0 ± 0.02	27.0 ± 0.11

single 3D TESS scan, three different sets of images are acquired (see also Fig. 4.1) with formal descriptions as stated in Eqs. (4.1)-(4.5). From the s_{T_1} signal ratio (see Eq. (4.6)), an estimated T_2 value is found (using Eq. (4.7), and an initial estimate of $T_{1,0} = 1$ s). The obtained value is then used to calculate an updated estimate of T_1, based on s_{T_2} (see Eqs. (4.6) and (4.8)). This procedure is repeated until the iterative change in T_1 and T_2 falls below a certain threshold (here, 0.1 ms). Typically, the iterative procedure converges very quickly (see Fig. 4.4). The resulting T_1 and T_2 maps are also shown in Figure 4.4, with the relaxometry results summarized in Table 4.1 for all probes (evaluated for a circular region of interest, ROI, placed in the center of the phantoms as indicated in Fig. 4.4). Generally, excellent agreement is found between reference single-echo SE and TESS transverse relaxometry data. However, some variation is observed for T_1 using TESS. Interestingly, no spatial variation can be seen for T_2 whereas T_1 decreases by about 20 % towards the rim of the phantom.

The spatial variation of T_1, as observed in vitro (see Fig. 4.4), is likely to be due to B_1 field heterogeneities and thus related to a miscalibration between the nominal (α_{nom}) and the actual flip angle (α_{act}) in the probes. This is confirmed by rerunning the calculation, but this time assuming a halved excitation angle, that is with $\alpha_{\text{nom}} = 20°$, instead of $\alpha_{\text{nom}} = 40°$. As a result, a strongly falsified T_1 is observed (see Fig. 4.5 a), however, T_2 proves to be completely inert. The sensitivity to transmit field errors, $\Delta\alpha := (\alpha_{\text{act}} - \alpha_{\text{nom}})/\alpha_{\text{nom}}$, is now systematically evaluated, as exemplarily demonstrated in Figure 4.5 b for $\alpha_{\text{nom}} = 40°$ and T_1 / T_2 / TR = 456 ms / 48.5 ms / 16 ms. The B_1 sensitivity of T_1, $\Delta T_1/\Delta\alpha$, is about 2, but $\Delta T_2/\Delta\alpha$ is barely noticeable, where $\Delta T_{1,2} := (T_{1,2}(\alpha_{\text{act}}) - T_{1,2}(\alpha_{\text{nom}}))/T_{1,2}(\alpha_{\text{nom}})$. This surprising result is not a remarkable coincidence related to a lucky choice of relaxation and sequence parameters, but can be confirmed over a large range of relaxation parameters and flip angles (Fig. 4.5 c). TESS thus offers a unique opportunity for fast, accurate, and unbiased T_2 quantification, whereas T_1 estimates show the expected typical prominent sensitivity of contemporary steady-state methods to B_1 field errors, requiring corrective data. The atypical behavior of TESS-T_2 is of special advantage and benefit in vivo.

For high-resolution in vivo TESS relaxometry, SNR is expected to become critical and propagation of noise must be evaluated. Corresponding simulation results are

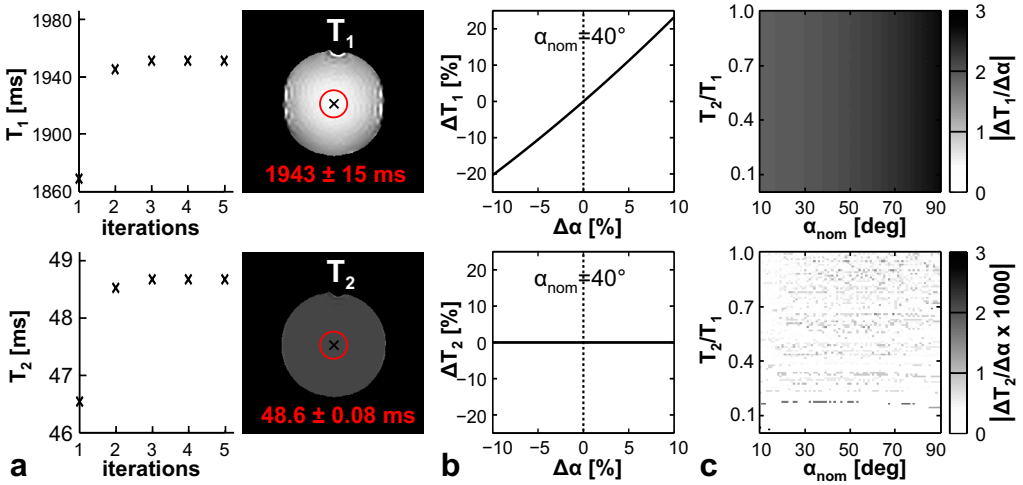

Figure 4.5: (a) Recalculation of T_1 and T_2, as presented in Figure 4.4, but using only half of the nominal flip angle for the calculation, i.e. 20°, instead of 40°. As a result of the dramatic underestimation of the actual flip angle by 50 %, T_1 is considerably overestimated (1943 ms, instead of 456 ms), but exactly the same value is derived for T_2. (b) B_1 sensitivity of T_1 (top) and T_2 (bottom) simulated for the flip angle and relaxation times of the phantom shown in (a). (c) Simulated B_1 sensitivity, as shown in (b), over a complete range of flip angles and T_2/T_1 times. Note the different scales in the sensitivity maps for T_1 and T_2.

shown in Figure 4.6. The expected relative SNR (rSNR) for T_1 (Fig. 4.6 a) and T_2 (Fig. 4.6 b) mapping using TESS is strongly affected by the choice of the flip angle (as might already be expected from the corresponding signal curves, see Figs. 4.2 a and 4.2 b). Generally, a pronounced rSNR maximum can be observed in both T_1 and T_2 near $\alpha \sim 15°$ with respect to a $T_2/T_1 \sim 0.05$ 0.1, that is for tissues. As a result, optimal SNR for TESS-based relaxometry can be achieved in the low flip angle and low T_2/T_1 limit.

High-resolution in vivo 3D TESS relaxometry is demonstrated in the knee joint at 3 T in axial (Fig. 4.7) and sagittal (Fig. 4.8) slice orientation using optimal flip angles for tissues. As an internal control, three small test tubes containing 0.125 mM, 0.25 mM, and 0.5 mM $MnCl_2$ were placed adjacent to the knee for the axial scan. B_1-insensitive TESS-T_2 quantification is illustrated in Fig. 4.7 and compared to reference T_2 maps calculated based on single-echo and multi-echo spin-echo experiments. Transverse relaxation time values are assessed for selected regions of interest (for definition of ROIs, see Fig. 4.7) with corresponding results summarized in Table 4.2. Overall, excellent correspondence between TESS and single-echo spin-echo transverse relaxometry data is found, whereas T_2 values, derived from multi-echo spin-echo data, show a pronounced overestimation of about 30 – 40 % for cartilage, muscle, and for the internal controls due to stimulated echo contributions (from imperfect refocusing pulses and thus due to B_1 errors).

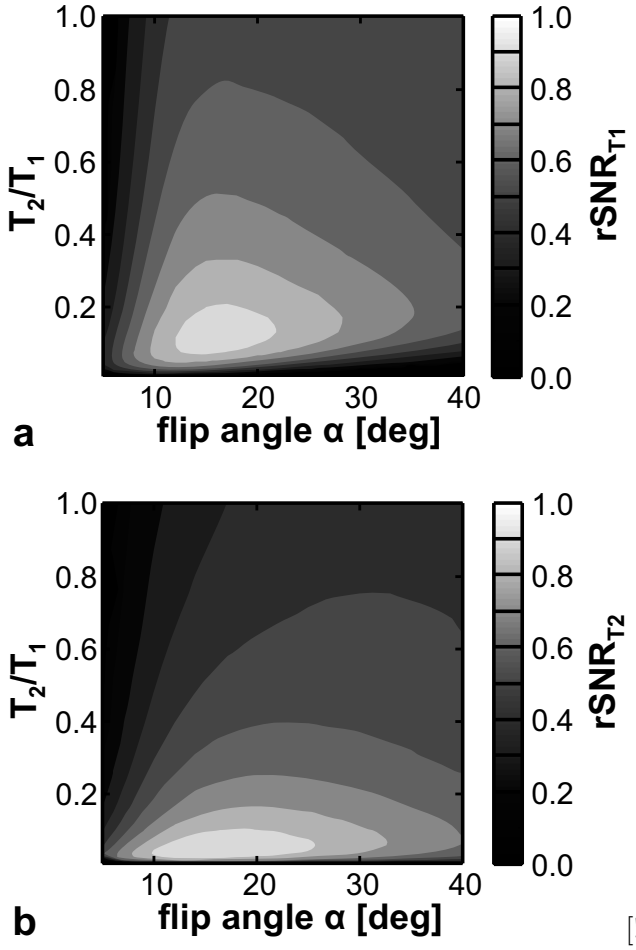

[!ht]

Figure 4.6: Monte-Carlo simulation of the relative signal-to-noise ratio (rSNR) for TESS relaxometry as a function of the flip angle and relaxation times (T_2 = 10 – 1000 ms, T_1 = 1000 ms) for a TR of 16 ms (for simulation details, see Section 'Methods'). (a) Relative SNR for T_1 mapping. (b) Relative SNR for T_2 mapping.

The distinct B_1 insensitivity of TESS-T_2 becomes especially apparent in the sagittal T_2 scan (Fig. 4.8 b) where no variation in muscle-T_2 can be observed over the complete field-of-view (FOV). This is quite contrary to the corresponding TESS-T_1 map (Fig. 4.8 c, right): It appears more inhomogeneous and shows clearly visible variations in muscle-T_1 over the FOV originating from B_1 heterogeneities. Comparison of TESS-T_1 with a reference measurement based on six consecutive IR-TSE scans (Fig. 4.8 c, left) reveals that the T_1 map calculated with TESS is flawed as expected. However, good correspondence can be observed in regions where B_1 field errors are not that prominent, for instance in the patella: There, TESS relaxometry yields a T_1 of 869 ± 45 ms for the ROI indicated by the arrow in Fig. 4.8 c compared to a T_1 of 839 ± 40 ms obtained with IR-TSE.

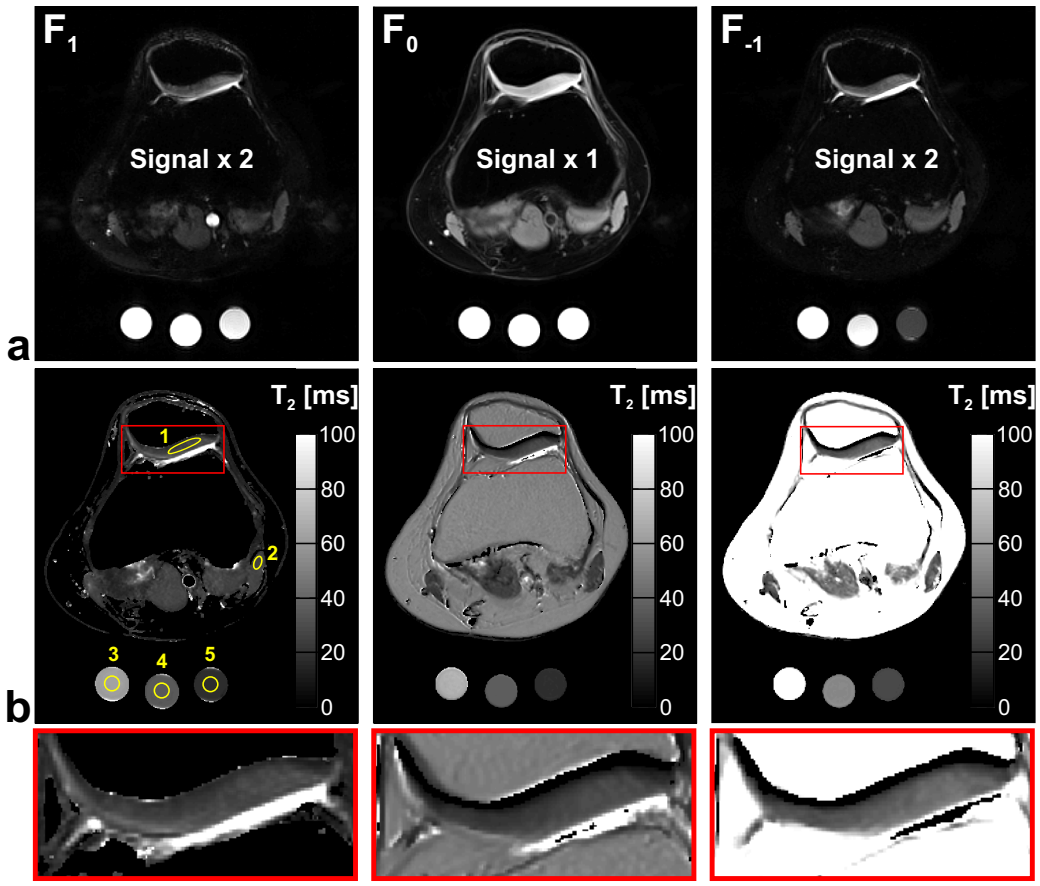

Figure 4.7: (a) Exemplary axial TESS base images (F_1, F_0, and F_{-1}) of the knee joint at 3 T obtained with water-selective excitation pulses. For better visibility, the signals corresponding to the F_1 and F_{-1} mode were multiplied by a factor of two. (b) T_2 values derived either by TESS (left), or by using a single-echo SE approach (middle), or by using a multi-echo SE method (right). The manganese-doped test tubes (0.125 mM, 0.25 mM, and 0.5 mM) serve as internal controls. For selected ROIs (indicated by the yellow numbers), T_2 values are summarized in Table 4.2. Again, excellent correspondence is observed in T_2 between TESS and single-echo SE data (see also Table 4.1), whereas the multi-echo SE approach shows a clear overestimation of T_2 from stimulated echo contributions.

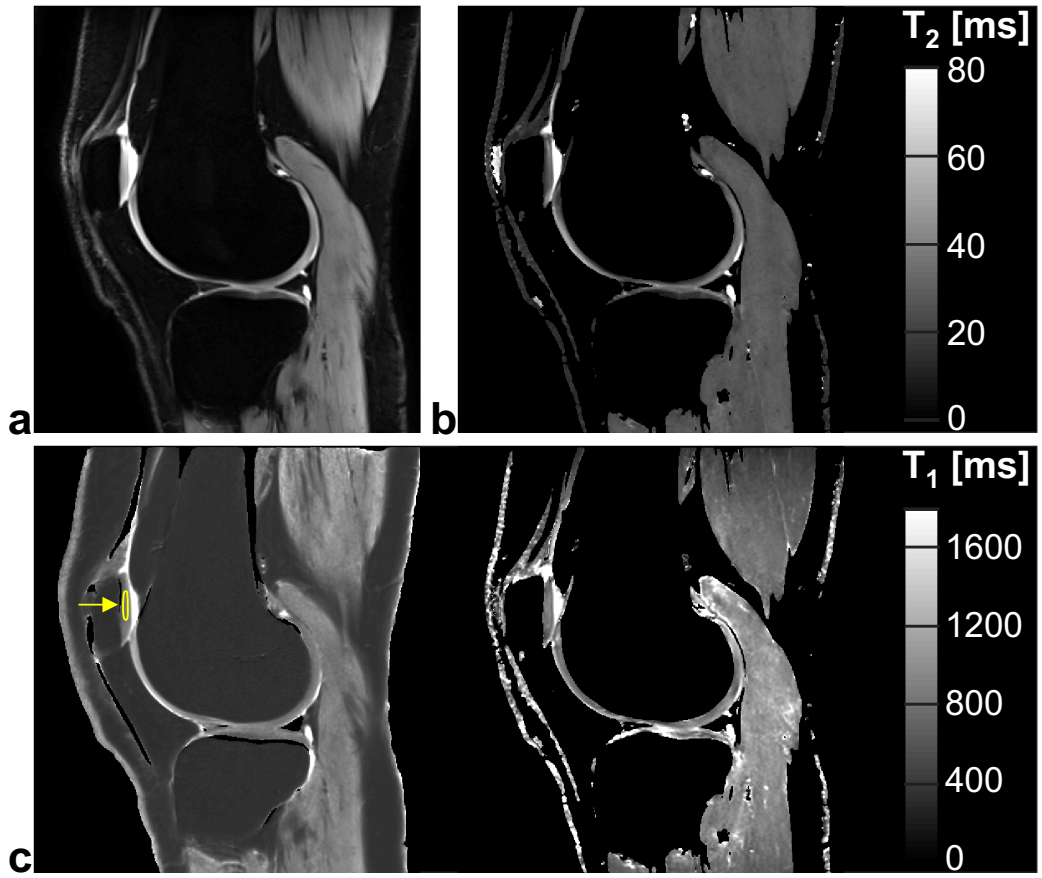

Figure 4.8: (a) Morphological TESS image, calculated from a weighted combination of the F_0 and F_{-1} signal (F_0+3·F_{-1}) to accentuate the contrast between synovial fluid and cartilage, similar to DESS. (b) B_1-insensitive sagittal T_2 map calculated from a single TESS scan. (c) Sagittal TESS-T_1 map (right) is compared to a reference T_1 measurement derived from 2D multi-slice IR-TSE scans. TESS-T_1 is clearly affected by B_1, however, good correspondence to the IR-TSE technique can be observed for instance in the patella (ROI indicated by the arrow).

Table 4.2: In vivo comparison of spin-echo and TESS T_2 relaxometry data in the knee joint at 3 T (for protocol details, see Section 'Methods').

Tissue / [$MnCl_2$]	TESS	SE[a]	SE[b]	SE[c]
		Single-echo	Multi-echo	Multi-echo
	T_2 [ms]	T_2 [ms]	T_2 [ms]	T_2 [ms]
Cartilage[d]	27.3 ± 3.2	26.5 ± 3.2	32.9 ± 4.5	40.4 ± 5.2
Muscle[e]	26.3 ± 0.6	24.6 ± 1.1	31.1 ± 4.5	37.6 ± 4.9
0.125 mM[f]	64.2 ± 0.9	69.1 ± 0.6	84.0 ± 0.6	102.6 ± 0.7
0.250 mM[g]	34.9 ± 0.3	36.6 ± 0.1	44.4 ± 0.2	53.0 ± 0.3
0.500 mM[h]	18.0 ± 0.2	18.7 ± 0.1	23.0 ± 0.1	28.9 ± 0.1

[a] T_2 value derived based on nine single-echo SE scans using a nonlinear least-squares fit.
[b] T_2 value derived based on a multi-echo SE scan (nine echoes), using a nonlinear least-squares fit. For the fit, the first echo was discarded to mitigate stimulated echo contributions.
[c] T_2 value derived based on a multi-echo SE scan (nine echoes), using a nonlinear least-squares fit.
[d] For definition, see Fig. 4.7: ROI 1.
[e] For definition, see Fig. 4.7: ROI 2.
[f] For definition, see Fig. 4.7: ROI 3.
[g] For definition, see Fig. 4.7: ROI 4.
[h] For definition, see Fig. 4.7: ROI 5.

4.4 Discussion

A variety of SSFP methods have been proposed thus far and are known in the literature for fast relaxometry, but all of them are sensitive to B_1 and show some more or less pronounced mixed T_2/T_1 sensitivity that can be mitigated by companion scans. As a result, without the use of additional corrective data, current SSFP techniques fail to deliver accurate, reliable and stable quantification results.

In this work, we report on a similar approach, as proposed for rapid T_2 quantification of cartilage using double-echo steady-state (DESS) imaging [28, 32]. In the limit of $\alpha \sim 90°$, the ratio between the F_{-1} and F_0 signal, as acquired with DESS, becomes independent of T_1, allowing accurate quantification of T_2 [9]. Signal-to-noise, however, is especially poor in this limit, requiring considerably lower flip angles in practice and hence leading to a systematic T_1-related bias in the estimated T_2 values using DESS. In principle, we solve this issue by acquiring a third independent mode, namely F_1. Based on two independent signal ratios, the interacting T_1- and T_2 sensitivity can be tackled by a simple and fast ping-pong approach, using a golden section search, until the calculated signal ratios converge to the actual measured ones. As a result, TESS offers the possibility of acquiring both T_1 and T_2 within one single scan and without the confounding influence of either T_1 on T_2 or T_2 on T_1 (as observed with any other steady-state method). Moreover, from the application of spoiler gradients within every TR, TESS is not affected by static field inhomogeneities. However, some motion sensitivity must be taken into account. Therefore, proper fixation seemed mandatory and was carefully conducted prior to every measurement. Diffusion effects are ex-

pected to be negligible for tissues, but reduce the signal of fluids for high-resolution scans [33].

As with any other fast quantitative SSFP imaging technique, TESS-based relaxometry is expected to be affected by B_1 field heterogeneities, and the impact of such transmit field calibration errors on T_1 and T_2 quantification was analyzed in Figure 4.5. Surprisingly, T_2 relaxometry with TESS revealed to be independent of B_1 whereas T_1 quantification showed the expected pronounced B_1-related estimation errors. This extraordinary feature is not only of special interest for high to ultra-high field T_2 relaxometry where prominent B_1 variations can be expected and applicability of spin-echo techniques might be limited due to SAR constraints, but also provides accurate quantification results in combination with spectral-spatial excitation pulses that typically entail flip angle calibration errors in the presence of B_0 heterogeneities. Spectral-spatial excitation, as demonstrated in Figures 4.7 and 4.8 for TESS, is especially beneficial for musculoskeletal imaging where fat is often found adjacent or interspersed within the tissues of interest. Fat suppression may thus not only enhance diagnostic information [34], but also eliminates the chemical shift artifact and thereby allows readout of the SSFP signal modes with a reduced receiver bandwidth which in turn results in an overall increased SNR.

4.5 Conclusions

In contrast to all other existing SSFP quantification techniques, TESS offers rapid T_1 and T_2 estimation within one single scan. Moreover, quantification of T_2 with TESS is markedly insensitive to B_1. As a result, the new proposed method is of high interest for fast and reliable relaxometry in the clinical routine, especially for rapid and bias-free T_2 imaging of the musculoskeletal system at high to ultra-high field strength.

References

[1] H. Y. Carr. Steady-state free precession in nuclear magnetic resonance. *Phys Rev*, 112(5):1693–1701, 1958.

[2] M. A. Bernstein, K. F. King, and X. J. Zhou. *Handbook of MRI Pulse Sequences*. Elsevier Academic Press, 2004.

[3] D. C. Look and D. R. Locker. Time saving in measurement of NMR and EPR relaxation times. *Rev Sci Instrum*, 41:250–251, 1970.

[4] K. A. Christensen, D. M. Grand, E. M. Schulman, and C. Walling. Optimal determination of relaxation times of Fourier transform nuclear magnetic resonance. Determination of spin-lattice relaxation times in chemically polarized species. *J Phys Chem*, 78:1971–1977, 1974.

[5] J. Homer and M. S. Beevers. Driven-equilibrium single-pulse observation of T1 relaxation. A reevaluation of a rapid "new" method for determining NMR spin-lattice relaxation times. *J Magn Reson*, 63(2):287–297, 1985.

[6] K. Scheffler and J. Hennig. T(1) quantification with inversion recovery TrueFISP. *Magn Reson Med*, 45(4):720–3, 2001.

[7] S. C. Deoni, B. K. Rutt, and T. M. Peters. Rapid combined T1 and T2 mapping using gradient recalled acquisition in the steady state. *Magn Reson Med*, 49(3): 515–26, 2003.

[8] P. Schmitt, M. A. Griswold, P. M. Jakob, M. Kotas, V. Gulani, M. Flentje, and A. Haase. Inversion recovery TrueFISP: quantification of T(1), T(2), and spin density. *Magn Reson Med*, 51(4):661–7, 2004.

[9] G. H. Welsch, K. Scheffler, T. C. Mamisch, T. Hughes, S. Millington, M. Deimling, and S. Trattnig. Rapid estimation of cartilage T2 based on double echo at steady state (DESS) with 3 Tesla. *Magn Reson Med*, 62(2):544–9, 2009.

[10] O. Bieri, K. Scheffler, G. H. Welsch, S. Trattnig, T. C. Mamisch, and C. Ganter. Quantitative mapping of T2 using partial spoiling. *Magn Reson Med*, 66(2): 410–8, 2011.

[11] K. L. Miller, B. A. Hargreaves, G. E. Gold, and J. M. Pauly. Steady-state diffusion-weighted imaging of in vivo knee cartilage. *Magn Reson Med*, 51(2): 394–8, 2004.

[12] S. C. Deoni, T. M. Peters, and B. K. Rutt. Quantitative diffusion imaging with steady-state free precession. *Magn Reson Med*, 51(2):428–33, 2004.

[13] O. Bieri, C. Ganter, G. H. Welsch, S. Trattnig, T. C. Mamisch, and K. Scheffler. Fast diffusion-weighted steady state free precession imaging of in vivo knee cartilage. *Magn Reson Med*, 67(3):691–700, 2012.

[14] O. Bieri, C. Ganter, and K. Scheffler. Quantitative in vivo diffusion imaging of cartilage using double echo steady-state free precession. *Magn Reson Med*, 68(3): 720–729, 2012.

[15] E. Staroswiecki, K. L. Granlund, M. T. Alley, G. E. Gold, and B. A. Hargreaves. Simultaneous estimation of T(2) and apparent diffusion coefficient in human articular cartilage in vivo with a modified three-dimensional double echo steady state (DESS) sequence at 3 T. *Magn Reson Med*, 67(4):1086–96, 2012.

[16] O. Bieri, T. C. Mamisch, S. Trattnig, and K. Scheffler. Steady state free precession magnetization transfer imaging. *Magn Reson Med*, 60(5):1261–6, 2008.

[17] M. Gloor, K. Scheffler, and O. Bieri. Quantitative magnetization transfer imaging using balanced SSFP. *Magn Reson Med*, 60(3):691–700, 2008.

[18] M. Gloor, K. Scheffler, and O. Bieri. Nonbalanced SSFP-based quantitative magnetization transfer imaging. *Magn Reson Med*, 64(1):149–56, 2010.

[19] M. Markl, M. T. Alley, C. J. Elkins, and N. J. Pelc. Flow effects in balanced steady state free precession imaging. *Magn Reson Med*, 50(5):892–903, 2003.

[20] F. Santini, S. G. Wetzel, J. Bock, M. Markl, and K. Scheffler. Time-resolved three-dimensional (3D) phase-contrast (PC) balanced steady-state free precession (bSSFP). *Magn Reson Med*, 62(4):966–74, 2009.

[21] A. F. Stalder, M. F. Russe, A. Frydrychowicz, J. Bock, J. Hennig, and M. Markl. Quantitative 2D and 3D phase contrast MRI: optimized analysis of blood flow and vessel wall parameters. *Magn Reson Med*, 60(5):1218–31, 2008.

[22] V. L. Yarnykh. Optimal radiofrequency and gradient spoiling for improved accuracy of T1 and B1 measurements using fast steady-state techniques. *Magn Reson Med*, 63(6):1610–26, 2010.

[23] S. C. Deoni, T. M. Peters, and B. K. Rutt. High-resolution T1 and T2 mapping of the brain in a clinically acceptable time with DESPOT1 and DESPOT2. *Magn Reson Med*, 53(1):237–41, 2005.

[24] S. C. Deoni, H. A. Ward, T. M. Peters, and B. K. Rutt. Rapid T2 estimation with phase-cycled variable nutation steady-state free precession. *Magn Reson Med*, 52 (2):435–9, 2004.

[25] C. T. Mizumoto and E. Yoshitome. Multiple echo SSFP sequences. *Magn Reson Med*, 18(1):244–250, 1991.

[26] M. T. Vlaardingerbroek and J. A. den Boer. *Magnetic Resonance Imaging*, pages 423–67. Springer-Verlag, Berlin, 3rd edition, 2003.

[27] W. Hänicke and H. U. Vogel. An analytical solution for the SSFP signal in MRI. *Magn Reson Med*, 49(4):771–5, 2003.

[28] H. Bruder, H. Fischer, R. Graumann, and M. Deimling. A new steady-state imaging sequence for simultaneous acquisition of two MR images with clearly different contrasts. *Magn Reson Med*, 7(1):35–42, 1988.

[29] W. H. Press, S. A. Teukolsky, W. T. Vetterling, and B. P. Flannery. *Numerical Recipes: The Art of Scientific Computing*. Cambridge University Press, Cambridge, 2007.

[30] R. M. Lebel and A. H. Wilman. Transverse relaxometry with stimulated echo compensation. *Magn Reson Med*, 64(4):1005–14, 2010.

[31] S. Meiboom and D. Gill. Modified spin-echo method for measuring nuclear relaxation times. *Rev Sci Instrum*, 29:688–691, 1958.

[32] T. W. Redpath and R. A. Jones. FADE–A new fast imaging sequence. *Magn Reson Med*, 6(2):224–234, 1988.

[33] O. Bieri, C. Ganter, and K. Scheffler. On the fluid-tissue contrast behavior of high-resolution steady-state sequences. *Magn Reson Med*, 68(5):1586–92, 2012.

[34] P. A. Hardy, M. P. Recht, and D. W. Piraino. Fat suppressed MRI of articular cartilage with a spatial-spectral excitation pulse. *J Magn Reson Imaging*, 8(6): 1279–87, 1998.

Chapter 5

Triple-echo steady-state T_2 relaxometry of the human brain at high to ultra-high fields

A modified version of this chapter has been published as:
Heule R, Bär P, Mirkes C, Scheffler K, Trattnig S, Bieri O. Triple-echo steady-state T_2 relaxometry of the human brain at high to ultra-high fields. NMR Biomed, 27(9):1037-1045, 2014.

5.1 Introduction

Relaxation is one of the most fundamental fingerprints of NMR reflecting the properties of biological tissues at a submicroscopic level. Damadian [1] was the first to report that normal and pathological tissues can be distinguished by NMR-based relaxation time measurements. Quantitative relaxometry of biological tissues has gained paramount interest ever since and shown potential to fundamentally advance the diagnostic power of MRI, especially in the field of clinical neurosciences [2].

Relaxation time mapping in the human brain not only allows distinction between gray matter, white matter, cerebrospinal fluid (CSF) or subcutaneous fat, relaxation time alterations are also reflective of many common disease states as observed in the context of epilepsy [3], schizophrenia [4] or multiple sclerosis [5]. More recent findings suggest that T_2 relaxometry is discriminative in the assessment of patients with multiple sclerosis as it was able to detect changes in the cerebral normal-appearing white matter [6] and to quantify the disease impact in early stages [7].

Quantitative imaging, however, is limited by prohibitive scan time requirements for daily clinical routine. This has motivated the development of rapid relaxometry methods [8–16], e.g. based on multi-echo spin echo (SE) [17–19] or steady-state free precession (SSFP) [20]. The speed of these techniques comes, however, at the expense of increased sensitivity to several instrumental factors that have been identified over the years and may adversely affect the reliability of the assessed metric, i.e., its reproducibility and accuracy.

First and foremost, inhomogeneities in the transmit field (B_1) and hence a nonuniform flip angle distribution lead to an overestimation of T_2 for fast SE-based sequences due to stimulated echo contributions [21, 22], whereas SSFP relaxometry techniques generally include the nominal flip angle value directly into relaxation time calculation and thus become biased by any deviation between the nominal and actual flip angle [23]. At high to ultra-high fields, B_1 field variations can be substantial and corrective techniques are required for accurate relaxometry which, however, prolong imaging time [24–28].

Besides B_1, also heterogeneities in the static field (B_0) may impair T_2 relaxometry data. In multi-echo SE, the presence of B_0 field variations leads to imperfect refocusing pulses and consequently incomplete phase reversals thus introducing an error into T_2 measurements [29]. Balanced SSFP, on the other hand, suffers from banding artifacts related to off-resonance effects caused by B_0 inhomogeneities [30, 31]. With SSFP, B_0 sensitivity can be mitigated by employing nonbalanced techniques that use spoiler gradients, but on the cost of increased motion sensitivity [32].

Only recently, a 3D nonbalanced SSFP sequence acquiring three echoes in one single scan has been proposed for fast quantification of both, T_1 and T_2 relaxation times that is, however, because of its motion sensitivity restricted to rigid targets such as the knee [33]. As reported by the authors, this triple-echo steady-state (TESS) approach exhibits an interesting intrinsic feature: in contrast to all known fast relaxometry methods, its T_2 quantification revealed to be highly insensitive to B_1 field variations. Moreover, the low flip angles used with TESS imaging reduce RF power deposition in human tissues and hence decrease the specific absorption rate (SAR) that, in general, increases considerably with field strength [34]. Because of these characteristics

(i.e. robustness to B_0 and B_1 inhomogeneity, and low SAR) TESS appears to be ideally suited for high-resolution T_2 mapping at high up to ultra-high magnetic field strengths.

At ultra-high field (UHF), the enhanced signal-to-noise ratio (SNR) is generally invested into visualization of finer structures, and clinical benefits are likely to be achieved [34, 35]. In neuroimaging, UHF MRI has already demonstrated potential advantages for clinical diagnostics, e.g. in the depiction of cortical lesions in multiple sclerosis patients [36–38]. Reliable quantitative MRI techniques are, however, still lacking at ultra-high field strengths due to the occurrence of severe B_0 and B_1 field inhomogeneities and due to SAR limitations.

In this work, a rapid 2D imaging technique is investigated for robust TESS-based T_2 relaxometry in the human brain at high to ultra-high field strengths. 3D TESS imaging is hardly applicable to the brain where pulsating cerebrospinal fluids with long T_2 times in the order of seconds at high fields produce motion artifacts and suffer from signal loss [32]. Here, we demonstrate that rapid high resolution 2D TESS-T_2 relaxometry is reliable in the human brain at high (3 Tesla (T)) to ultra-high (7 T and 9.4 T) field strengths. In validation measurements at 3 T, the method proves to be highly reproducible and excellent agreement between TESS-T_2 and reference T_2 values obtained from single-echo SE scans is found.

5.2 Methods

All numerical simulations, data analysis, and visualization were done using Matlab 7.5 (The MathWorks, Inc., Natick, MA). A repetition time (TR) of 8 ms, an echo time (TE) of 4 ms, and a nominal flip angle (nom) of 25° were used consistently in all simulations. In vitro and in vivo MRI scans were performed on a clinical 3 T system and in vivo UHF imaging either on a 7 T or a 9.4 T system. Manufacturer of all MR systems was Siemens Healthcare, Erlangen, Germany. At 3 T the standard 12-channel head coil of the manufacturer was used, at 7 T a 32-channel head coil (Nova Medical, Wilmington, MA) and at 9.4 T a 16-channel dual-row transmit array in combination with a 31-element receive array [39]. All measurements were conducted on healthy volunteers and approved by the local ethics committee.

5.2.1 TESS sequence principle

Two decades ago, Mizumoto and Yoshitome already presented a type of nonbalanced SSFP sequences that allows the acquisition of higher-order echoes by extending and expanding the gradients in frequency encoding direction [40]. Since those echoes achieved under a steady-state condition show complicated T_1 and T_2 dependencies, images with different contrasts can be obtained. TESS relaxometry as suggested in [33] makes use of this multiple echo approach based on a nonbalanced SSFP sequence that generates three echoes within every TR: the lowest order SSFP-FID (free induction decay) mode (F_0), the lowest order SSFP-Echo mode (F_{-1}), and a higher-order SSFP-FID mode (F_1). Analytical expressions for the ideal SSFP signal amplitudes (no motion, no diffusion, quasi-instantaneous radiofrequency (RF) pulses) can be found, e.g. in [41].

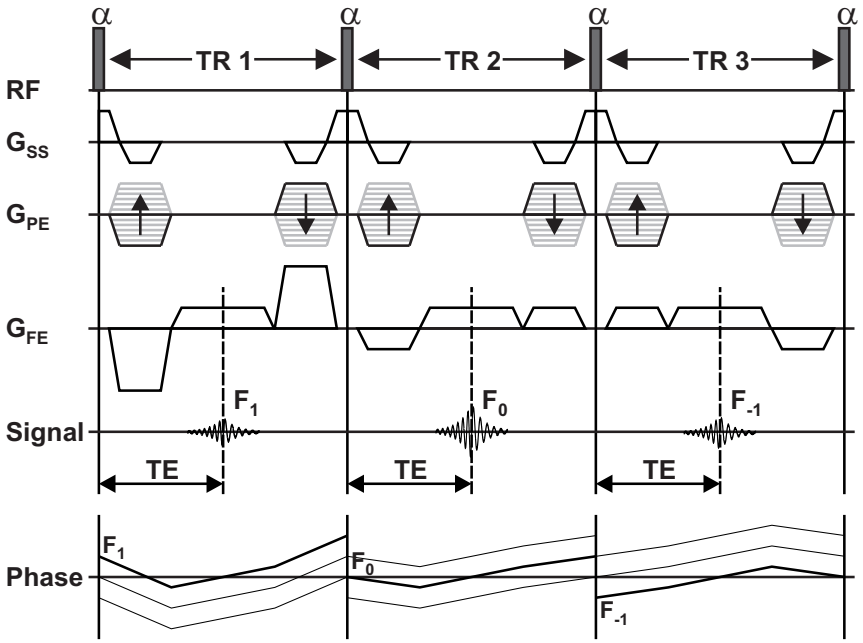

Figure 5.1: 2D TESS sequence scheme: The three SSFP signal modes (F_1, F_0, and F_{-1}) are acquired within separate RF cycles (each signal within one) to ensure short TR. Gradient moments along slice selection and phase encoding axes are nulled within each TR while the gradients along frequency encoding direction induce a dephasing of 2π/voxel. TESS thus belongs to the class of nonbalanced SSFP sequences. The last row illustrates the phase evolution of the three acquired SSFP-modes induced by the gradient waveform along frequency encoding direction. The thick labeled lines depict the path of the acquired echoes. The dephasing gradients may also be played in phase instead of frequency encoding direction but not in slice selection direction since nonideal slice profiles inherent to 2D imaging will disturb the F_1, F_0, and F_{-1} phase configurations [43]. Only results from dephasing in frequency encoding direction are included in this work.

Generally, higher order SSFP modes become more strongly susceptibility weighted, and in the presence of strong local magnetic field variations induced by susceptibility effects or imperfections in B_0, the transverse magnetization decays with T_2^* rather than with T_2. This sensitivity can be reduced by using shorter TR, cf. [42], Eq. (11). As a result, especially in the prospect of UHF imaging, the TR of TESS should be kept short. To this end, the three echoes are acquired individually (see Fig. 5.1), i.e. within three consecutive rather than within one single TR [33].

5.2.2 2D TESS-based T_2 relaxometry

For slice selection, Hanning windowed apodized SINC-shaped excitation pulses with selectable time-bandwidth product (TBW) and duration T_{RF} were used [44]. In the small flip angle approximation [45], also known as Fourier transform approximation, the corresponding flip angle profile is equivalent to the slice profile, and can be derived

as the inverse Fourier transform of the RF pulse envelope

$$\alpha(\Delta\omega) \approx \gamma \left| \int_{t=0}^{T_{RF}} B_1(t) \exp(i\Delta\omega t) \mathrm{d}t \right|. \tag{5.1}$$

This approximation holds very well for flip angles up to 30° and is therefore valid for TESS relaxometry which is optimal for low flip angles (< 30°) [33]. Note that Eq. (5.1) continues to hold well for flip angles up to 90° and severely breaks down only when $\alpha > 90°$ [44, 45]. At large flip angles, where the nonlinearity of the Bloch equations causes deviations from Eq. (5.1), a forward Shinnar-Le Roux (SLR) transform that accounts for this nonlinearity might be preferred to determine the slice profile [46].

For 2D TESS imaging, the accumulated signal of the individual modes,

$$\hat{F}_{1,0,-1} = \sum_{i=1}^{N} F_{1,0,-1}(\alpha_i), \tag{5.2}$$

depends on the flip angle (slice) profile $\alpha(\Delta\omega)$ sampled at N discrete points α_i. In complete analogy to [33], for a given fixed set of protocol parameters (TR, TE, and α), the following two signal ratios are now investigated for relaxometry:

$$\begin{aligned} s_{T_2}(T_1) &:= \frac{\hat{F}_1}{\hat{F}_0} \quad \text{and} \\ s_{T_1}(T_2) &:= \frac{\hat{F}_{-1}}{\hat{F}_0 - \hat{F}_1}. \end{aligned} \tag{5.3}$$

From the two measured signal ratios described by Eq. (5.3), T_1 and T_2 values can be derived as follows: The relaxation time calculation is initialized by a global guess for T_1 and a one-dimensional golden section search is performed to find a first estimate for T_2 from the ratio s_{T_1}. The obtained T_2 is used to calculate an improved T_1 based on ratio s_{T_2} again using a golden section search. The improved T_1 can then be used again to yield an updated T_2. This procedure is iterated until the change in both T_1 and T_2 is less than a predefined convergence tolerance, for more details on this iterative T_1 and T_2 derivation cf. Ref. [33], Eqs. (6-8). Note that for the ratio $s_{T_2}(T_1)$ ($s_{T_1}(T_2)$) the relaxation time T_2 (T_1) is formally treated as a bound variable (indicated by the subscript T_2 (T_1)) whereas T_1 (T_2) represents a running variable. For a given set of protocol parameters (TR, TE, and α), the signal ratios thus depend only on one running variable.

In principle, TESS-relaxometry as described above offers quantification of both, T_1 and T_2, relaxation times. The results presented in Ref. [33], however, indicate that TESS-T_1 is impaired by B_1 field inhomogeneities. TESS-T_2, in contrast, proved to be highly B_1-insensitive thus motivating the purpose of this work, namely TESS-T_2 relaxometry of the human brain at high to ultra-high field strengths.

Optimal flip angle settings for 2D TESS-based T_2 relaxometry in terms of SNR in the derived T_2 maps can be found by performing a Monte Carlo simulation and analyzing the propagation of noise from the base images to the final T_2 maps, in complete analogy to Ref. [33], Fig. 5. For tissues ($T_2/T_1 \sim 0.05$ 0.1), a pronounced

SNR maximum is found for flip angles about $20° - 25°$. As a consequence, a flip angle of 25° was chosen for all measurements within this work.

5.2.3 In vitro study

TESS-based T_2 mapping was evaluated in vitro at 3 T using spherical phantoms of about 14 cm in diameter containing different concentrations of manganese(II) chloride diluted in water (0.5 mM, 0.25 mM, 0.125 mM, 0.05 mM, and 0.025 mM $MnCl_2$ in H_2O). Single-slice TESS imaging (4 mm slice thickness) was performed with a 64 × 64 matrix (4 × 4 mm^2 in-plane resolution), a nominal flip angle of 25°, a TBW of either 2 or 4, a receive bandwidth of 440 Hz/pixel, and a TR and TE of 9.34 ms and 4.81 ms, respectively. A preparation time of 5 s was used to ensure steady state conditions of the transverse magnetization and 8 averages were taken yielding a total measurement time of 19 s. From the acquired three SSFP signal modes (F_1, F_0, and F_{-1}), TESS-T_2 values were calculated with and without slice profile correction.

Reference T_2 was derived from seven consecutive single-echo SE scans with TE values ranging from 5 ms up to 80 ms, 175 ms, 350 ms, 750 ms, and 1250 ms for probes containing 0.5 mM, 0.25 mM, 0.125 mM, 0.05 mM, and 0.025 mM $MnCl_2$ in H_2O, respectively. One single slice (5 mm thickness and 2.5 × 5.0 mm^2 in-plane resolution, 128 × 32 matrix size) was acquired within 3 min 18 s at a receive bandwidth of 698 Hz/pixel. A long TR of 6 s was used to guarantee complete T_1 recovery. Stimulated echo contamination in SE-based T_2 measurements [22] was minimized by following a single-echo rather than a multi-echo approach.

5.2.4 In vivo measurements

Axial human brain scans using single-slice TESS imaging (3 mm slice thickness) were performed at 3 T, 7 T, and 9.4 T. The enhanced SNR at ultra-high magnetic field strength was invested into improved in-plane resolution, yielding 0.5 × 0.5 mm^2 at 7 T and 9.4 T compared to 0.9 × 0.9 mm^2 at 3 T, and into an increase of the receive bandwidth from 160 Hz/pixel at 3 T to 698 Hz/pixel at 7 T and 9.4 T in order to shorten TR and, as a consequence, to reduce susceptibility effects. The duration of the RF pulse had to be stretched from 400 μs at 7 T to 1200 μs at 9.4 T due to SAR restrictions. Achieved TR (TE) at 3 T, 7 T, and 9.4 T was 12.66 (6.35) ms, 7.08 (3.67) ms, and 7.88 (4.07) ms, respectively. A parallel acquisition technique (GRAPPA) was used to shorten the acquisition time per image thus further mitigating motion sensitivity. Eight averages were taken to provide enough SNR in the base data, resulting in total measurement times of 36.6 s, 32.6 s, and 36.2 s at 3 T, 7 T, and 9.4 T, respectively. All protocol details are given in Table 5.1.

At 3 T, reference T_2 values were obtained from five consecutive single-echo SE scans (10 slices, 3 mm gap, 3 mm thickness, 0.9 × 0.9 mm^2 in-plane resolution, 256 × 176 matrix, including a receive bandwidth of 120 Hz/pixel and a TR of 1410 ms). Corresponding echo times were ranging from 20 ms to 100 ms. One single-echo SE scan was completed within 2 min 25 s by using GRAPPA (acceleration factor: 2, reference lines: 24) to reduce measurement time. Respective single-slice TESS images at 3 T were acquired for selected slice positions contained in the SE reference slab using identical in-plane resolution and slice thickness as described above.

Table 5.1: MR scan parameters of in vivo single-slice 2D triple-echo steady-state (TESS) imaging.

	3 T	7 T	9.4 T
In-plane resolution [mm^2]	0.9 × 0.9	0.5 × 0.5	0.5 × 0.5
Image encoding matrix	256 × 208	448 × 350	448 × 350
Slice thickness [mm]	3	3	3
TR [ms]	12.66	7.08	7.88
TE [ms]	6.35	3.67	4.07
Nominal flip angle [°]	25	24	24
Receive bandwidth [Hz/pixel]	160	698	698
Duration of RF pulse [μs]	740	400	1200
TBW of RF pulse	2	2	2
Number of averages	8	8	8
Parallel imaging technique	GRAPPA[a]	GRAPPA[a]	GRAPPA[a]
Total acquisition time [s]	36.6	32.6	36.2

[a]GRAPPA, generalized autocalibrating partially parallel acquisition; acceleration factor: 2; reference lines: 32.

Possible severe deviations in B_1, as expected at UHF, were modeled at 3 T for both, TESS scans as well as single-echo SE scans, by a detuning of the RF reference amplitude for the excitation of protons at the MR scanner, i.e., once to 0.5 times and once to 1.5 times its reference value. By this means, deviations of ± 50 % were induced between actual and nominal flip angle.

The reproducibility of TESS-based T_2 quantification in the human brain was analyzed by means of ten consecutive scans of one subject at 3 T. After each scan, the subject was taken out and repositioned for the next scan to mimic and enforce new measurement conditions. Slice positioning was performed manually and special care was taken to position the slices nearly identical for all measurements, however, some variability in T_2 introduced by slight misalignments could be expected. As a consequence, reproducibility was assessed for a region of interest (ROI) placed in frontal white matter where only small through-plane tissue variations were assumed and quantified by the coefficient of variation (calculated as the ratio of the standard deviation to the mean).

5.3 Results and discussion

5.3.1 Slice profile effects

If the effect of imperfect slice profiles inherent to 2D imaging is not accounted for, i.e. $\hat{F}_{1,0,-1} = F_{1,0,-1}(\alpha_{\mathrm{nom}})$ in Eq. (5.2), TESS-T_2 relaxometry is clearly impaired. The arising systematic error is simulated in Figure 5.2 versus T_2/T_1 for SINC pulses with TBW values of 2, 4, 6, and 8 (dashed lines). At TBW = 2, TESS-based T_2 values are

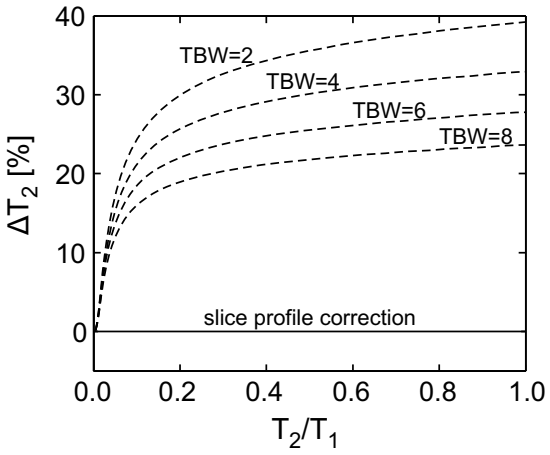

Figure 5.2: Systematic error arising in T_2 relaxometry based on 2D-TESS if imperfections in the slice profile are neglected. The error is quantified by $\Delta T_2 = [(T_2 - T_{2,\mathrm{calc}})/T_2] \cdot 100\,\%$, where T_2 is the true T_2 relaxation time and $T_{2,calc}$ the calculated one, and plotted versus T_2/T_1 values ranging from tissues (0.05 – 0.1) to fluids (~ 1) for SINC pulses with a TBW of 2, 4, 6, and 8 (dashed lines). With slice profile correction (cf. Eqs. (5.1)-(5.3)), this error can be entirely eliminated independent of the RF pulse shape (solid line).

considerably reduced relative to the true relaxation times to about 20 % for tissues (T_2/T_1 ~ 0.05 – 0.1) and up to 39 % for fluids (T_2/T_1 ~ 1). By increasing TBW, i.e. approaching an ideal rectangular profile, the error becomes smaller, but only slightly. At TBW = 8, the residual error is still about 15 % for tissues and up to 23 % for fluids (cf. Fig. 5.2). This systematic error can be eliminated by incorporating the slice profile directly into the TESS-T_2 calculation, cf. Eqs. (5.1)-(5.3) (solid line in Fig. 5.2).

The results obtained from simulations were verified on in vitro validation measurements at 3 T and are summarized in Table 5.2. Without slice profile correction, i.e. assuming an ideal rectangular slice profile, relaxometry based on 2D-TESS underestimates T_2 compared to the reference single-echo SE-based method which is regarded in the following as gold standard [47] (cf. Table 5.2). For probes containing 0.5 mM, 0.25 mM, 0.125 mM, 0.05 mM, and 0.025 mM $MnCl_2$ in H_2O, the relative difference between SE-T_2 and TESS-T_2 calculated as [(SE-T_2 – TESS-T_2) / SE-T_2) · 100 % yields 3.3 % (3.3 %), 8.6 % (8.0 %), 18.5 % (16.5 %), 30.0 % (26.4 %), and 35.8 % (32.8 %), respectively for 2D TESS scans using SINC pulses of TBW = 2 (TBW = 4) for slice selection.

The systematic error in TESS-T_2 induced by imperfect slice profiles thus increases with higher T_2 relaxation times and can barely be reduced by using RF pulses with higher TBW, i.e. by improving the slice profile (cf. Table 5.2), in accordance with the simulations (recall Fig. 5.2). With slice profile correction (cf. Eqs. (5.1)-(5.3)), excellent agreement between TESS-T_2 and SE-T_2 is found for both applied SINC pulses with TBWs of either 2 or 4 (cf. Table 5.2). The relative difference in T_2 between slice profile corrected TESS-T_2 and the gold standard measurement is below 1 % for all

Table 5.2: 2D TESS-T_2 quantification was demonstrated in vitro on manganese-doped aqueous probes at 3 T using SINC pulses with a TBW of either 2 or 4 for slice selection. TESS-T_2 values derived without slice profile correction are compared to the corresponding corrected values and results from T_2 measurements based on single-echo SE data are given for reference.

[$MnCl_2$]	TESS-T_2 [ms]				SE-T_2 [ms] (single-echo)
	TBW = 2		TBW = 4		
	Slice profile correction OFF	Slice profile correction ON	Slice profile correction OFF	Slice profile correction ON	
0.500 mM	17.6 ± 0.1	18.3 ± 0.1	17.6 ± 0.1	18.2 ± 0.1	18.2 ± 0.1
0.250 mM	29.9 ± 0.2	33.0 ± 0.2	30.1 ± 0.2	32.8 ± 0.2	32.7 ± 0.1
0.125 mM	58.4 ± 0.5	72.4 ± 0.7	59.9 ± 0.7	72.2 ± 0.9	71.7 ± 0.2
0.050 mM	121.5 ± 1.4	173.4 ± 2.2	127.7 ± 1.9	172.5 ± 3.0	173.6 ± 0.7
0.025 mM	213.0 ± 4.4	336.3 ± 9.3	222.9 ± 5.4	323.2 ± 9.1	331.8 ± 2.4

probes with $MnCl_2$ concentrations ranging from 0.5 to 0.05 mM. The error increases slightly with lower concentrations of $MnCl_2$ (i.e. higher T_2 values) yielding about 1.4 % (2.6 %) deviation for the probe containing 0.025 mM $MnCl_2$ and for TBW = 2 (TBW = 4). This may be attributed to the fact that TESS-based T_2 relaxometry includes more noise in the final T_2 maps for higher T_2/T_1 ratios (cf. Ref. [33], Fig. 5). However, for brain tissues the main target of this work with reported average T_2 values of 80 ms for gray and 110 ms for white matter at 3 T [48] high accuracy of the proposed method can be expected (cf. Table 5.2).

From these initial results, it can be seen that the incorporated slice profile correction accounts sufficiently accurate for imperfect RF profiles even if simple SINC pulses with small TBWs and thus generating poor slice profiles are used. Lower TBW enables to apply RF pulses of shorter duration and hence reduced power deposition in human tissues. This is particularly beneficial with regard to UHF TESS imaging where SAR becomes critical and TR should be kept short to eliminate susceptibility artifacts.

As a consequence, all in vivo 2D TESS scans at 3 T, 7 T, and 9.4 T were performed using SINC-pulses of TBW = 2 for slice selection. In the following, TESS-T_2 derived from simulations and in vivo measurements consistently refers to the slice profile corrected values.

5.3.2 Sensitivity to transmit field inhomogeneity

The sensitivity to B_1 of 2D TESS-T_2 relaxometry was simulated using SINC pulses of varying TBWs (range, 2 – 8) and is illustrated in Figure 5.3 for the example of TBW = 2. It can be seen that, for a broad range of T_2/T_1 values and simulated flip angle miscalibrations of up to ± 50 %, the produced error in the T_2 calculation does not exceed 0.2 % (cf. Fig. 5.3), independent of the TBW value. The intriguing B_1 insensitivity of TESS-T_2 quantification reported in Ref. [33] for 3D imaging is thus

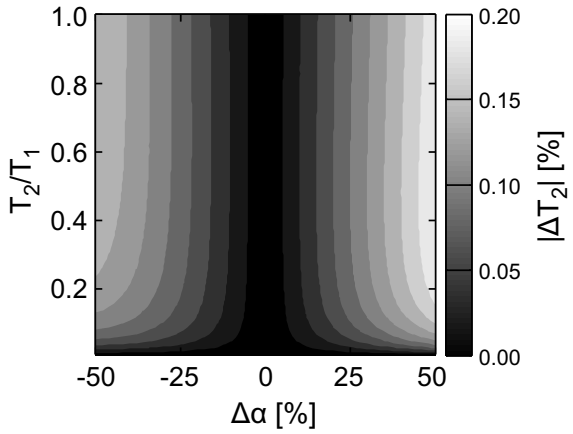

Figure 5.3: Sensitivity of 2D TESS-T_2 relaxometry to flip angle errors resulting from B_1 field inhomogeneity simulated for a SINC pulse with TBW = 2. B_1 sensitivity is reflected by the error in T_2 modeled as $\Delta T_2 = [(T_2 - T_{2,\mathrm{calc}})/T_2] \cdot 100\,\%$ (T_2: true T_2 relaxation time, $T_{2,\mathrm{calc}}$: calculated T_2 relaxation time) plotted versus T_2/T_1 and flip angle variations $\Delta\alpha = [(\alpha_{\mathrm{act}} - \alpha_{\mathrm{nom}})/\alpha_{\mathrm{nom}}] \cdot 100\,\%$ (α_{act}: actual flip angle produced at the center of the slice, α_{nom}: nominal flip angle).

not affected by incorporating the effect of nonideal slice profiles as inherent to 2D acquisitions into T_2 relaxation time calculation.

This result was confirmed by in vivo T_2 measurements at 3 T based on 2D TESS imaging as demonstrated in Figure 5.4 (first row) for two axial slice positions in the human brain, each scanned three times at differently tuned RF amplitudes (at 0.5, 1.0, and 1.5 times the nominal RF amplitude). For reference, T_2 measurements based on a single-echo SE approach were performed at the same RF amplitudes (see Fig. 5.4, second row). TESS- and SE-based T_2 values were assessed for selected regions of interest (indicated by the numbered asterisks in Fig. 5.4) and are summarized in Table 5.3.

As predicted by the simulations, TESS-T_2 behavior is highly B_1 insensitive (cf. Fig. 5.4, first row). In particular, TESS-T_2 was demonstrated to be comparably robust to B_1 field variations as the reference gold standard technique (see Table 5.3). TESS-T_2 values assessed for scans at 0.5 and 1.5 times the nominal amplitude deviate overall only between 2 – 8 % from the value at nominal amplitude whereas for the single-echo SE-based T_2 measurements even larger deviations are observed, e.g. for gray matter in the caudate nucleus head at 1.5 times the nominal amplitude where the assessed T_2 (42 ± 4 ms) deviates by about 13 % from the nominal value (48 ± 3 ms) (cf. Table 5.3).

5.3.3 Accuracy and reproducibility in vivo

In general, good agreement between T_2 relaxometry data derived based on TESS and single-echo SE is found in the axial human brain scans at 3 T (see Fig. 5.4 and Table 5.3). A small, but systematic increase in TESS-T_2 values of human brain tissues with higher B_1 amplitude and consequently higher actual flip angles is observed. This

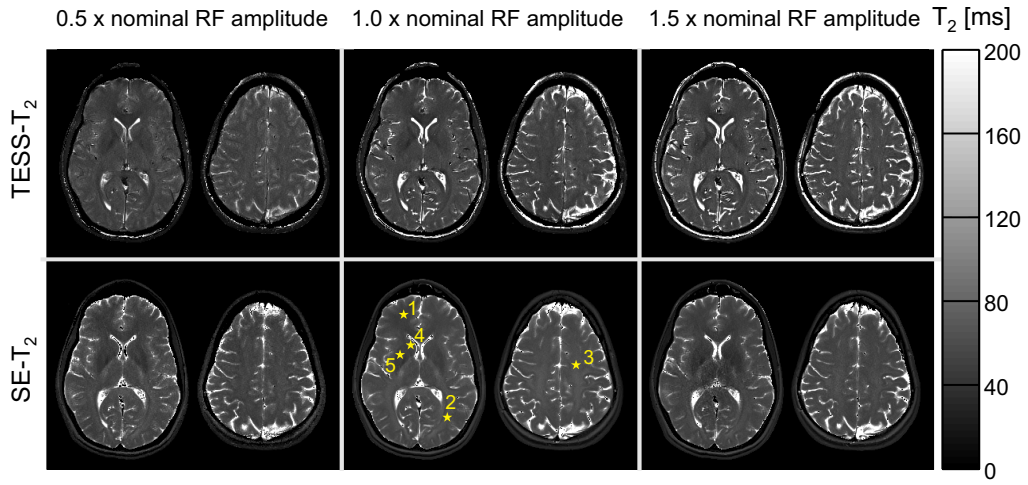

Figure 5.4: In vivo evaluation at 3 T. 2D TESS-T_2 maps of the human brain (first row) are compared with T_2 values derived from reference single-echo SE scans (second row) for two axial slice positions. Robustness to B_1 field variations was examined by manually adjusting the reference RF amplitude at the MR scanner. TESS as well as reference SE scans were performed at 0.5 (left column), 1.0 (center), and 1.5 (right) times the nominal RF amplitude. For five regions of interest placed at the positions indicated by the numbered asterisks in the SE-T_2 maps (center column), T_2 values are summarized in Table 5.3. The apparent damping of TESS-T_2 values obtained for CSF at reduced RF amplitude (first row, left column) can be attributed to signal modulations from diffusion at lower flip angles [49]. TESS-T_2 values of brain tissues are only negligibly affected by diffusion effects (see Table 5.3).

Table 5.3: TESS-T_2 relaxometry data for selected ROIs in white matter (WM) and gray matter (GM) of the human brain at 3 T depending on the RF amplitude in comparison with single-echo SE T_2 measurements

Brain tissue		TESS-T_2 [ms]			SE-T_2 [ms] (single-echo)		
		RF amplitude factor[b]					
		0.5	1.0	1.5	0.5	1.0	1.5
WM	Frontal WM (1)[a]	44 ± 3	47 ± 3	49 ± 4	46 ± 5	48 ± 2	48 ± 2
	Occipital WM (2)[a]	53 ± 5	56 ± 5	57 ± 6	60 ± 5	62 ± 3	56 ± 3
	Centrum semiovale (3)[a]	50 ± 4	53 ± 5	55 ± 6	51 ± 4	52 ± 3	47 ± 4
GM	Caudate nucleus head (4)[a]	45 ± 4	46 ± 4	49 ± 8	44 ± 4	48 ± 3	42 ± 4
	Putamen (5)[a]	53 ± 4	53 ± 5	57 ± 6	55 ± 4	63 ± 3	55 ± 4

[a] The numbers in parentheses correspond to the regions of interest indicated in Fig. 5.4.
[b] Factor by which the nominal RF amplitude for proton excitation at the MR scanner was multiplied.

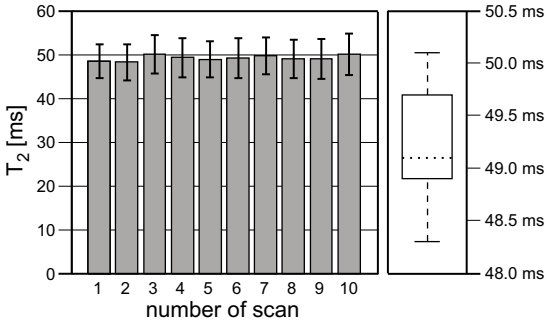

Figure 5.5: TESS-T_2 variability at 3 T assessed with ten consecutive scans of a healthy volunteer for a ROI placed in the frontal white matter of the left brain hemisphere. Mean calculated T_2 was 49.2 ± 0.6 ms, yielding a coefficient of variation of 0.012. The plot on the right-hand side shows the median T_2 value (dotted line), lower and upper quartile values (bottom and top of the box) and the extent of the data from minimal to maximal values visualized by the dashed line.

effect is highly likely to be caused by enhanced sensitivity to diffusion of high-resolution TESS-based T_2 quantification at lower flip angles. The expected signal modulations from diffusion and their propagation into TESS-T_2 values depending on the flip angle can be simulated following Freed et al. [49]. It is found that TESS-T_2 of tissues is only negligibly affected in agreement with the obtained results for brain tissues (cf. Table 5.3), while diffusion effects may considerably modulate the signals of fluids (such as CSF in the brain) at small flip angles resulting in an underestimation of T_2 because of the extremely long T_2 persistence times of all modes (in the order of seconds for CSF). This is apparent in the TESS-T_2 map obtained at 0.5 times the nominal RF amplitude where CSF appears less bright (cf. Fig. 5.4, first row, left column). As reported in related work, signal damping due to diffusion is especially prominent for fluids in the SSFP-Echo (F_{-1}) mode in the low flip angle regime [50] and at high resolution [51].

TESS-T_2 quantification is highly reproducible. The coefficient of variation calculated for a region of interest in frontal white matter of the left brain hemisphere, derived from ten measurements of the same healthy volunteer at 3 T, is only about 0.012. TESS-T_2 variability of the assessed ROI is illustrated in Figure 5.5.

5.3.4 UHF T_2 quantification

Rapid T_2 mapping based on 2D-TESS proves to be feasible and reliable in the human brain at ultra-high field strengths (see Fig. 5.6). The obtained high-resolution axial T_2 maps at 7 T (Fig. 5.6 a) and 9.4 T (Fig. 5.6 b) are free of artifacts and characterized by a homogeneous contrast behavior across the entire slice thus demonstrating the unique B_1 insensitivity of 2D TESS-based T_2 relaxometry as well as the robustness of the underlying sequence to B_0 field variations which increase proportional to the field strength [34]. Representative T_2 values assessed for frontal white matter in the left brain hemisphere are: 23 ± 2 ms / 28 ± 2 ms at 7 T (left / right slice in Fig. 5.6 a) and 20 ± 2 ms / 25 ± 2 ms at 9.4 T (left / right slice in Fig. 5.6 b).

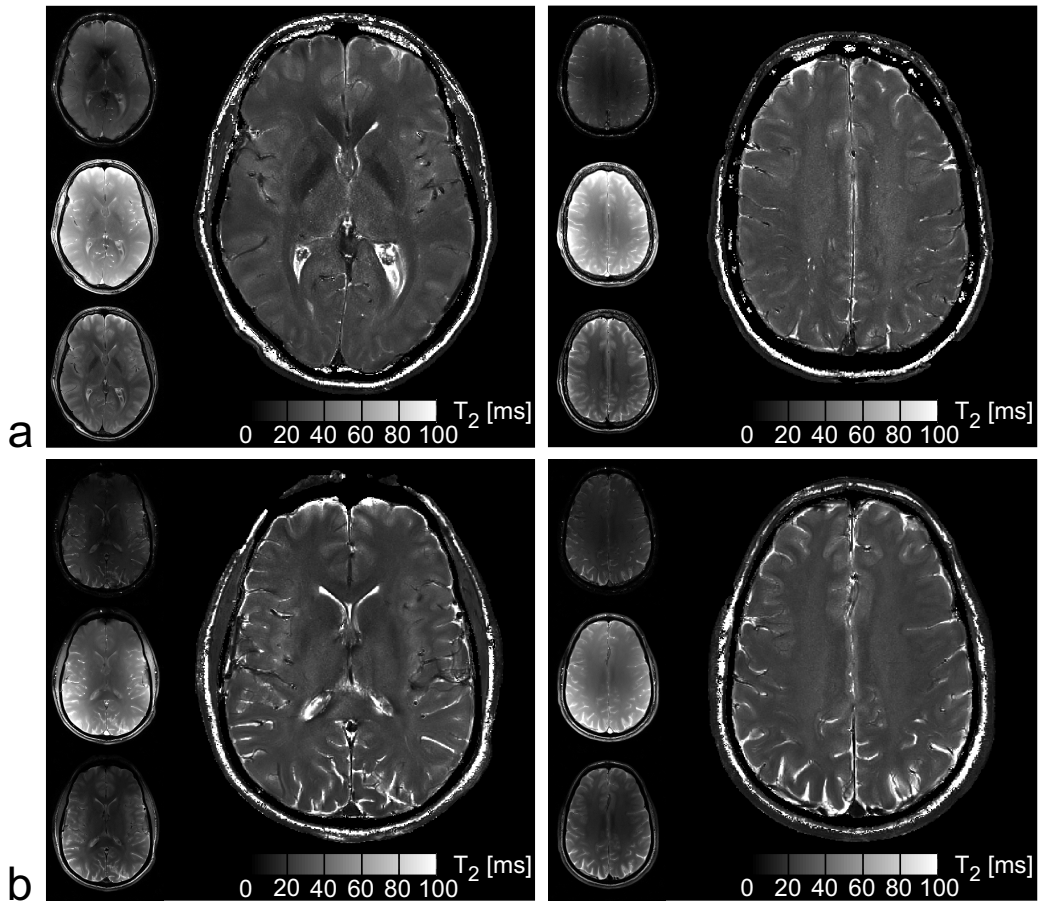

Figure 5.6: Representative T_2 maps obtained with rapid 2D TESS imaging for two axial slices at (a) 7 T and (b) 9.4 T. For each slice, the three acquired base signal modes are shown on the left (F_1, F_0, and F_{-1} from top to bottom).

At 7 T and above, transmit head coils providing volume coverage typically produce B_1 field patterns with high RF amplitude in the center of the brain and much reduced values towards the periphery [34]. No evidence can be observed in Figure 5.6 that the B_1 insensitivity of TESS-T_2 breaks down at very large fields. On the contrary: TESS-T_2 remains completely unaffected even at 9.4 T, as a consequence taking full advantage of the increased SNR at such high field strength.

5.3.5 Potential and limitations of 2D TESS-T_2 relaxometry

Major benefit of employing TESS-T_2 quantification at high to ultra-high fields is its observed intriguing robustness in the presence of large B_1 field variations. Rapid relaxometry techniques based on SSFP imaging generally suffer from their sensitivity to flip angle errors arising from B_1 inhomogeneity. To the best of our knowledge, TESS-T_2 relaxometry is the first suggested SSFP method that overcomes this drawback without need for corrective strategies, just exhibiting an intrinsic highly B_1-insensitive behavior.

In this work, the motion sensitivity of 3D-TESS initially proposed in Ref. [33] was mitigated by a rapid 2D approach making TESS-T_2 relaxometry feasible in nonrigid targets such as the human brain. Slice profile effects inherent to 2D imaging were eliminated by incorporating the flip angle profile directly into T_2 calculation. There was no need for optimized RF pulse design, such as SLR pulses with in fact improved but still far from ideal excitation profiles [46]. Instead, simple and fast SINC-shaped RF pulses with small TBW even though producing a rather poor slice profile could be used.

2D TESS-T_2 quantification has demonstrated to be highly insensitive to the two major sources of flip angle errors, that is B_1 field heterogeneities and imperfect slice profiles. In combination with the robustness to B_0 inhomogeneities and the ability to apply low-SAR pulses of short duration and small flip angles, TESS imaging has proved to be suited for UHF applications.

The presented 2D TESS imaging approach was limited to single-slice acquisitions. However, the underlying sequence can easily be modified for the use of multi-band RF pulses as employed in a parallel imaging technique known as CAIPIRINHA [52]. By this means, multiple slices are excited simultaneously providing accelerated 2D TESS multi-slice imaging and increased volumetric coverage with possible acquisition times of less than 10 s per slice.

As observed, high-resolution TESS imaging may be subject to signal modulations from diffusion. While the T_2 values of CSF obtained from TESS scans of the human brain at 3 T in fact reflected some diffusion sensitivity (cf. Fig. 5.4, first row), TESS-T_2 quantification of human brain tissues was only negligibly affected (cf. Table 5.3).

5.4 Conclusions

A rapid T_2 relaxometry method based on 2D TESS acquisitions was presented. It offers accurate and robust T_2 quantification of human tissues even in the presence of substantial B_0 and B_1 field inhomogeneities as has been demonstrated within the scope of this work for high to ultra-high field imaging of the human brain. Derivation

of TESS-T_2 relaxation times was highly reproducible making the suggested method suitable for clinical applications. The results accentuate the potential of TESS-T_2 relaxometry to emerge as a valuable measure for early diagnosis and progression monitoring of brain diseases in rapid high-resolution 2D scans at high to ultra-high fields.

References

[1] R. Damadian. Tumor detection by nuclear magnetic resonance. *Science*, 171 (3976):1151–3, 1971.

[2] P. Tofts. *Quantitative MRI of the Brain*. John Wiley & Sons Ltd, Chichester, 2003.

[3] A. Pitkanen, M. Laakso, R. Kalviainen, K. Partanen, P. Vainio, M. Lehtovirta, P. Riekkinen, and H. Soininen. Severity of hippocampal atrophy correlates with the prolongation of MRI T2 relaxation time in temporal lobe epilepsy but not in Alzheimer's disease. *Neurology*, 46(6):1724–30, 1996.

[4] P. Williamson, D. Pelz, H. Merskey, S. Morrison, S. Karlik, D. Drost, T. Carr, and P. Conlon. Frontal, temporal, and striatal proton relaxation times in schizophrenic patients and normal comparison subjects. *Am J Psychiatry*, 149 (4):549–51, 1992.

[5] H. B. Larsson, J. Frederiksen, J. Petersen, A. Nordenbo, I. Zeeberg, O. Henriksen, and J. Olesen. Assessment of demyelination, edema, and gliosis by in vivo determination of T1 and T2 in the brain of patients with acute attack of multiple sclerosis. *Magn Reson Med*, 11(3):337–48, 1989.

[6] M. Neema, D. Goldberg-Zimring, Z. D. Guss, B. C. Healy, C. R. Guttmann, M. K. Houtchens, H. L. Weiner, M. A. Horsfield, D. B. Hackney, D. C. Alsop, and R. Bakshi. 3 T MRI relaxometry detects T2 prolongation in the cerebral normal-appearing white matter in multiple sclerosis. *Neuroimage*, 46(3):633–41, 2009.

[7] G. Bonnier, T. Sumpf, D. Romanasco, A. Roche, M. Schluep, R. Du Pasquier, J. Frahm, G. Krueger, and C. Granziera. Ultra-fast T2 mapping of multiple sclerosis pathology in early disease. In *Proc Intl Soc Mag Reson Med*, page 3615, 2013.

[8] K. Scheffler and J. Hennig. T(1) quantification with inversion recovery TrueFISP. *Magn Reson Med*, 45(4):720–3, 2001.

[9] S. C. Deoni, T. M. Peters, and B. K. Rutt. High-resolution T1 and T2 mapping of the brain in a clinically acceptable time with DESPOT1 and DESPOT2. *Magn Reson Med*, 53(1):237–41, 2005.

[10] G. H. Welsch, K. Scheffler, T. C. Mamisch, T. Hughes, S. Millington, M. Deimling, and S. Trattnig. Rapid estimation of cartilage T2 based on double echo at steady state (DESS) with 3 Tesla. *Magn Reson Med*, 62(2):544–9, 2009.

[11] O. Bieri, K. Scheffler, G. H. Welsch, S. Trattnig, T. C. Mamisch, and C. Ganter. Quantitative mapping of T2 using partial spoiling. *Magn Reson Med*, 66(2): 410–8, 2011.

[12] R. Heule, C. Ganter, and O. Bieri. Rapid estimation of cartilage T2 with reduced T1 sensitivity using double echo steady state imaging. *Magn Reson Med*, 71(3): 1137–1143, 2014.

[13] D. Ma, V. Gulani, N. Seiberlich, K. Liu, J. L. Sunshine, J. L. Duerk, and M. A. Griswold. Magnetic resonance fingerprinting. *Nature*, 495(7440):187–92, 2013.

[14] T. J. Sumpf, M. Uecker, S. Boretius, and J. Frahm. Model-based nonlinear inverse reconstruction for T2 mapping using highly undersampled spin-echo MRI. *J Magn Reson Imaging*, 34(2):420–8, 2011.

[15] C. A. McKenzie, Z. Chen, D. J. Drost, and F. S. Prato. Fast acquisition of quantitative T2 maps. *Magn Reson Med*, 41(1):208–12, 1999.

[16] M. Doneva, P. Bornert, H. Eggers, C. Stehning, J. Senegas, and A. Mertins. Compressed sensing reconstruction for magnetic resonance parameter mapping. *Magn Reson Med*, 64(4):1114–20, 2010.

[17] J. Hennig, A. Nauerth, and H. Friedburg. RARE imaging: a fast imaging method for clinical MR. *Magn Reson Med*, 3(6):823–33, 1986.

[18] H. Y. Carr and E.M. Purcell. Effects of diffusion on free precession in nuclear magnetic resonance experiments. *Phys Rev*, 94(3):630–638, 1954.

[19] S. Meiboom and D. Gill. Modified spin-echo method for measuring nuclear relaxation times. *Rev Sci Instrum*, 29:688–691, 1958.

[20] H. Y. Carr. Steady-state free precession in nuclear magnetic resonance. *Phys Rev*, 112(5):1693–1701, 1958.

[21] S. Majumdar, S. C. Orphanoudakis, A. Gmitro, M. O'Donnell, and J. C. Gore. Errors in the measurements of T2 using multiple-echo MRI techniques. I. Effects of radiofrequency pulse imperfections. *Magn Reson Med*, 3(3):397–417, 1986.

[22] R. M. Lebel and A. H. Wilman. Transverse relaxometry with stimulated echo compensation. *Magn Reson Med*, 64(4):1005–14, 2010.

[23] S. C. Deoni. High-resolution T1 mapping of the brain at 3T with driven equilibrium single pulse observation of T1 with high-speed incorporation of RF field inhomogeneities (DESPOT1-HIFI). *J Magn Reson Imaging*, 26(4):1106–11, 2007.

[24] J. G. Sled and G. B. Pike. Correction for B(1) and B(0) variations in quantitative T(2) measurements using MRI. *Magn Reson Med*, 43(4):589–93, 2000.

[25] V. L. Yarnykh. Actual flip-angle imaging in the pulsed steady state: a method for rapid three-dimensional mapping of the transmitted radiofrequency field. *Magn Reson Med*, 57(1):192–200, 2007.

[26] L. I. Sacolick, F. Wiesinger, I. Hancu, and M. W. Vogel. B1 mapping by Bloch-Siegert shift. *Magn Reson Med*, 63(5):1315–22, 2010.

[27] K. Nehrke and P. Bornert. DREAM–a novel approach for robust, ultrafast, multislice B(1) mapping. *Magn Reson Med*, 68(5):1517–26, 2012.

[28] C. Ganter, M. Settles, I. Dregely, F. Santini, K. Scheffler, and O. Bieri. B1+-mapping with the transient phase of unbalanced steady-state free precession. *Magn Reson Med*, 70(6):1515–23, 2013.

[29] S. Majumdar, S. C. Orphanoudakis, A. Gmitro, M. O'Donnell, and J. C. Gore. Errors in the measurements of T2 using multiple-echo MRI techniques. II. Effects of static field inhomogeneity. *Magn Reson Med*, 3(4):562–74, 1986.

[30] O. Bieri and K. Scheffler. Fundamentals of balanced steady state free precession MRI. *J Magn Reson Imaging*, 38(1):2–11, 2013.

[31] S. C. Deoni. Transverse relaxation time (T2) mapping in the brain with off-resonance correction using phase-cycled steady-state free precession imaging. *J Magn Reson Imaging*, 30(2):411–7, 2009.

[32] F Santini, O Bieri, and K Scheffler. Flow compensation in non-balanced SSFP. In *Proc Intl Soc Mag Reson Med*, page 3124, 2008.

[33] R. Heule, C. Ganter, and O. Bieri. Triple echo steady-state (TESS) relaxometry. *Magn Reson Med*, 71(1):230–7, 2014.

[34] J. Hennig and O. Speck. *High-Field MR Imaging*. Medical Radiology. Springer, Heidelberg, 2011.

[35] A. G. van der Kolk, J. Hendrikse, and P. R. Luijten. Ultrahigh-field magnetic resonance imaging: the clinical potential for anatomy, pathogenesis, diagnosis, and treatment planning in brain disease. *Neuroimaging Clin N Am*, 22(2):343–62, 2012.

[36] K. Kollia, S. Maderwald, N. Putzki, M. Schlamann, J. M. Theysohn, O. Kraff, M. E. Ladd, M. Forsting, and I. Wanke. First clinical study on ultra-high-field MR imaging in patients with multiple sclerosis: comparison of 1.5T and 7T. *Am J Neuroradiol*, 30(4):699–702, 2009.

[37] M. Metcalf, D. Xu, D. T. Okuda, L. Carvajal, R. Srinivasan, D. A. Kelley, P. Mukherjee, S. J. Nelson, D. B. Vigneron, and D. Pelletier. High-resolution phased-array MRI of the human brain at 7 Tesla: initial experience in multiple sclerosis patients. *J Neuroimaging*, 20(2):141–7, 2010.

[38] M. Filippi, N. Evangelou, A. Kangarlu, M. Inglese, C. Mainero, M. A. Horsfield, and M. A. Rocca. Ultra-high-field MR imaging in multiple sclerosis. *J Neurol Neurosurg Psychiatry*, 85(1):60–6, 2014.

[39] G. Shajan, M. Kozlov, J. Hoffmann, R. Turner, K. Scheffler, and R. Pohmann. A 16-channel dual-row transmit array in combination with a 31-element receive array for human brain imaging at 9.4 T. *Magn Reson Med*, 71(2):870–9, 2014.

[40] C. T. Mizumoto and E. Yoshitome. Multiple echo SSFP sequences. *Magn Reson Med*, 18(1):244–250, 1991.

[41] W. Hänicke and H. U. Vogel. An analytical solution for the SSFP signal in MRI. *Magn Reson Med*, 49(4):771–5, 2003.

[42] C. Ganter. Static susceptibility effects in balanced SSFP sequences. *Magn Reson Med*, 56(3):687–91, 2006.

[43] K. Scheffler. A pictorial description of steady-states in rapid magnetic resonance imaging. *Concepts Magn Reson*, 11(5):291–304, 1999.

[44] M. A. Bernstein, K. F. King, and X. J. Zhou. *Handbook of MRI Pulse Sequences*. Elsevier Academic Press, Burlington, MA, 2004.

[45] J. Pauly, D. Nishimura, and A. Macovski. A k-space analysis of small-tip-angle excitation. *J Magn Reson*, 213(2):544–57, 1989.

[46] J. Pauly, P. Le Roux, D. Nishimura, and A. Macovski. Parameter relations for the Shinnar-Le Roux selective excitation pulse design algorithm. *IEEE Trans Med Imaging*, 10(1):53–65, 1991.

[47] E. L. Hahn. Spin echoes. *Phys Rev*, 80(4):580–594, 1950.

[48] J. P. Wansapura, S. K. Holland, R. S. Dunn, and Jr. Ball, W. S. NMR relaxation times in the human brain at 3.0 Tesla. *J Magn Reson Imaging*, 9(4):531–8, 1999.

[49] D. E. Freed, U. M. Scheven, L. J. Zielinski, P. N. Sen, and M. D. Hürlimann. Steady-state free precession experiments and exact treatment of diffusion in a uniform gradient. *J Chem Phys*, 119(9):4249–58, 2001.

[50] O. Bieri, C. Ganter, G. H. Welsch, S. Trattnig, T. C. Mamisch, and K. Scheffler. Fast diffusion-weighted steady state free precession imaging of in vivo knee cartilage. *Magn Reson Med*, 67(3):691–700, 2012.

[51] O. Bieri, C. Ganter, and K. Scheffler. On the fluid-tissue contrast behavior of high-resolution steady-state sequences. *Magn Reson Med*, 68(5):1586–92, 2012.

[52] F. A. Breuer, M. Blaimer, R. M. Heidemann, M. F. Mueller, M. A. Griswold, and P. M. Jakob. Controlled aliasing in parallel imaging results in higher acceleration (CAIPIRINHA) for multi-slice imaging. *Magn Reson Med*, 53(3):684–91, 2005.

Chapter 6

Conclusion

6.1 Summary

Within the scope of this thesis, techniques based on steady-state free precession (SSFP) imaging have been proposed and investigated in proof-of-principle studies for rapid, accurate, and precise T_1 and T_2 quantification with possible application in clinical settings. The main results with special emphasis on the potential as well as on the limitations of the presented methods are summarized in the following:

Chapter 2. It was demonstrated in simulations that the accuracy of variable flip angle (VFA) T_1 mapping can substantially be improved for the purpose of human brain tissue quantification by making use of an analytical solution for the RF-spoiled steady-state signal and a global T_2 estimate. The adverse influence of diffusion was shown to be negligible for the typical spoiler gradient moments used in short-TR spoiled gradient-echo (SPGR) acquisitions. In order to account for transmit field inhomogeneities, 3D SPGR imaging was accompanied by B_1 mapping scans. Reliable and accurate T_1 values in the human brain were obtained for white and gray matter in good agreement with gold standard IR reference measurements.

In conclusion, the proposed T_1 calculation approach offers highly accurate T_1 quantification of human brain tissues in acceptable scan times for the clinical routine, however, due to the effect of diffusion some residual sensitivity to the acquisition protocol (i.e. to the RF phase difference increment and to the moment of the spoiler gradient) has to be considered. The presented method yields optimal results in targets for which a good global T_2 guess is available as for human brain tissues. In other regions of the human body with higher T_2 variations, a systematic bias will be introduced.

Chapter 3. Generally a substantial reduction in the T_1-related bias of DESS-based T_2 estimation can be achieved by using a simple global T_1 estimate as demonstrated in simulations. Gold standard single-echo SE T_2 mapping yielded excellent agreement with the T_2 relaxometry data of cartilage obtained from 3D double-echo steady-state (DESS) scans in the knee joint. The improvement of DESS T_2 estimation became particularly evident in the range of low flip angles ($\alpha < 45°$), commonly used for morphological DESS imaging. Furthermore, increased zonal variation in T_2 between deep and superficial cartilage layers were observed.

In conclusion, the obtained results emphasize the potential of DESS to fuse accurate quantitative T_2 and morphological imaging of the musculoskeletal system within a single scan. Optimal results with respect to accuracy are obtained if a good global T_1 guess is available as in the case of cartilage or muscle.

Chapter 4. In simulations, in vitro studies, and 3D triple-echo steady-state (TESS) imaging of the musculoskeletal system at 3 Tesla, it was found that the novel T_1 and T_2 quantification method is not biased by any interacting influence of T_2 on T_1 or T_1 on T_2. Furthermore, it was observed that the T_2 values derived based on TESS are completely insensitive to B_1 field variations. Consequently, excellent correspondence between TESS-T_2 and gold standard single-echo SE T_2 relaxometry data was observed in vitro at 1.5 Tesla and in vivo at 3 Tesla for muscle and cartilage. The T_1 values calculated using the new TESS method showed the expected sensitivity to flip angle

miscalibrations due to B_1 inhomogeneity. In order to obtain accurate T_1 values with TESS, B_1 mapping was stringent as with any other SSFP-based relaxometry method.

In conclusion, TESS offers rapid combined T_1 and T_2 relaxometry within one single scan, is not biased by T_1 or T_2 and robust in the presence of B_0 inhomogeneity due to the nonbalanced nature of the underlying sequence. Furthermore, TESS-based T_2 estimation proved to be completely B_1-insensitive. The proposed method is thus of high interest for fast, robust, and accurate high-resolution T_2 mapping, especially of the musculoskeletal system at high to ultra-high fields. Due to its motion sensitivity, 3D TESS relaxometry is, however, not applicable to nonrigid targets.

Chapter 5. Owing to the achieved short scan times and, as a result, reduced motion sensitivity, rapid single-slice 2D TESS acquisitions were feasible in the human brain. The effect of imperfect slice profiles inherent to 2D imaging was properly incorporated into the T_2 calculation based on 2D TESS. In simulations, in vitro studies, and human brain imaging at 3 Tesla, 2D TESS T_2 quantification proved to be highly robust in the presence of B_1 field variations. As a consequence, excellent agreement between TESS and gold-standard single-echo SE T_2 measurements was found in vitro and in vivo for human brain tissues at 3 Tesla. At ultra-high field strengths (7 and 9.4 Tesla), T_2 relaxometry based on 2D TESS imaging delivered reliable and robust results in the human brain. Although prominent static and transmit field variations occur at ultra-high fields, the obtained T_2 maps showed no B_0- or B_1-related degradations.

In conclusion, due to the observed robustness, TESS-T_2 may emerge as a valuable measure for early diagnosis and progression monitoring of brain diseases in high-resolution 2D acquisitions at high to ultra-high fields. In this work, 2D TESS relaxometry was restricted to single-slice acquisitions.

6.2 Future work

An overview will be given about the future work required to establish and further improve or extend the SSFP-based T_1 and T_2 quantification techniques presented in this thesis.

Clinical environment

- The presented relaxometry methods were carefully evaluated in the human brain (3D VFA T_1, single-slice 2D TESS T_2) and in the musculoskeletal system (3D DESS T_2, 3D TESS T_1 and T_2) of healthy volunteers. In future studies, their utility for clinical applications has to be examined. Conventional VFA T_1 mapping and DESS T_2 estimation are established techniques in clinical and research contexts for human brain tissue characterization and cartilage disease assessment, respectively. The proposed new postprocessing techniques are ready to be applied to clinical and basic research studies comprising VFA T_1 or DESS T_2 quantification.

- TESS-based combined T_1 and T_2 quantification has yet to be established. First results of a study assessing the clinical relevance of T_2 relaxation times measured

by 3D TESS in knee articular cartilage in comparison to conventional multi-echo SE T_2 quantification are presented in Ref. [1]. It is found that 3D TESS T_2 mapping provides similar quantitative results than multi-echo SE T_2 measurements with respect to precision and to the distribution of the T_2 values in cartilage but within substantially shorter scan times as well as pronounced B_0 and B_1 insensitivity. In particular, 3D TESS T_2 relaxometry was able to distinguish healthy cartilage tissue from lesions.

- 2D TESS relaxometry was investigated within the scope of this thesis for rapid single-slice T_2 mapping of human brain tissues. Generally, volumetric coverage is desired in order to make this method valuable for clinical applications. Therefore, further work is invested in order to extend single-slice 2D TESS imaging to multi-slice acquisitions (see below).

Motion sensitivity

- Only recently, single-slice 2D TESS imaging was modified for the use of Hadamard encoding in order to excite multiple slices simultaneously [2]. A four-slice Hadamard-encoded excitation scheme [3] was investigated for TESS T_2 mapping in the human brain and the increase in the signal-to-noise ratio compared to single-slice acquisitions was invested into a reduction of the overall scan time per slice. The derived setup resulted in snapshot-like T_2 mapping with an acquisition time of only 10 s for one slice and an in plane-resolution of 1.1×1.1 mm^2. Further work is needed to adapt the four-slice Hadamard scheme to whole-brain coverage by either exciting more slices simultaneously or interleaving consecutive four-slice acquisitions.

- An alternative strategy to tackle the motion sensitivity of 3D TESS is suggested in Ref. [4]. It makes use of a series of N phase-cycled 3D balanced SSFP acquisitions with different equidistant RF phase shift increments. The acquired N data sets can be manipulated to isolate the lowest-order SSFP configurations as acquired with TESS (F_{-1}, F_0, and F_1) by using an N-point discrete Fourier transform algorithm [5]. After calculation of the desired SSFP modes (F_{-1}, F_0, and F_1), T_1 and T_2 can be derived analogously to TESS relaxometry. This method offers fast 3D motion-insensitive combined T_1 and T_2 estimation. While the obtained quantitative T_2 results were robust and B_1-insensitive similar to TESS, T_1 appeared to be systematically underestimated [4]. Further research is needed to fully understand the mechanism leading to the observed T_1 underestimation.

Residual T_2 and diffusion sensitivity

- In this thesis, the accuracy of VFA T_1 mapping in the human brain could substantially be improved by using a global T_2 estimate and an analytical solution for the RF spoiled steady-state signal. The method proved to be robust and reproducible, however, a residual T_2 bias has to be considered, in particular for targets with higher T_2 variations than in the brain. This T_2 sensitivity can be eliminated by combining VFA T_1 estimation with an independent accurate determination of T_2, e.g. from the acquisition of two balanced SSFP scans with

varying flip angles and incorporated finite RF pulse correction [6], and then calculating T_1 and T_2 in an iterative approach similar to TESS relaxometry.

- The proposed VFA T_1 mapping technique shows some residual sensitivity to the choice of the RF phase difference increment due to the effect of diffusion. Future work may thus focus on deriving a method of optimal accuracy and more universal nature. For T_1 mapping based on SPGR acquisitions, optimal results require complete elimination of all transverse coherences prior to each RF pulse. The most effective way of achieving ideal spoiling is the use of a very long TR. It may thus be worth to review the potential of 2D interleaved multi-slice acquisition strategies with long repetition times for accurate T_1 quantification.

- The sensitivity of DESS and TESS relaxometry to diffusion was observed to be generally negligible for tissues. However, diffusion effects may considerably modulate the SSFP signals from fluids (e.g. CSF (cerebrospinal fluids) in the brain), in particular at low flip angles and in high-resolution scans. A possible option to yield improved quantitative results for fluids is the adaptation of the used SSFP signal model in order to include the effect of diffusion, e.g. by making use of the model developed by Freed et al. [7].

Ultra-high field applications

- Rapid TESS-based B_1-insensitive T_2 relaxometry has the potential to be of special advantage for ultra-high field applications. The accuracy of conventional SE-based T_2 measurement methods is substantially reduced at ultra-high field strenghts due to B_1 sensitivity, and the acquisition speed of these techniques is penalized because of specific absorption rate issues. Further work is needed to incorporate TESS into quantitative MR studies at ultra-high field strength, e.g. in the context of 3D visualization of cartilage. Recently, 3D TESS T_2 quantification was evaluated at 7 Tesla for the assessment of the median nerve in healthy volunteers and patients with carpal tunnel syndrome, and has shown ability to discriminate between healthy and damaged nerve structures [8].

Multiparametric mapping

- In this thesis, a rapid TESS acquisition scheme has been suggested to simultaneously derive the T_1 and T_2 relaxation times. As the accurate mapping of a single tissue parameter generally requires a priori knowledge about other material-specific or MR-related parameters, it is beneficial to develop acquisition techniques which are sensitive to numerous tissue properties and to calculate these parameters in a combined iterative approach without interacting bias. In this regard, future work may be invested into investigating whether the proposed single-component relaxometry methods can be extended to extract more information about the biochemical composition of the tissues (e.g. in the context of multi-compartment relaxation).

B_1 insensitivity of TESS-T_2

- The observed intriguing B_1 insensitivity of TESS T_2 relaxometry was manifest from numerical simulations, in vitro, and in vivo studies, however, it was not

theoretically proven. A theoretical consideration of this empirical result may help to better understand the underlying mechanisms leading to the complete B_1 insensitivity of TESS-T_2.

References

[1] V. Juras, K. Bohndorf, R. Heule, C. Kronnerwetter, P. Szomolanyi, B. Hager, O. Bieri, and S. Trattnig. Assessment of the clinical relevance of triple-echo steady-state T2 mapping in articular cartilage. In *Proc Intl Soc Mag Reson Med*, 2015.

[2] O. Pusterla, F. Santini, R. Heule, and O. Bieri. T2-snapshots imaging with simultaneous multislice TESS acquisition. In *Proc Intl Soc Mag Reson Med*, 2015.

[3] S. Müller. Multifrequency selective RF pulses for multislice MR imaging. *Magn Reson Med*, 6(3):364–71, 1988.

[4] D. Nguyen and O. Bieri. MIRACLE: Motion-Insensitive RApid Configuration reLaxomEtry. In *Proc Intl Soc Mag Reson Med*, 2015.

[5] Y. Zur, M. L. Wood, and L. J. Neuringer. Motion-insensitive, steady-state free precession imaging. *Magn Reson Med*, 16(3):444–59, 1990.

[6] H. J. A. Crooijmans, K. Scheffler, and O. Bieri. Finite RF pulse correction on DESPOT2. *Magn Reson Med*, 65(3):858–62, 2011.

[7] D. E. Freed, U. M. Scheven, L. J. Zielinski, P. N. Sen, and M. D. Hürlimann. Steady-state free precession experiments and exact treatment of diffusion in a uniform gradient. *J Chem Phys*, 119(9):4249–58, 2001.

[8] G. Riegler, G. Drlicek, C. Kronnerwetter, R. Heule, O. Bieri, B. Hager, P. Bär, and S. Trattnig. Triple-echo steady state T2 mapping and high resolution axonal bundle assessment of the median nerve in healthy volunteers and patients with carpal tunnel syndrome at 7 Tesla. In *Proc Intl Soc Mag Reson Med*, 2015.

Acknowledgment

I wish to thank

... Oliver Bieri who offered me the unique opportunity to work in his group on an interesting subject in an exciting growing research field. He had always time to discuss my work, provided me with many ideas, and guided me through these three and a half years with endless patience, enthusiasm, and confidence.

... Thomas Vetter for being willing to be my faculty representative and enabling me to do my thesis at the Faculty of Science, University of Basel.

... Stefan Ropele for evaluating my thesis as my co-examiner.

Many thanks to my colleagues and friends from the Radiological Physics group and the Neuroradiology group (including former members): Michael Amann, Grzegorz Bauman, Zarko Celicanin, Henk-Joost Crooijmans, Xeni Deligianni, Monika Gloor, Tanja Haas, Nicolin Hainc, Markus Klarhöfer, Philipp Madörin, Damien Nguyen, Orso Pusterla, Julia Reinhardt, Francesco Santini, Bram Stieltjes, Matthias Weigel, and Jinxia Zhu. In particular to

... Julia who became a dear friend.

... Orso and Damien for having agreed to be measured many times.

... Matthias for lively discussions about phase graphs.

... Xeni, Monika, and Francesco for their support at any time I needed help.

... Henk for encouraging me during the initial period of my PhD studies.

... Michael who was always checking my well-being whenever he saw me.

Many thanks also to

... my collaborators from the MR Centre of Excellence, Vienna and from the Max Planck Institute for Biological Cybernetics, Tübingen for applying the new TESS relaxometry technique at ultra-high field strength.

... Carl Ganter, Technical University of Munich, for contributing his broad MR expertise.

... the Swiss National Science Foundation (SNF) for the financial support.

My parents (Christine and Manfred), my twin sister (Noemi), my little (younger) sister (Sünja), and my friends were always there for me. Thank you!

Rahel Heule

Curriculum vitae

Personal data

Name:	Rahel Maria Heule
Date of birth:	April 24, 1985
Place of birth:	Brugg AG
Place of citizenship:	Widnau SG

Education

Jan. 2012 - June 2015:	PhD in Biophysics, University of Basel. Supervisors: Prof. Dr. Oliver Bieri and Prof. Dr. Thomas Vetter.
Sept. 2008 - May 2010:	Master of Science in Physics, University of Basel. Master's thesis in Theoretical Physics, supervisors: Dr. Vladimir M. Stojanović and Prof. Dr. Christoph Bruder, thesis title: *Operator control of a Heisenberg chain by locally acting on a single end qubit.*
Oct. 2005 - Sept. 2008:	Bachelor of Science in Physics, University of Basel.
Aug. 2001 - Dec. 2004:	Eidgenössische Matura, Gymnasium Muttenz BL (main subject: Latin), qualifying for university admittance.